DISSERTATION

INVESTIGATIONS OF LOW-TEMPERATURE REACTION PATHWAYS IN SOLID-STATE REACTIONS

Submitted by

Gia Thinh Tran

Department of Chemistry

In partial fulfillment of the requirements

For the Degree of Doctor of Philosophy

Colorado State University

Fort Collins, Colorado

Summer 2024

Doctoral Committee:

Advisor: James R. Neilson

Amy L. Prieto
Justin B. Sambur
Hua Chen

ABSTRACT

INVESTIGATIONS OF LOW-TEMPERATURE REACTION PATHWAYS IN SOLID-STATE REACTIONS

Advances in our technology are limited by our knowledge of functional materials and our synthesis methods. This dissertation discusses different synthesis methods for a variety of solid state materials. At the core of this thesis are metathesis reactions i.e., double displacement reactions. Metathesis reactions allow for control over product selectivity and reaction kinetics with choice of the spectating ions. We demonstrate these characteristics with different spectating ions in metathesis and cometathesis (e.g., combining two halides) reactions. $LaMnO_3$ was chosen to probe the product selectivity of anion cometathesis towards specific off-stoichiometries of $LaMnO_3$. The metathesis reaction for $BiFeO_3$ illustrates that predictions of thermodynamic selectivity is important, but reaction kinetics remain important as well. Kinetic studies of metathesis reactions that form $YMnO_3$ demonstrate the importance of crystalline intermediates to modulate the reaction rates.The complexity of solid-state kinetics their kinetic regimes within a reaction can be identified through synchrotron X-ray diffraction. We attempted to synthesize $LiMoO_2$ as precursors for the proposed phase $LaMoO_3$. We demonstrate our considerations on the synthesis challenges and offer insights into alternative Mo-based systems (nitrides). Aside from metathesis reactions, we employ learned concepts to flux reactions to influence the chemical potential of N_2. Synthesis of Li-Fe-O-N and Li-Mn-O-N phases was attempted under the hypothesis that alkali halide salt mixtures solubilize nitrogen and pin nitrogen's chemical potential to prevent N_2 formation. Cs_2SbCl_6 was chosen as a single crystal target to gain clearer insights into the electronic structure. Single crystals were synthesized via

hydrothermal synthesis, but preliminary conductivity measurements suggest that Cs_2SbCl_6 has impractical photoconductance.

ACKNOWLEDGEMENTS

My work was primarily supported as part of GENESIS: A Next Generation Synthesis Center, an Energy Frontier Research Center funded by the U.S. Department of Energy, Office of Science, Basic Energy Sciences under Award Number DE-SC0019212. My research used resources at beamline 28-ID-2 of the National Synchrotron Light Source II, a U.S. Department of Energy (DOE) Office of Science User Facility operated for the DOE Office of Science by Brookhaven National Laboratory under Contract No. DE-SC0012704. I appreciate assistance from staff scientist Wenqian Xu at Argonne National Lab 11-ID-B.

Chapter 6 on the synthesis of oxynitrides was supported by the US National Science Foundation, Award Number DMR-2210780.

I would also like to acknowledge the Analytical Resources Core at Colorado State University for their provision of PXRD instrumentation (Research Resource ID, RRID: SCR_021758). I appreciate the assistance from staff scientist Sanjit Ghose at NSLS-II.

In high school, I read *Into the Wild* by Jon Krakauer: A story on a young man who came to the conclusion that life has most meaning when it is shared with others. Let's ignore the rest of the circumstances described in the book about the physical state of the protagonist for now. With that sentimentality, I would like to dedicate this dissertation to the many people throughout my life up to this point. I appreciate every single encounter in my life. By no means can this document include all names, but I would like to highlight those who are most impactful to me. First, I would like to thank my advisor Dr. Jamie R. Neilson as a mentor and teacher. You enabled growth through compassion, a lot of patience, encouragements and reminders that the science that all your students are doing is interesting and valuable. Next, I would like to thank my undergraduate advisor Dr. Shahab Derakhshan at California State University Long Beach for his guidance. Your mentorship and support inspired me to pursue a Ph.D in chemistry. In extension to that, thank you Stephanie Araiza. You have been my first mentor who taught me all essential

basic techniques that every solid-state chemist needs. To my lab mates, thank you very much for your support and help throughout this journey. Dr. Paul K. Todd and Dr. Allison E. Wustrow pushed me to critically evaluate and re-evaluate my science to bring out the best form of it. It is unquestionable to say that my science is strongly influenced by yours. Of course I would like to thank all other “Neilsonite” that spent time with me together as you have built a strong support network for me. Thank you to Dr. Iain Oswald, who was the spark to my passion for volleyball which served as an effective outlet. Thank you to Dr. Eve Mozur, Dr. Jewels Fallon, Dr. Christopher Rom, Brennan McBride, and Dominic Asabiah. I would like to give thanks to an honorary Neilsonite Dr. Matt McDermott as he is an exceptional scientist and a good friend who worked with me in the ‘trenches to publish many of our works. I am also looking forward to the growth and accomplishments of future Neilsonites. My friends have been supportive throughout my journey. Khoi, Chhay, Malin, and Carolyn, we have been good friends for over 10 years. Life in the States would have been much grimmer if it wasn’t for you all. Thank you Mario for being a good friend and roommate. Thank you to Mario again, Sarah, Sammi, Zack, Tekoa, and Seth for introducing me to Dungeons and Dragons and playing a multi-year long campaign together. To my girlfriend Becky, thank you for your love and support. I am blessed to meet a loving and caring person such as yourself. I am happy to close this chapter of my life and begin a new one with you. Finally, I could never have accomplished anything without my family. You fed, cleaned, and nurtured me to who I am today. At the end of day, this Ph.D is really dedicated to you three. Mama und Papa, vielen Dank für alles was ihr beide für mich und Anh Khuong getan habt. Von euch habe ich gelernt nicht mit zu vielen Bedenken meine Ziele anzugehen. Anh Khuong, Danke dass du der beste grosse Bruder zu mir bist. Ich kann mir nicht vorstellen ein Leben ohne dich zu führen.

DEDICATION

I would like to dedicate this dissertation to my family: My brother Quoc An Tran, my father Tho Hoa Tran, and my mother Thi Ngoc Hoa Tran.

TABLE OF CONTENTS

LIST OF TABLES

LIST OF FIGURES

Chapter 1

Introduction

1.1 Significance and Challenges of Solid-State Synthesis

Materials define the limits and capabilities of our technologies, but limitations in our materials synthesis hinder progress towards more effective innovations. solid-state syntheses have produced history defining functional materials such that they revolutionize the status quo of our technology. Theoretical structure predictions in the solid-state community outpace the experimental synthesis and characterization of novel materials, experimentalists require new synthetic tools to test hypothesized phases. Furthermore, solid-state chemistry does not possess convenient separation techniques and has not yet established discrete reaction steps or mechanisms like molecular chemistry. To synthesize specific structures, experimentalists require control over synthesis pathways with those constraints. Traditionally, solid-state reactions, also called "ceramic methods" or "shake-and-bake", use high reaction temperatures to overcome the high diffusion barrier of solids (Figure 1.1 (a)). Consequently, the reaction usually favors the formation of thermodynamically stable phases with little to no control over the reaction mechanism. Many predicted phases are unstable at elevated temperatures, thus called metastable, but they could be accessible at milder reaction temperatures. Therefore, it is important to fully understand synthesis approaches to gain more control over product selectivity in reactions. By studying the reaction pathway of solid-state systems, computational models and materials synthesis approaches can be improved.

While there are ways to access these metastable phases, there is no general guiding principle to predict or rationalize the reaction pathway.[4–6] To circumvent the selectivity problem, the solid-state community resorted to extrinsic factors like high pressure and precursor morphology to alter the relative free energy of the reaction.[7,8] Quenching from

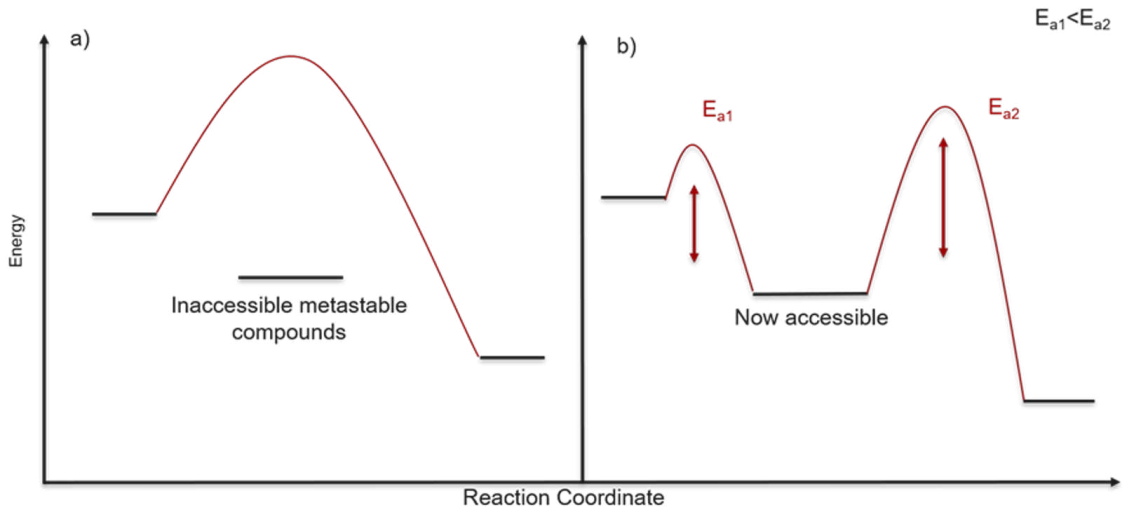

Figure 1.1: Schematic reaction coordinate diagrams illustrating (a) typical synthesis of thermodynamically most stable phases and (b) selective synthesis towards kinetically stabilized metastable phase.

high pressure and temperature can kinetically trap metastable phases, which become stable under these conditions.

Another approach is to control the activation barrier of the reaction. (Figure 1.1(b)).[9] Flux-assisted and solvothermal reactions promote higher diffusion of ions while maintaining a low temperature profile. Solvothermal reactions heat a reaction within a solvent above the melting point of the solvent. The reactants do not need to melt but instead dissolve more readily inside the solvent, enabling higher diffusion.[10]

Fluxes (often common salts like LiCl and KCl) are solid at ambient temperature, but are molten at the reaction temperature. Their purpose is akin to solvents in solvothermal reactions, they promote diffusion of atoms and ions through a liquid medium. Owing to eutectic points of two different salt mixtures, a reaction can operate at lower temperatures with a salt flux as opposed to without (Figure 1.2).[1,11]

Metathesis reactions can also lower the kinetic barrier. Metathesis reactions use the formation of a highly stable salt side-product to drive the reaction to completion.[12] In this dissertation, the main focus will be on select metathesis reactions and their modifications

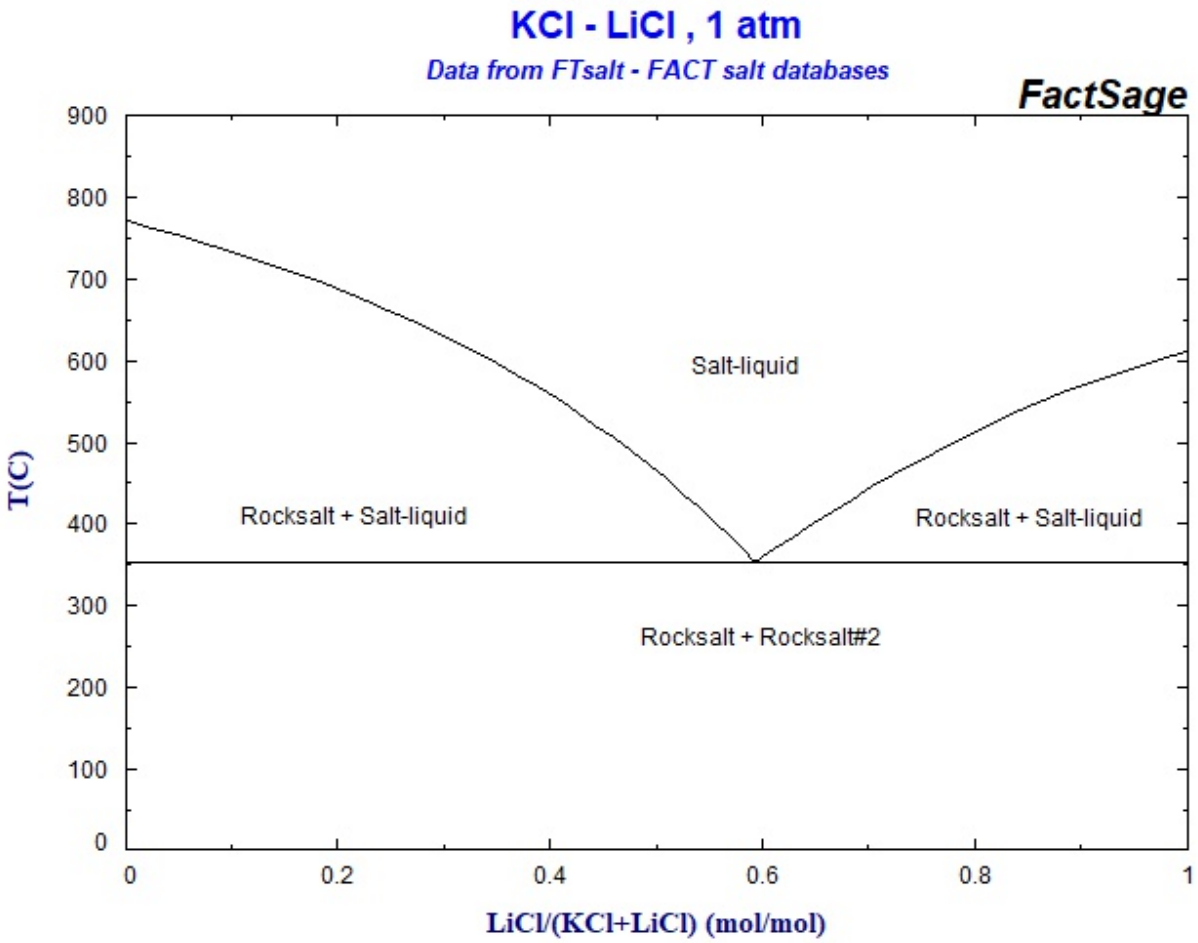

Figure 1.2: Equilibrium phase diagram of LiCl–KCl system. The eutectic point of the salt flux is lower than the melting temperature of each salt individually. Figure reproduced from Bale et al.[1]

in an effort to control the energetic landscape of reactions, access metastable polymorphs, selectively synthesis target structures.

1.2 The Ceramic Method vs. Metathesis Reaction

solid-state metathesis reactions were originally explored for their self-heating and extremely exothermic nature to synthesize materials.[13] Recent investigations demonstrated that metathesis reactions can decrease the reaction temperature required for solid-state syntheses, especially in comparison to ceramic methods: For example, the synthesis of metastable chalcogenides ($T_{\text{rxn}} < 150$ °C)[14] or the alkali-dependent synthesis of different

yttrium manganese oxides ($500 < T_{rxn} < 800$ °C).[15,16] Modifications to metathesis reactions offer control over the reaction pathway and thus the reaction outcome. The "spectator" cation choice and the polymorph of the precursors in metathesis reactions towards $YMnO_3$ determined the reaction intermediates and the product phase.[15,17] Furthermore, the mixing of multiple "spectating" ions display improved reactivity as the observed reaction temperature decreased and also demonstrated product selectivity.[11,18]

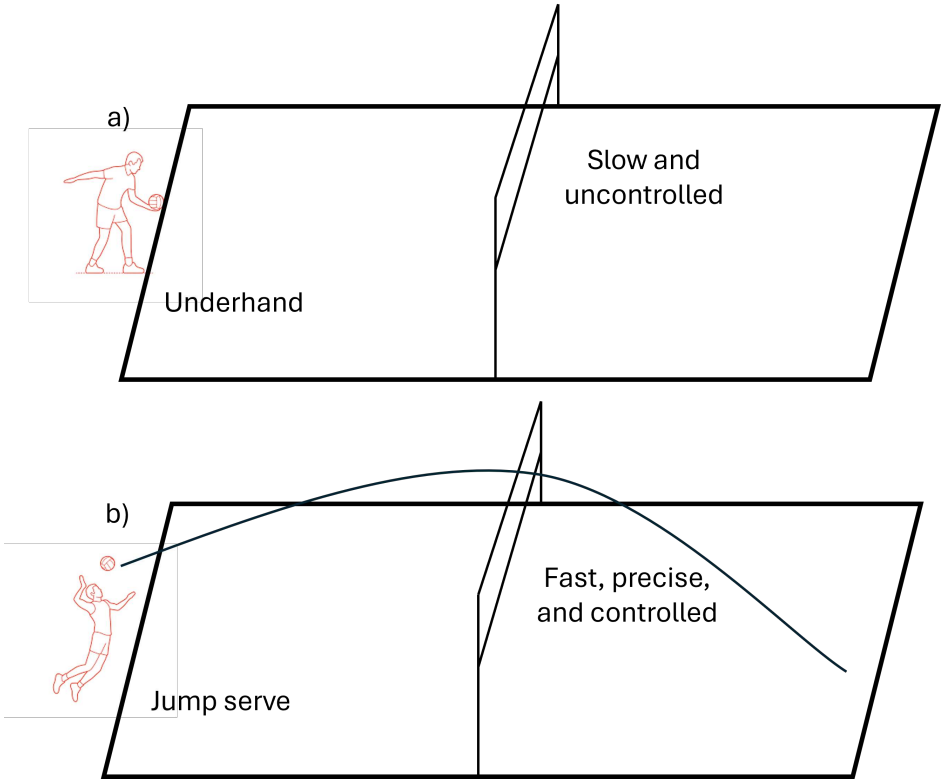

Figure 1.3: Schematic representation of (a) an underhand serve and (b) an overhand serve in volleyball.

A direct comparison between the original shake-and-bake method and modified metathesis method in regard to temperature conditions, kinetics, and phase selectivity points out that metathesis reactions offer advantages across all three aspects. We can draw an analogy between the reaction methods and two different types of serves in volleyball to illustrate this concept (Figure 1.3(b)). The classic underhand serve launches the ball over the net

to the other side by hitting the ball from underneath which often results in an arch-like trajectory that reaches high altitudes but sacrifices speed and accuracy. Akin to the traditional ceramic method, this serve ensures that it overcomes a high barrier, but lacks in speed and control over the placement on the other side of the volleyball court. On the other hand, the metathesis is comparable to an overhand serve. The ball is held or tossed at an angle approximately 45° above the head before it is hit to launch it across the net. The ball launches faster than the underhand serve but reaches sufficient altitudes to fly over the net. Like the metathesis reaction, there are many modifications to the overhand serve that can alter the trajectory path as well as the motion of the ball (rotation) as it travels over the net.

1.3 The Gradient Furnace

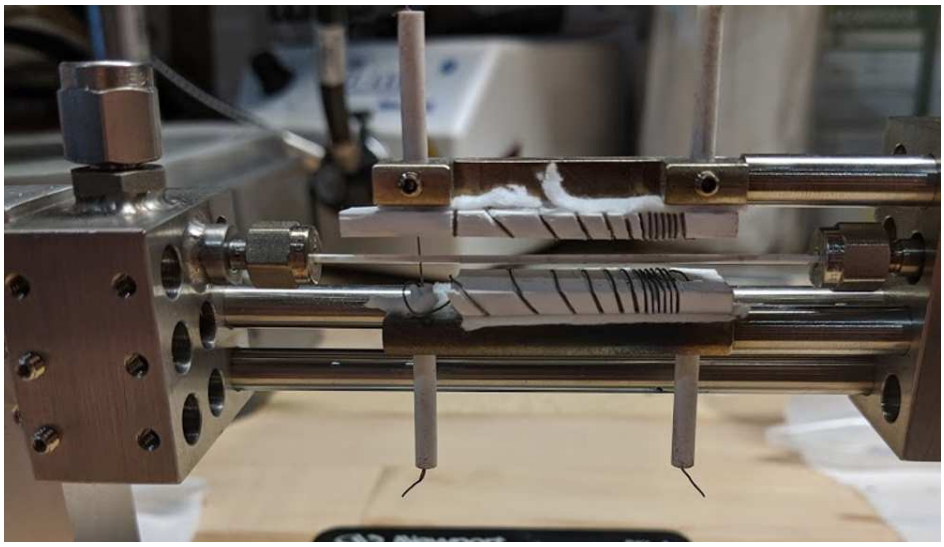

Figure 1.4: Picture of the gradient furnace.

A major portion of data in this thesis were collected at the National Synchrotron Light Source II at Brookhaven National Laboratory. The pivotal instrument of these experiments is a custom-made gradient furnace shown in Figure 1.4. The furnace was designed and pro-

vided by O'Nolan, et al.[19] The gradient furnace ensures its temperature gradient through scaling densities of heating elements along a quartz capillary (Friedrich & Dimmock). The furnace features custom 3D-printed ceramic bars with resistively heated Kanthal (FeCrAl alloy) wire that fit in grooves within the bars. The non-uniform heating is generated by the non-equal distances of the coiled wire. A small hole in the upper mount allows for a K-type thermocouple to measure the local temperature. The gradient range was determined by measuring temperature-dependent lattice parameters determined from X-ray diffraction data collected for solids with known coefficients of thermal expansion. In most cases NaCl was used.[20] More details are outlined in the respective methods sections. Each horizontal position is calibrated and defined to a temperature.[19] One can conduct the same reaction under different reaction temperature at the same time. The design of the furnace is most valuable at synchrotron beamline facilities where the allotted time is limited. Most importantly, the gradient furnace allows for kinetic studies of solid-state reactions. As the reaction progresses, multiple time points can be taken.

1.4 Thesis Overview

This dissertation addresses reaction pathways of multiple solid-state methods as well as a hydrothermal synthesis towards Cs_2SbCl_6 single crystals. However, the bulk of this dissertation investigates reaction pathways in solid-state metathesis reactions towards products with the ABX_3 stoichiometry. Chapter 2 details product selectivity of non-stoichiometric $LaMnO_3$ through anion cometathesis. Chapter 3 revolves around the metathesis towards $BiFeO_3$ and the effect of different spectator cations on the reaction kinetics. Chapter 4 describes the kinetic studies from *in situ* synchrotron X-ray diffraction (SXRD) of several metathesis reactions towards the formation of $YMnO_3$. Chapter 5 describes the synthesis attempts towards $LiMoO_2$ and elaborates on difficulties in synthesizing Mo-based oxides. The chapter concludes with remarks about promising Mo-based nitrides as nitrogen has intrinisc properties that facilitate molybdenum valences between +3 and +5. Chapter 6

describes synthesis attempts of novel oxynitrides using an eutectic salt flux of LiCl and KCl to pin the chemical potential of nitrogen gas. Chapter 7 reports the hydrothermal synthesis towards Cs_2SbCl_6 single crystals and preliminary conductivity measurements. The last chapter includes concluding remarks about the work discussed in the aforementioned chapters and proposes ideas on possible future directions of the studies.

Chapter 2

Selective Synthesis of Defect-Rich $LaMnO_3$ by Low-Temperature Anion Cometathesis*

Overview

The synthesis of complex oxides at low temperatures brings forward aspects of chemistry typically ignored. This study focuses on perovskite $LaMnO_3$, which is of interest for its correlated electronic behavior tied to the oxidation state and thus spin configuration of manganese. Traditional equilibrium synthesis of these materials typically requires synthesis reaction temperatures in excess of 1000 °C, followed by subsequent annealing steps at lower temperatures and different $p(O_2)$ conditions to manipulate the oxygen content post-synthesis (e.g., $LaMnO_{3+x}$). Recent use of double-ion exchange (metathesis) reactions have been shown to react at much lower temperatures (500-800 °C), highlighting a fundamental knowledge gap for how solids react at lower temperatures. Here, we revisit the metathesis reaction, $LiMnO_2 + LaOX$, where X is a halide or mixture of halides, with *in situ* synchrotron X-ray diffraction. These experiments reveal low reaction onset temperatures (ca. 450-480 °C), with the lowest reaction temperature provided by a mixture of related precursors in "cometathesis" reaction with two halogen-containing precursors, $2\ LiMnO_2 + LaOCl + LaOBr$. In all cases, the resulting products are the expected alkali halide salt and a defective $LaMnO_{3+x}$, consistent with a rapid local equilibration of the precursors with crystalline intermediates and the expected global thermodynamic equilib-

* Reprinted with permission from G.T. Tran, A. Wustrow, D. O'Nolan, S. Tao, C.J. Bartel, T. He, M.J. McDermott, B.C. McBride, K.W. Chapman, S.J. L. Billinge, K. A. Persson, G. Ceder, and J.R. Neilson, Selective Synthesis of Defect-Rich $LaMnO_3$ by Low-Temperature Anion Cometathesis, *Inorg. Chem*. 2024, 63, 7, 3250–3257. Copyright 2024, American Chemical Society. G.T.T and J.R.N. conceptualized the project. A.W., B.C.M., and S.T assisted with *in situ* X-ray diffraction experiments and analysis. D. O'N. provided essential equipment, C.J.B. and M.J.McD. provided calculations. T. He provided data mining. G.T.T. performed the experiments and wrote the manuscript with guidance of J.R.N.

rium with O_2(g) as revealed by computational thermodynamics. Together, these results reveal how the inclusion of additional elements (e.g., Li and a halide) impart a direct, single-step route to the equilibrium conditions at reaction temperatures normally inaccessible to solid-state chemistry.

2.1 Introduction

Our understanding of how solid-forming reactions proceed and are controlled tends to be limited at intermediate temperatures. For reactions below ca. 300 °C, we know that some ions of low charge and/or size can selectively diffuse,[21] thus enabling the synthesis of highly out-of-equilibrium phases such as $LaNiO_2$[22] and $SrFeO_2$[23] with square planar transition metal coordination geometries or unusual oxidation states.[24] This contrasts the apparent non-selective diffusion down concentration gradients that occurs at elevated temperatures ($T > 800$ °C).[25] solid-state metathesis reactions, while originally explored for their highly exothermic nature to synthesize refractory materials, can be used to synthesize materials requiring far milder conditions,[26] such as in the synthesis of metastable chalcogenides ($T_{rxn} < 150$ °C)[14] or the alkali-dependent synthesis of different yttrium manganese oxides ($500 < T_{rxn} < 800$ °C).[15,16] In these oxide-forming reactions, it has been shown that the precursor polymorph influences how the reaction proceeds.[17] Furthermore, *cometathesis* reactions with mixtures of "spectating" ions (e.g., the alkali or alkaline earth elements) exhibit cooperative reactivity highlighted by a reduced reaction temperature (e.g., $MgMn_2O_4 + CaMn_2O_4 + 4$ YOCl),[11] and even polymorph selectivity.[18] However, many simple questions remain concerning the general applicability and understanding of the progression toward equilibrium of these reactions.

As a focus of this study, $LaMnO_3$ has been studied for its ability to accommodate a range of defect concentrations and the resulting physical properties in the nonstoichiometric phases. The phase is often mixed valence, and control over the valence gives rise to the highly non-linear "colossal magnetoresistance" effect.[27] While the Mn valance can

be modified via aliovalent substitution (e.g., Sr^{2+} for La^{3+}), the reaction temperature and exposure to different oxygen partial pressures give rise to significant cation vacancies and nonstoichiometry that can also produce mixed valence Mn.[2,28,29] For highly oxidized compounds, the prototypical $Pnma$ tilted perovskite structure undergoes a phase transition to the $R\bar{3}c$ perovskite crystal structure for $x \geq 0.09$.[28] While this manuscript will refer to the non-stoichiometric composition as $LaMnO_{3+x}$, it is important to articulate that the excess oxygen is accommodated via cation vacancies and not oxygen interstitials: $La_{1-\epsilon}Mn_{1-\epsilon}O_3$, where $\epsilon = x/(3+x)$.[28] However, the concentration of La and Mn vacancies need not be equivalent. In general, we will refer to this phase and the non-stoichiometric variants as $LaMnO_3$; we only refer to the stoichiometric compound where specifically noted.

The oxygen content in$LaMnO_3$ is reliant on the chemical potential of oxygen which is temperature dependent. As a survey of the synthesis conditions of $LaMnO_3$, high temperatures are employed, which limits the highest chemical potential of oxygen accessible under ambient pressure. According to 76 $LaMnO_3$ synthesis procedures extracted from the experimental literature (see Appendix A A.1), citekononova2019text the reaction temperatures range from ca. 500 °C to ca. 1500 °C, with most reactions taking place between 1000-1300 °C (Figure 2.1). Typical precursors include manganese oxides and La_2O_3. However, initial metathesis[30] and "assisted" metathesis[31] reactions employing $LiMnO_2$ as a precursor reported lower reaction temperatures (ca. 800-850 °C). Most synthetic conditions require an initial high-temperature reaction followed by annealing at lower temperatures under varied atmospheres to adjust the stoichiometry.

Here, we specifically study and discuss the ternary metathesis reactions,

$$\mathrm{LiMnO_2} + \mathrm{LaO}X \longrightarrow \mathrm{Li}X + \mathrm{LaMnO_3}, \tag{2.1}$$

where X=Cl,Br. The primary questions addressed are: (1) how does the reaction temperature relate to the byproduct salt phase diagram and its solidus; and, (2) how do the local chemical potentials of the reactants and subsequent intermediates impart selectiv-

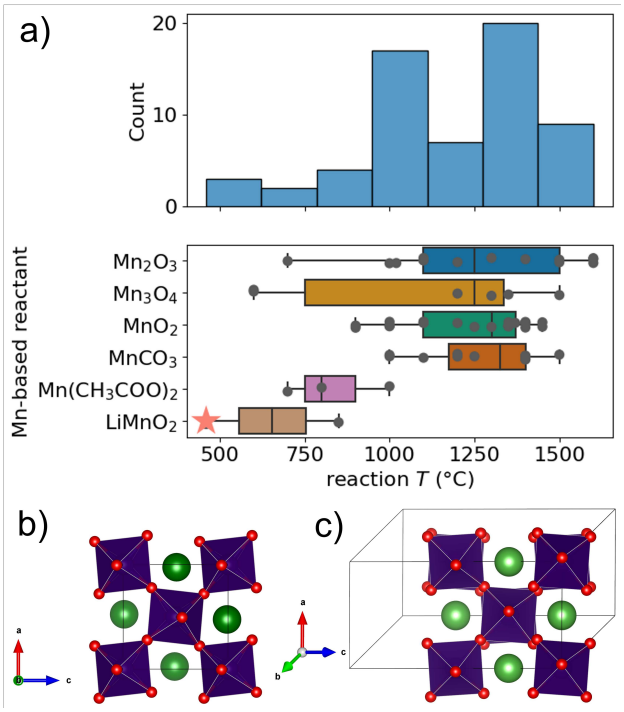

Figure 2.1: (a) Top: Histogram of reported $LaMnO_3$ syntheses at across a range of reaction temperatures. Most report a temperature of at least 800 °C or above. The star marks the reaction temperature that is reported herein. Bottom: Distribution of reaction temperatures as sorted by different Mn-containing precursors used to synthesize $LaMnO_3$ at given temperatures. Mn_3O_4 and $Mn(CH_3COO)_2$ precursors require oxidation and appear with lower reaction temperatures. (Crystal structure representations of (b) $R\bar{3}c$ and (c) $Pnma$ $LaMnO_3$.

ity over the final reaction products. Focusing on reactions to produce $LaMnO_3$, by design of reaction stoichiometry, $LiMnO_2$ is combined with stoichiometric equivalents of LaOCl, LaOBr, or the mixture of 0.5 LaOCl + 0.5 LaOBr. Using synchrotron X-ray diffraction with a modified capillary furnace, a series of *in situ* and post-heated isothermal X-ray diffraction patterns show the influence on the defect-mediated reaction pathway and that combination of byproduct anions lowers reaction temperatures. From a detailed crystallographic analysis, the crystalline intermediate phases suggest that the reaction proceeds by propagating point defects in the different reactive phases. Combined with an analysis of the overall thermodynamic landscape, it appears that the local chemical potentials of the relevant intermediates establish a reaction that produces an oxidized "$LaMnO_{3+x}$" product,

consistent with experiments performed at high temperatures and high equilibrium oxygen partial pressures.

2.2 Experimental Methods

2.2.1 Precursor Synthesis

0.3g of lanthanum oxyhalides were synthesized via solid-state synthesis. Lanthanum oxide was mixed with stoichiometric amounts plus 10 mol% excess of the respective ammonium halide salt (Acros Organics 99.9%) with a mortar and pestle. The mixture was then placed in an alumina crucible to heat in air at 600 °C for 3 h with heating and cooling rates of 10 °C/min. 5g of $LiMn_2O_4$ was synthesized by reacting stoichiometric amounts of Li_2CO_3 (Baker, 99.3%) and Mn_2O_3. Mn_2O_3 was synthesized by heating $MnCO_3$ (Sigma-Aldrich, 99.9%) in an alumina crucible in air at 850 °C for 12 h with heating and cooling rates of 10 °C/min. The Li_2CO_3 and Mn_2O_3 powders were mixed using a mortar and pestle, pelleted, and heated in an alumina crucible at 800 °C for 24 h with heating and cooling rates of 10 °C/min.[32] To prepare tetragonal $LiMnO_2$, $LiMn_2O_4$ powder was refluxed under nitrogen in a 4 M LiI solution in acetonitrile (Alfa Aesar, 99.9 %) where the overall Li:Mn ratio was 6:1. The reflux was performed using an oil bath. After reflux, the powder was filtered and washed with acetonitrile to remove residual LiI and I_2 before it was dried under vacuum at 80 °C.[33]

2.2.2 Bulk Reactions

Bulk reactions were prepared by mixing stoichiometric amounts of $LiMnO_2$ and lanthanum oxyhalides in a mortar and pestle for 15 min in an argon glovebox with $\leq$ 1 ppm O_2 and $\leq$ 1 ppm H_2O. The homogenized mixture was then pelleted, placed in a cylindrical alumina crucible, and sealed in an evacuated quartz ampule ($\leq$20 mTorr). Reactions were heated at 10 °C/min to the dwell temperature (600 °C) to ensure product formation within four hours. Sample product identification was verified with laboratory powder X-

ray diffraction (PXRD) data collected on a Bruker D8 Discover diffractometer using Cu Kα radiation and a Lynxeye XE-T position sensitive detector (Fig. A.1).

2.2.3 *In Situ* and *Ex Post Facto* SXRD Reactions

Synchrotron X-ray diffraction (SXRD) data were collected at beamline 28-ID-2 at the National Synchrotron Light Source II at Brookhaven National Laboratory. Data for the reactions were obtained with a gradient furnace, where each horizontal position is calibrated and defined to a temperature.[19] The gradient furnace ensures its temperature gradient through scaling densities of heating elements along a quartz capillary (Friedrich & Dimmock). Samples were packed into 1.1 mm outer diameter, 0.9 mm inner diameter quartz capillaries in an argon-filled glovebox, and carefully flame-sealed under vacuum. This ampule was then brought out of the glovebox and quickly sealed under vacuum ($\leq$20 mTorr). Calibration of detector curvature was performed using CeO_2 at all points along the gradient furnace using pyFAI.[34] SXRD data were collected on a PerkinElmer plate detector at 1400 mm distance and 1480 mm at two different visits to the light source. Using a PID-controlled power source, a horizontal temperature range of 300-800 °C along the capillary was created. The temperature at a given position was calibrated with NaCl and its thermal expansion.[20] Samples were held at temperatures for 40 min twice for two separate time points. Samples were then cooled at an approximately 5 °C/min rate. *Ex post facto* diffraction data were collected with a wavelength of 0.1949 Å at ambient temperatures.

2.2.4 Quantitative Analysis of Diffractive Data

Quantitative phase analysis of X-ray diffraction data was performed using the Rietveld method with TOPAS v6 software package. The following assumptions were made for consistent analysis: Atomic displacement parameters were fixed to a value of $B = 1$ Å^2, and peak broadening is primarily modeled via crystal size broadening using a refined Lorentzian function. Data from *ex post facto* SXRD runs are plotted as weight fractions.

2.2.5 Computational Methods

Formation enthalpies (at 0 K) were obtained with density functional theory (DFT) using the r2SCAN meta-GGA density functional.[35,36] Starting structures were obtained either from the Materials Project database[37] or from the XRD-refined structures synthesized in the present work. All structures were optimized using the Vienna Ab initio Simulation Package (VASP) and the projector augmented wave (PAW) method.[38] A plane wave energy cutoff of 520 eV and 1000 k-points per reciprocal atom were used for all calculations. Gibbs free energies of formation, $\Delta G_f(T)$, were obtained for each solid compound by combining the DFT-calculated formation enthalpies with vibrational and configurational contributions to the entropy. The vibrational entropy contribution was determined using the machine-learned descriptor introduced by Bartel et al.[39] Configurational entropy was estimated by considering the entropy of mixing for an ideal solid solution for any site having partial occupancies. Gibbs formation energies, including DFT-computed ambient temperature formation enthalpies, model-predicted vibrational entropies, and ideal mixing configurational entropies, were then used to compute all Gibbs reaction energies presented in this work. Reaction energies were normalized to yield one mole of $LaMnO_3$.

Predominance diagrams were constructed using the chemical potential diagram approach described by Yokokawa[40] and implemented in previous work.[16] Thermodynamic data for the predominance diagrams were acquired from the Materials Project (MP), version 2022.10.28. Gibbs free energies of formation for temperatures $T > 0$ K were approximated from MP data using the aforementioned machine-learned descriptor developed by Bartel et al.[39] According to our computed data, $LaMnO_3$ is not predicted to be stable at any temperature. Thus, $LaMnO_3$ was manually stabilized (energy lowered until brought onto the hull) to illustrate its approximate position on the predominance diagram. The predominance diagrams were constructed as two-dimensional projections in μ_{La}-μ_{O} space from the full five-dimensional (La-Mn-O-Li-X) chemical potential diagram for the system. Boundaries from the higher-dimensional space (e.g., $LiMnO_2$ in the La-O

predominance diagram) are plotted as slices as previously described.[16] Oxygen chemical potentials marked on the predominance diagram were estimated for different pressures as $\mu_O = 0.5 k_b T \log P_{O_2}$, where P_{O_2} is the partial pressure of O_2 gas in units of atmospheres. These oxygen chemical potentials represent differences from the standard state chemical potential of oxygen, μ_O^0, which is taken to be 0 eV at $P_{O_2} = 1$ atm. An atmospheric oxygen partial pressure of 0.1731 atm was assumed for the air in Fort Collins, CO ($\approx$ 5000 ft).

2.3 Results and Discussion

Ex situ synchrotron powder X-ray diffraction indicates that the temperature at which defect-rich $LaMnO_3$ forms falls below the solidus of the LiCl-LiBr phase diagram, with the lowest temperature reaction being that containing mixed halogen precursors: $LiMnO_2$ + 0.5LaOCl + 0.5LaOBr. Using the gradient furnace (see Methods), the product distributions of the quenched reactions were determined using the Rietveld method and plotted in Figure 2.2. Qualitatively, the phase distributions are illustrated by their identity as precursors, intermediates, and products. The intermediate phases observed include orthorhombic $LiMnO_2$ and a phase consistent with Mn_3O_4. For the cometathesis reaction, solid-solution $LaOCl_{0.5}Br_{0.5}$ is formed. In all three reactions studied, the alkali halide salt forms at the same nominal reaction temperature (e.g., capillary position) as $LaMnO_3$; the temperature for this reaction onset is approximately 50 °C below the melting point for the LiCl-LiBr solidus (Figure 2.3). The lowest $LaMnO_3$ formation temperature is observed for the anion cometathesis reaction (LaOCl onsets at ca. 490 °C; LaOBr onsets at ca. 470 °C; and the LaOCl/LaOBr mixture onsets at ca. 450 °C). Product formation at onset temperature below the nascent salt solidus has been previously observed in alkali and alkaline earth cometathesis reactions (e.g., $MgMn_2O_4$ + $CaMn_2O_4$ + 4 YOCl),[11,18] and we proposed that the abrupt onset is consistent with the surface melting of the nascent salt. A nascent salt is distinct from the formation of a bulk molten alkali halide, as the crystalline salt is observed by *in situ* diffraction at the onset temperature, and adiabatic self-heating

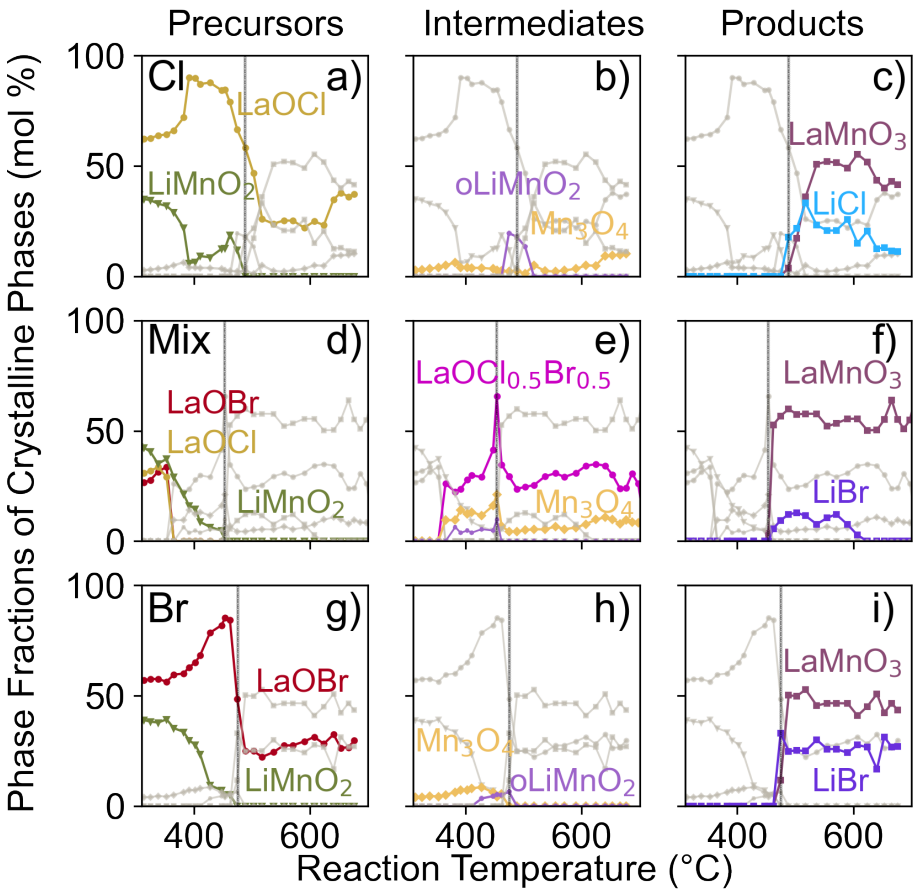

Figure 2.2: Phase fractions of crystalline phases from isothermal reactions performed at different temperatures in a gradient furnace from powder synchrotron X-ray diffraction data for the reaction of (a-c) $LaOCl + LiMnO_2$ (g-i) $LaOBr + LiMnO_2$, and (d-f) $0.5\ LaOCl + 0.5\ LaOBr + LiMnO_2$. Formation temperatures are marked as vertical solid gray lines. The lowest reaction temperature (450 °C) for the formation of $LaMnO_3$ occurs with $0.5\ LaOCl + 0.5\ LaOBr + LiMnO_2$, while all observed $LaMnO_3$ formation temperatures are around 50 °C colder than the melting point temperature of the salt.

does not appear to be sufficient to cause melting at the interface.[11] Here, it is clear that the mixing of anions produces a similar effect consistent with surface melting of the nascent alkali halide salt at the interface, akin to cation cometathesis, acting to facilitate $LaMnO_3$ formation.

Ex situ synchrotron powder X-ray diffraction shows that the metathesis reactions produce $LaMnO_3$ with a reduced unit cell volume upon cooling down relative to the stoichiometric unit cell, most consistent with cation vacancies (e.g., $La_{1-\epsilon}Mn_{1-\epsilon}O_3$). The

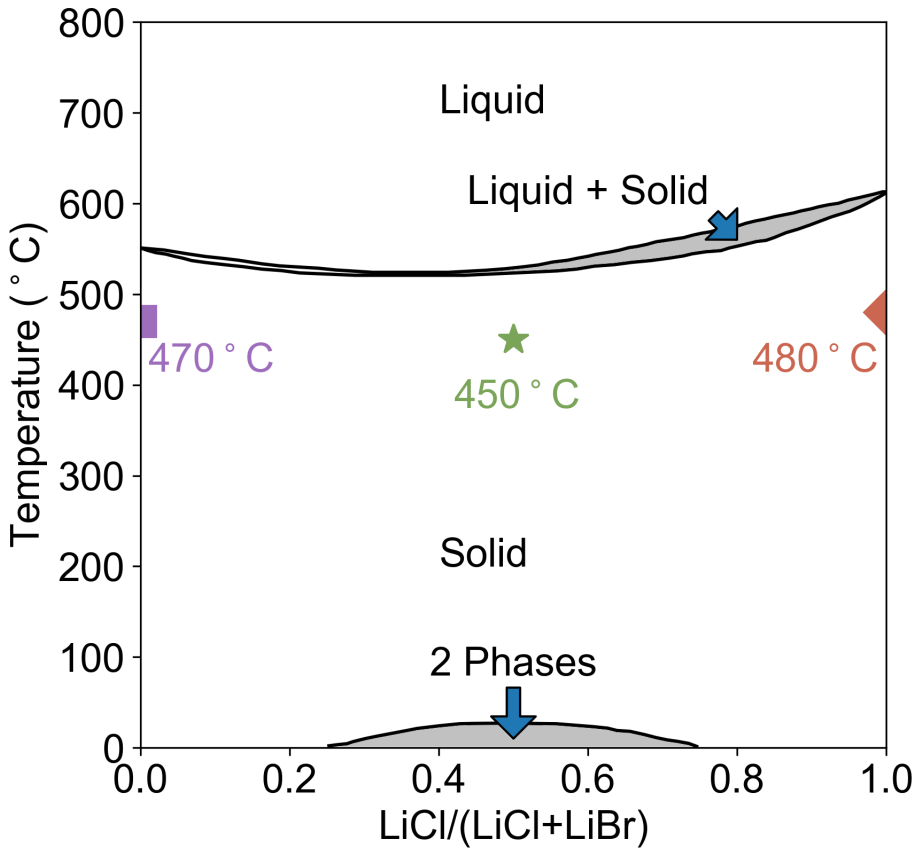

Figure 2.3: Equilibrium phase diagram of LiCl–LiBr system. $LaMnO_3$ onset formation temperatures of each metathesis reaction are marked (Cl as red diamond, Br as purple square, cometathesis as green star).[1] The onset temperature in the cometathesis reaction is approximately 100 °C below the solidus line.

unit cell volume of $LaMnO_3$ was calculated from Rietveld refinements and plotted as a function of reaction temperature in Fig. 2.4. In all cases, the structure described by the $Pnma$ space group provides the best fit to the data. The rhombohedral $R\bar{3}c$ structure often found with highly oxidized $LaMnO_{3+x}$[28] or Li-substituted $LaMn^{3+}_{1-3x}Mn^{4+}_{2x}Li_xO_3$ did not provide a better fit to the data (see Figure A.5 and the discussion therein).[41] The unit cell of $LaMnO_3$ produced at higher reactions temperatures is smaller relative to lower reaction temperatures. Comparison of the observed unit cell volumes with previous studies[28,42] reveals that the product from the LaOCl/LaOBr cometathesis reaction is nearly stoichiometric upon at the lowest reaction temperatures formation (compared to 61.05 $Å^3$/fu[28]

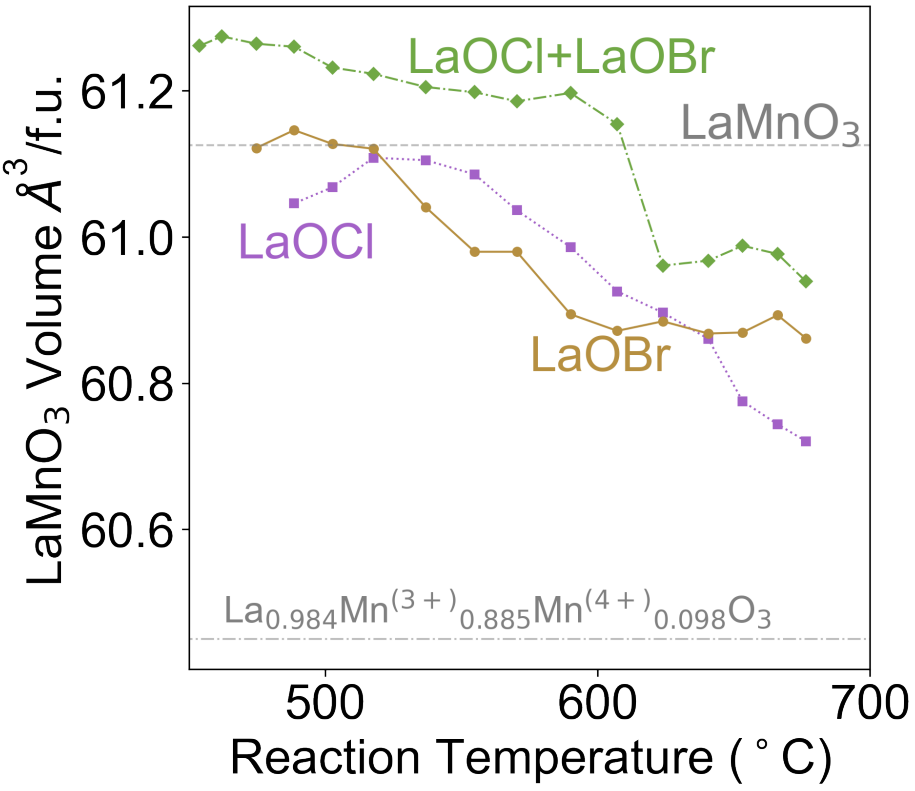

Figure 2.4: Unit cell volume of $LaMnO_3$ as a function of temperature determined by Rietveld refinements. Single anion 0.5 LaOCl/Br + $LiMnO_2$and 0.5 LaOCl + 0.5 LaOBr + $LiMnO_2$ reactions yield a higher unit cell volume than the phase formed by solid solution metathesis. Topfer reports stoichiometric $LaMnO_3$ with a volume of 61.05 Å^3 (gray dashed line) and $La_{0.984}Mn^{3+}{}_{0.885}Mn^{4+}{}_{0.098}O_3$ with 60.40 Å^3 (gray dashdotted line).[2]

to 61.2 Å^3/fu[42]). Yet, at higher reaction temperatures, the unit cell volume is smaller as previously attributed to the presence of a smaller Mn^{4+} cation and cation vacancies.[28] One would typically expect that reactions at higher temperatures to be less oxidizing, due to the reduced chemical potential of O_2(g) at elevated temperatures. The observations here are counter to this expectation.

A closer examination of *In situ* PXRD collected at different time points during the reaction as it happens reveals a time-dependent variation of the unit cell volume of $LaMnO_3$. The gradient furnace used in these experiment permit practical analysis of the time-dependent change in the lattice parameters at constant temperature, as summarized in Table 2.1. Upon its initial formation at the lowest temperature (e.g., at onset), the

unit cell volume of $LaMnO_3$ is close to the volume of a stoichiometric phase. Over time at constant temperature, the unit cell volume increases: at 488 °C the volume increases from 61.662(1) Å^3/fu to 63.095(1) Å^3/fu. From the benefit of the gradient furnace, the isothermal nature of this time-dependent change rules out thermal expansion of $LaMnO_3$. To further rule out thermal expansion, Miyoshi, et al., calculated a linear thermal expansion coefficient of $(1.06(1)) \times 10^{-5}$;[43] the expected volume from thermal expansion of stoichiometric $LaMnO_3$ is only 61.999(1) Å^3/fu at 488 °C. The same trend in increasing unit cell volume with prolonged time is also observed at 570 °C. The unit cell after cooling is smaller than what is predicted from thermal contraction of the 40-minute time point measured at elevated temperature: at 488 °C one would expect 63.095 Å^3 to contract to 62.179(1) Å^3; at 570 °C one would expect 63.118 Å^3 to contract to 62.043(1) Å^3 instead of the observed volumes (Table 2.1). Therefore, we turn to computationally-derived phase diagrams to address the equilibration of the precursors with the evolving atmosphere at these low temperatures.

To explain the trends in $LaMnO_3$ unit cell volumes as a function of reaction temperature and time, we analyze what would one might expect from a computationally-derived chemical equilibrium at reaction interfaces and of the overall reaction environment. To understand the equilibrium of a reaction interface, it is useful to employ a predominance diagram viewed along the axes of the elemental chemical potentials that define the system. Since the local interface has a nearly infinite reservoir of each elemental component, the intensive variable of chemical potential is more reliable than the extensive variable of the average concentration.[40] The predominance diagram shown in Figure 2.5 illustrates the La-Mn-O chemical potential space viewed in the μ_{La}-μ_O axes, along with the intersection of $LiMnO_2$ and LaOCl from the high-dimensional La-Mn-O-Li-Cl chemical potential space, as previously described.[16,44] This phase diagram is derived from computationally-tractable analogs to the real non-stoichiometric phases that exist in experiments that are readily accessible from the Materials Project database.[37] For example, the ordered, cation-deficient

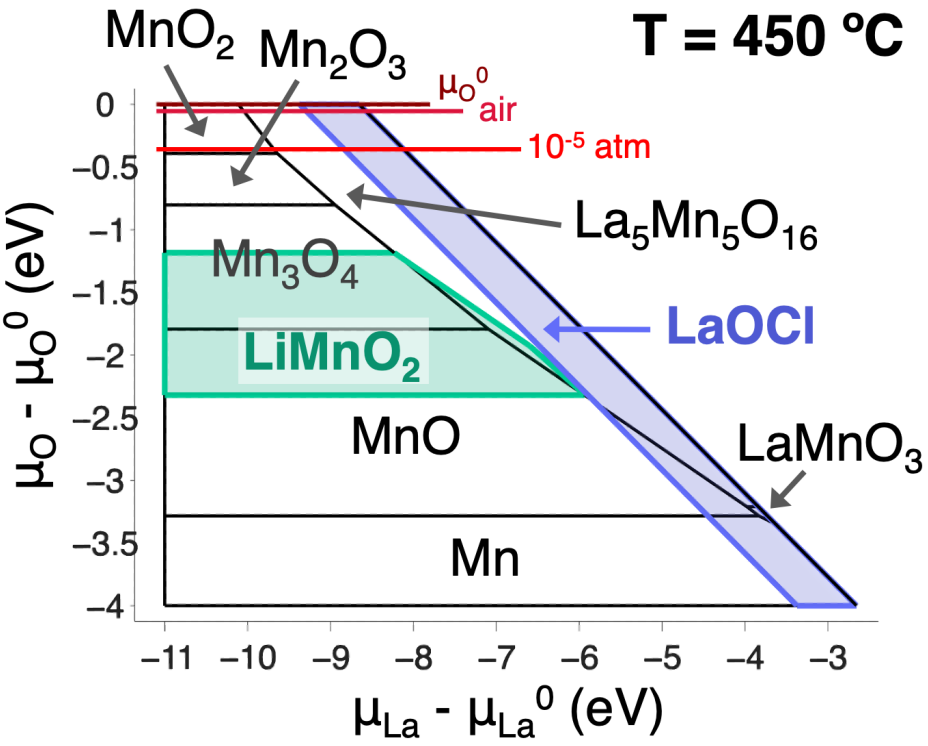

Figure 2.5: DFT-derived Predominance diagram of lanthanum and oxygen chemical potential shown at 450 °C referenced to their standard elemental state. For the La-Li-Mn-O-Cl system, a description of the reaction energetics is provided in the Supporting Information, with specific elaboration of the relative contribution of the entropy attributed to solid solution formation. Pressures of oxygen gas (red lines) highlight the chemical potential that is expected at 1 atm, partial oxygen pressure in air, and partial pressure that is expected in an argon atmosphere (10 ppm). $LiMnO_2$ (green), LaOCl (blue), were plotted as a plane across the chemical potential space. The metathesis byproduct LiX has been omitted for visual clarity as it is always stable. All projected phases overlap with the over-oxidized phase $La_5Mn_5O_{16}$ and share a stable interface with the oxidized phase. Only LaOCl overlaps with $LaMnO_3$. $La_5Mn_5O_{16}$ should be treated as a summary of all stable oxidized $LaMnO_3$ rather than a stoichiometrically specific compound.

phase, $La_5Mn_5O_{16}$, summarizes the overlapping ranges of stability for the near continuum of cation-deficient $LaMnO_3$ phases. The large stability field of $La_5Mn_5O_{16}$ reflects that significant propensity for oxidation via cation deficiency of stoichiometric $LaMnO_3$ visible at low oxygen chemical potentials.

We previously illustrated that reactant-product adjacency on chemical potential diagrams can rationalize selective phase formation based on the local equilibration of chemical potentials across the reactant/product interfaces.[16] In the phase equilibria illustrated

in Figure 2.5, LaOCl and $LiMnO_2$ both share a stable boundary with $La_5Mn_5O_{16}$, suggesting that nucleation of $La_5Mn_5O_{16}$ at the LaOCl/$LiMnO_2$ will lead to local thermodynamic equilibrium and may pin the local oxygen chemical potential to a rather low value. If one draws the shortest distance in chemical potential space between LaOCl and $LiMnO_2$, this is near an oxygen chemical potential of ca. $\mu_O - \mu_O^0 = -2$ eV. If we assume that "$La_5Mn_5O_{16}$" represents a continuum of non-stoichiometric $LaMnO_3$ phases, then we would expect this phase to have the largest unit cell volume at the lowest oxygen chemical potentials, consistent with the observed *in situ* unit cell volumes (Table 2.1).

However, the oxygen chemical potential of the reaction environment is significantly higher and promotes the formation of a more oxidized $LaMnO_3$ with a smaller unit cell volume. In these reactions performed in evacuated capillaries and ampules, the $p(O_2)$ $\approx 10^{-5}$ atm, for which $\mu_O - \mu_O^0 = 0.5 k_b T \ln(p/p^0) = -0.458$ eV at 650 °C. If we assume that the presence of $LiMnO_2$ pins the local chemical potentia between the values of $\mu_O - \mu_O^0$ = -1.2 eV and -2.25 eV (e.g., its stability window along the $\mu_O - \mu_O^0$ axis), then after $LiMnO_2$ is sufficiently consumed, the oxygen chemical potential is no longer pinned to those values. As such, the system can equilibrate that of the surrounding atmosphere which starts at a much higher value (-0.458 eV). This analysis of the local thermodynamics at the reaction interfaces explains the time and temperature dependent shift in the unit cell volumes of $LaMnO_3$. At the higher temperatures studied here, this equilibration with the atmosphere becomes noticeable due to the enhanced solid-state oxygen diffusion, which is severely hampered at the lower temperatures. Islam, et al., reported higher oxygen diffusion of Sr doped $LaMnO_3$ at elevated temperatures in agreement with our hypothesis on the significance of the chemical potential.[45] Together, we propose that the chemical potential of the precursors define the local equilibrium of the reaction by way of their respective stability windows with respect to the elemental chemical potentials.

Going further, crystallographic examination of the evolution of other phases in the reaction mixture provides corroborating evidence of the progression from a local to bulk

Table 2.1: Volumes of $LaMnO_3$ per formula unit from *in situ* and *ex situ* LaOBr + ceLiMnO2 metathesis reaction in relation to temperature and time. $LaMnO_3$'s unit cell volume increases above the onset temperature as well as over time. The unit cell shrinks upon cooling.

Temperature (°C)	Time (min)	Volume (Å^3/f.u.)
488 °C	20 mins	61.662(1)
488 °C	40 mins	63.095(1)
Ex post facto 25 °C	post ex facto	61.145(1)
570 °C	20 mins	62.965(1)
570 °C	40 mins	63.118(1)
Ex post facto 25 °C	post ex facto	62.552(1)

equilibrium at higher reaction temperatures. The quenched reaction products identified from isothermal reactions reveal that tetragonal $LiMnO_2$ undergoes a phase transformation into the more thermodynamically stable orthorhombic $LiMnO_2$ polymorph $Pmnm$, as well as the formation of a phase that is best indexed as tetragonal spinel consistent with Mn_3O_4 ($I4_1/amd$). The observation of a stoichiometric Mn_3O_4 would suggest that there is a net reduction of Mn during the reaction, or it may serve as a source of excess oxygen during the formation of $LaMnO_{3+x}$. From the Rietveld analysis of the Mn_3O_4 phase, the peak intensities are inconsistent with a stoichiometric model. Upon refining the Mn site occupancy of Mn_3O_4, the octahedral site has a reduced occupancy ($g(Mn_{oct}) = 0.671(1)$), consistent with either vacancies or Li substitution, as illustrated in Figure 2.6 (Apendix A for calculations of valency). Yet, the tetrahedral site occupancy remains relatively unchanged. Assuming that a vacancy replaces the Mn, the average valence of the $Mn_{3-x}O_4$ phase works out to 3.3(1); if one assumes Li_{Mn} substitution, the valence is 3.0794(1). Therefore, the change in the manganese valence averaged over all Mn compounds during the reaction is small. This observation is consistent with previous studies of the metathesis reactions $LiMnO_2$ + YOCl, during which $LiMnO_2$ reacted towards two lithium manganese oxide spinel intermediates.[17,46] There, the presence of both in the intermediates suggested a charge disproportionation of manganese ions, with the defected cubic spinel $LiMn_2O_4$ accumulating a $Mn^{3+\delta}$ valance and the tetragonal spinel accumulating a $Mn^{3-\delta}$ valance.[17,47]

However, this study on metathesis reactions found only a defect-rich tetragonal spinel and an over-oxidized $LaMnO_{3+x}$.

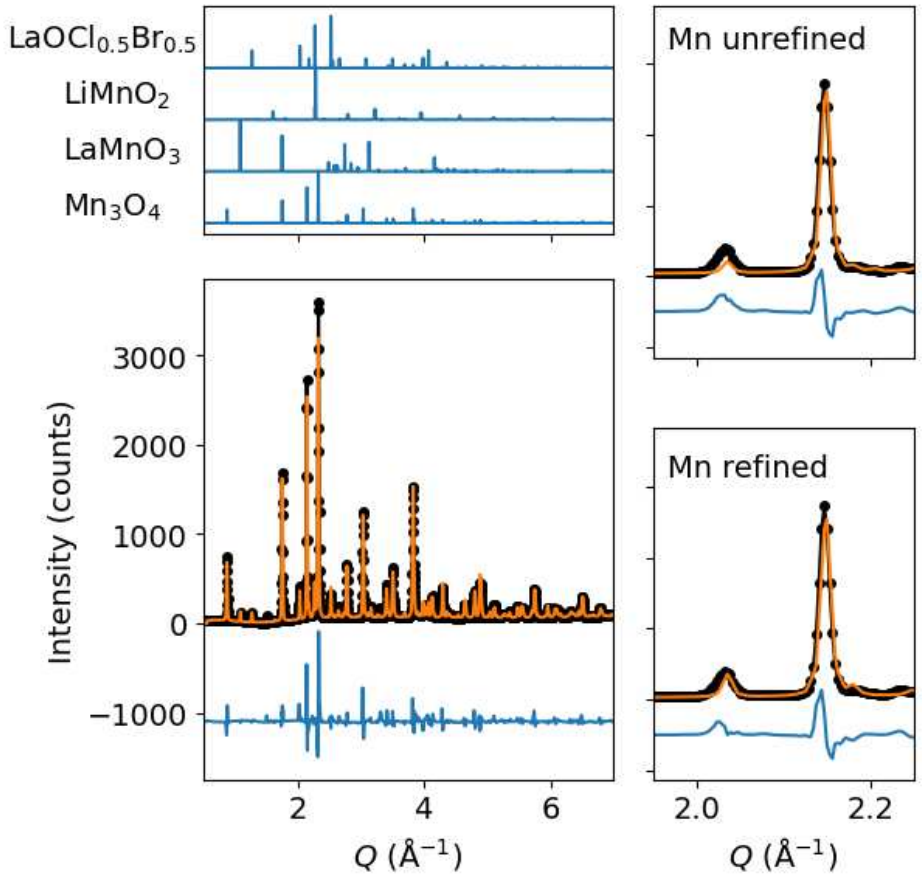

Figure 2.6: Rietveld refinements of anion cometathesis reaction LaOCl + LaOBr + 2 $LiMnO_2$. Refinements on the octahedral manganese sites improve the fit (orange line) to the data (black dots) better as Mn site occupancy was refined.

LaOX are known to accommodate non-stoichiometry through ordered and disordered defects. Crystallographic analysis of the LaOX phases during the reaction do not reveal gross defect nonstoichiometry but perhaps some subtle deviations that give insight to the reaction path. In the anion cometathesis reaction, LaOCl and LaOBr react to form solid solution $LaOCl_{0.5}Br_{0.5}$. As defects are known to influence the unit cell volume, the volumes of LaOX were extracted from the *ex post facto* diffraction data using the Rietveld method. In Figure 2.7(b), the LaOX average volume is computed by adding together the unit volumes

of the observed LaOX phases (e.g., LaOCl, LaOBr, Cl-rich solid solution, Br-rich solid solution; then $LaOCl_{0.5}Br_{0.5}$ above 370 °C) and dividing by the total number of phases present (four or five), thus assuming an equimolar mixture of phases. The unit cell volumes of LaOCl and LaOBr during single anion metathesis reactions stay relatively consistent at 116.95 $Å^3$ and 127.88 $Å^3$, respectively, as a function of temperature. Anion cometathesis reactions reveal a discontinuous jump in LaOX volume as solid solution $LaOCl_{0.5}Br_{0.5}$ forms. Once formed, the volume of $LaOCl_{0.5}Br_{0.5}$ decreases to 120.7 $Å^3$ as temperature increases. According to Vegard's law, the theoretical unit cell volume is predicted to be 121.9 $Å^3$.

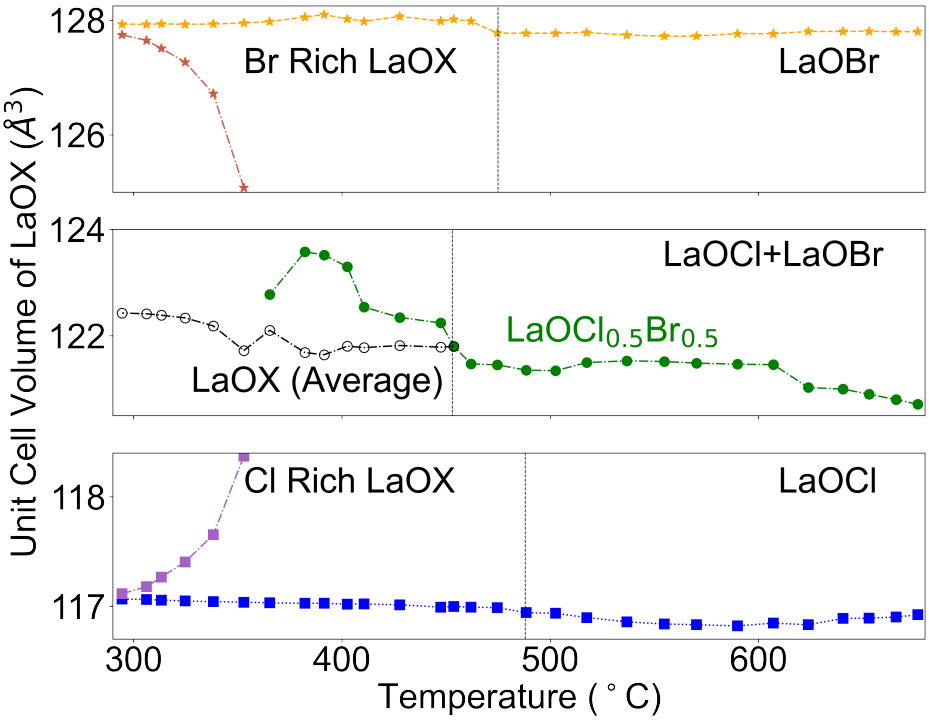

Figure 2.7: Unit cell volume of LaOX as a function of temperature determined by Rietveld refinements. The unit cell volume of each end member system are shown in comparison to the unit cell volume of each end member as it reacts to form solid solutions (purple and red). The unit cell volume of the $LaOCl_{0.5}Br_{0.5}$ is shown compared to the average of all LaOX species. The volumes of LaOX phases prior to the formation of $LaOCl_{0.5}Br_{0.5}$ have been averaged and are represented as one volume in b). The solid solution decrease over the course of the reaction after the product onset temperature (indicated with the gray vertical lines) well below the literature value while single halide phases experience less volume changes. Residual LaOX phases are detected above the reaction onset temperatures.

The continual decrease of the unit cell volume of solid-solution $LaOCl_{0.5}Br_{0.5}$ suggests that cometathesis propagates through different defect formation mechanisms than single anion methathesis reactions. We explore the following three hypotheses: 1) asymmetric anion reactivity with a greater loss of bromine than chlorine, 2) cation intercalation into the van der Waals gap during reaction with $LiMnO_2$, and 3) preferential deintercalation of halogen. The first hypothesis is inconsistent with the observed lattice parameter of the salt byproduct LiX that is 5.35(1) Å, which agrees with the expected value for $LiCl_{0.5}Br_{0.5}$ predicted with Vegard's law. However, we cannot entirely rule out a higher reactivity of Br if excess Br resides in phases (or interfaces) that are amorphous and not detectable with diffraction. For the second hypothesis, one would expect an increase of the c axis with the intercalation in metal oxychlorides, but the opposite is observed.[48,49] This leaves the third hypothesis, in which the halogen preferentially deintercalates. This is rationalized by two factors. In the solid-solution $LaOCl_{0.5}Br_{0.5}$, the local strain from having two different halide radii likely decreases the effective bond dissociation energy of the halogen relative to the oxygen. Secondly, as La^{3+} is removed from the crystal during reactivity, it can be equivalently charge compensated by the co-removal of an equal amount of oxygen and halogen, 3/2 an oxygen anion (e.g., three oxygen for two lanthanum) or three halogens. Therefore, one expects a higher rate of halogen removal based solely on the stoichiometric ratios. Both factors would lead to increased reactivity of the halogen that is consistent with the observations.

2.4 Conclusion

Metathesis reactions provide the ability to control the local equilibrium of reactions at their onset, which then reach a global equilibrium with reaction progression. Specific to this study, the role of anion cometathesis (i.e., a mixture of like precursors) is identical to that of cation cometathesis (e.g., mixing halogens is the same as mixing alkalis). In detail, the reaction of $LiMnO_2$ + LaOX, where X is Cl, Br, or an equimolar mixture, the

product $LaMnO_{3+x}$ forms with excess oxygen relative to the metal cations. By understanding the chemical potential landscape, we can enable more synthetic control in solid-state syntheses, as atomistic defect species in functional materials often control macroscopic properties. Further efforts to understand defect formation in low temperature synthesis will assist us in the pursuit of complete selective synthesis.

Chapter 3

Synthesis of $BiFeO_3$ Using Metathesis Reactions*

3.1 Overview

Many ceramic materials require very strict reaction condition to synthesize and are otherwise not attainable if their requirements are not met. $BiFeO_3$, toted for its multiferroic behavior, is challenging to synthesize: it appears to be stable only in a narrow temperature range (540 to 830 °C) and minor, adventitious incorporation of additional elements can lead to high fractions of secondary phases such as $Bi_2Fe_4O_9$ and $Bi_{25}FeO_{39}$. Here, we employ stoichiometric, double-ion exchange reactions (aka "metathesis") to synthesize $BiFeO_3$ powders. Using computationally-guided selection of precursors, we identify various salts with favorable thermodynamic selectivity toward $BiFeO_3$ and an alkali halide salt, such as $A\text{FeO}_2 + \text{BiOF}$, where A = Li, Na, and K. Curiously, only $KFeO_2$ (yielding KF) yields stoichiometric $BiFeO_3$ during synthesis. *In situ* synchrotron X-ray diffraction data collected from different reaction temperatures, as well as isothermal kinetic analysis, reveals that $BiFeO_3$ forms very rapidly and decomposes under the synthesis conditions with A = Na, while reactions with Li do not form $BiFeO_3$. Only with $KFeO_2$ can the target phase be isolated under practical conditions in the laboratory employing rapid heating followed by rapid quenching into iced brine. We demonstrate that $BiFeO_3$ can be synthesized phase pure via metathesis reaction.

---

* Substantial portions of this chapter have been reproduced with permission from G.T. Tran, B.C. McBride, M.J. McDermott, R. McAuliffe, Z. Thatcher, G. Kamm, G. Veith, S.J. L. Billinge, K. Chapman K. A. Persson, G. Ceder, and J.R. Neilson, Synthesis of $BiFeO_3$ using metathesis reactions, *Prepared Manuscript*. 2024. G.T.T, B.C.M and J.R.N. conceptualized the project. B.C.M., and Z.T assisted with *in situ* X-ray diffraction experiments and analysis. G.K. provided essential equipment, M.J.McD. provided calculations. R. McA. provided precursor. B.C.M performed the experiments and G.T.T wrote the manuscript with guidance of J.R.N.

3.2 Introduction

$BiFeO_3$ has been extensively studied for its multiferroic properties but its bulk synthesis faces phase purity challenges. Multiferroic materials exhibit more than one of the primary ferroic properties in the same phase. The most desired combination would be ferroelectricity and ferromagnetism with coupling between the two.[50] Below Néel temperature of 643 K, $BiFeO_3$ exhibits ferroelectricity, ferroelasticity, and antiferromagnetism. The Bi^{3+} ion provides $6s^2$ lone pair electrons that are polarizable by an external electric field and Fe^{3+} delivers 3*d* electrons that enable the phase to order antiferromagnetically in an magnetic field.

Past publications identified that the chemical phase space is easily skewed by temperature and impurity inclusions. solid-state reactions at lower temperatures (below 800 °C) synthesize $Bi_2Fe_4O_9$ and $Bi_{25}FeO_{39}$ over $BiFeO_3$.[51,52]At higher temperatures $BiFeO_3$ decomposes and Bi_2O_3 volatilizes which in turn shifts the phase space towards off stoichiometries.[53] Rapid thermal sintering showed success in mitigating the decomposition of $BiFeO_3$.[54] $BiFeO_3$ suffers from phase purity issues and easily coexists with other ternary oxides such as $Bi_2Fe_4O_9$ and $Bi_2Fe_4O_9$, or $BiFeO_3$ decomposes to the binary Bi_2O_3. In fact, some impurity elements such as Mn shift the equilibrium to produce substituted phases of $Bi_2Fe_4O_9$ or $Bi_{25}FeO_{39}$.[55]

Metathesis reactions demonstrate how the inclusion of "spectating ions" assist synthesis efforts. Metathesis reactions were originally deployed for their highly exothermic nature to synthesize refractory materials,[56] but we have shown that they synthesize materials at milder conditions,[11,57] or guide the reaction to different products, depending on the precursor choice.[15,16] Although, utilizing "spectating" ions proves as useful, it is difficult to choose the best performing reaction, even if we restrict ourselves to reactions of the form,

$$A\mathrm{FeO_2} + \mathrm{BiO}X, \tag{3.1}$$

due to the large number of possible combinations. Modern DFT calculations and compositional phase diagrams of multidimensional phase diagrams, enable prediction of the ideal reactants based on the reaction energetics.

We utilize a solid-state reaction selectivity metric designed by McDermott et al. to down-select the most promising metathesis reaction towards $BiFeO_3$.[58] A chemical reaction network scheme based off of all entries from the Materials Project Database in the A-X-Bi-Fe-O system, where A = Li, Na, K, Rb, Cs, Mg, Ca, Sr, Ba and X = F, Cl, Br, I, permits facile calculation of the reaction energies for reactions producing $BiFeO_3$ and the corresponding halide salt, as found in metathesis-style reactions.[37] The competition metric is based on the chemical potential distance,[16] and can be used to select precursors that reduces the number of intermediate species between precursor and product.

In this contribution, we demonstrate how DFT calculations and high-dimensional compositional phase diagrams identify the most selective reactions, $A\text{FeO}_2 + \text{BiOF}$, where A= Li, Na, K, from over 8500 possible reactions. Using synchrotron X-ray diffraction with a modified capillary furnace, a series of *in situ* isothermal X-ray diffraction reveal the influence on the synthesis of $BiFeO_3$. We show how the inclusion and identity of spectator ions affect the synthesis of $BiFeO_3$. Specifically, we show how the metathesis reaction with $KFeO_2$ guides the reaction towards $BiFeO_3$.

3.3 Experimental

3.3.1 Precursor Synthesis

$LiFeO_2$ was synthesized via solid-state synthesis (1g scale). Li_2CO_3 (Alfa Aesar 99%) in 5mol % excess was mixed with α-Fe_2O_3 (Fisher Scientific 98%) using a mortar and pestle in air. The mixture was then placed in an alumina crucible to heat under argon flow at 700 °C for 48 h with a heating rate of 6 h total. The sample was furnace-cooled by turning off the heating of the furnace with no specific cooling rate set. α-$NaFeO_2$ was prepared by McAuliffe et al. via ball-milling of Na_2O_2 and α-Fe_2O_3 in an argon glovebox. The resulting

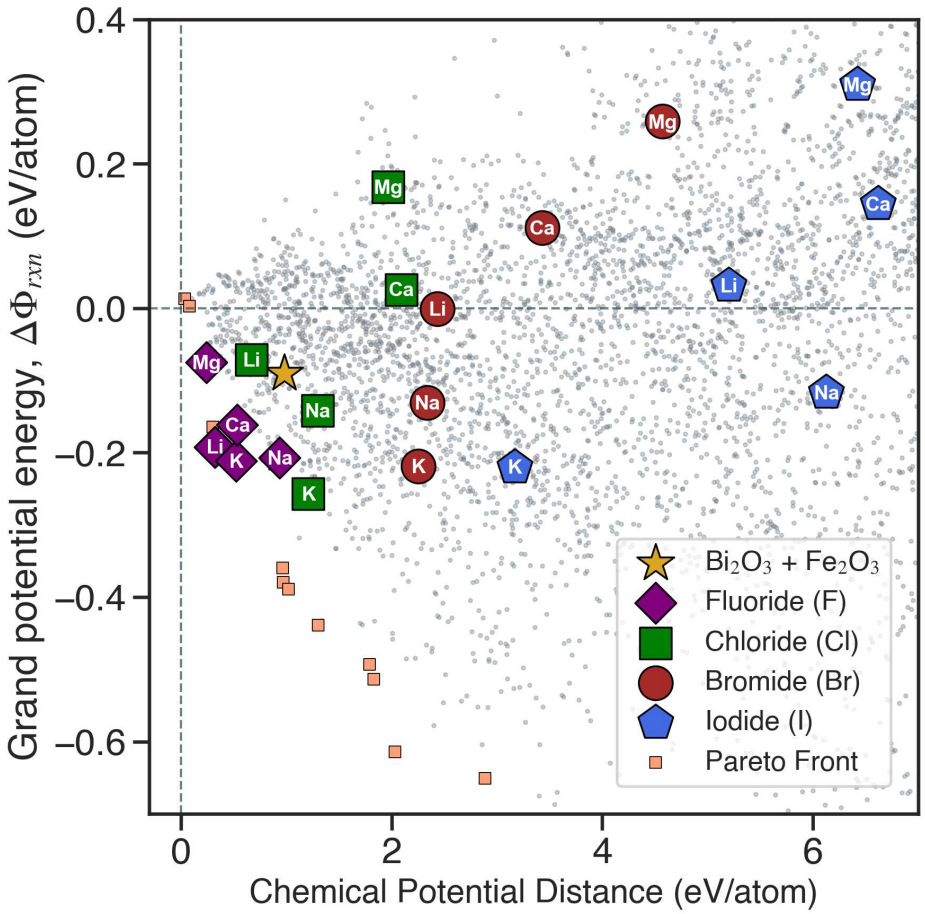

Figure 3.1: Synthesis map for $BiFeO_3$ reactions. Grand potential energies, $\Delta\Phi_{rxn}$, of reactions at $T = 800$ °C and $\mu_O = -0.110$ eV ($(pO_2) = 70$ Torr) and their selectivity (total chemical potential distances) for all 8,610 balanced reactions in the A-X-Bi-Fe-O system that yield $BiFeO_3$ (A = Li, Na, K, Mg, Ca; X = F, Cl, Br, I). The highlighted reactions correspond to those with the formula $A(FeO_2)_q + q\text{BiO}X \longrightarrow q\text{BiFeO}_3 + \text{AX}_q$, where q corresponds to the oxidation state of the cation species, A and $q \in \{1, 2\}$. Reactions incorporating fluorine (F) are the closest to the Pareto front and, thus, the most viable, i.e., they provide the maximal selectivity (lowest chemical potential distance) with the greatest driving force. Within the F-based reactions, Li and K are in the Pareto front, and K provides the maximal change in free energy.

powder was then heated in air to 700 °C for 12 h at a 10 °C/min heating rate. After heating for 12 h, the sample was furnace-cooled by turning off the heating of the furnace.[59] $KFeO_2$ was synthesized via solid-state synthesis (1g scale). K_2CO_3 (Alfa Aesar 99%)and α-Fe_2O_3 (Fisher Scientific 98%) were mixed with a mortar and pestle. The mixture was then placed in an alumina crucible to heat under argon flow at 900 °C for 12 h with a heating rate of 10 °C/min. The sample was furnace-cooled by turning off the heating of the

furnace. Phase pure BiOF was synthesized by sol-gel method. 1.619g of $Bi(NO_3)_3 \cdot 5\,H_2O$ (Sigma-Aldrich 98%) was mixed with 2-times molar excess NH_4F (Sigma-Aldrich 99%) and dissolved in ethylene glycol (Acros Organics technical grade). The mixture was stirred until everything was dissolved. There is potential of HF forming, therefore, we advise the use of HF-resistant PPE and appropriate methods to clean HF contaminated equipment. The resulting gel was dried at 80 °C and then heated at 350 °C overnight.

3.3.2 Ex situ Reactions

Stoichiometric amounts of AFeO$_2$ and BiOF were mixed in a mortar and pestle to synthesize 0.1g of $BiFeO_3$ in the reaction $A\text{FeO}_2 + \text{BiOF} \longrightarrow \text{BiFeO}_3 + A\text{F}$, where A is either Li, Na, or K. The mixture was pelletized and then placed in an alumina boat which in turn was placed in an open-ended mullite tube to heat under an O_2/Ar flow (pO_2 = 70 Torr) at 860 °C for 0-10 min (see Figure 3.3). After the chosen reaction time, the alumina boat was dropped into an iced-salt-water slurry to quench the reaction. For the synthesis of single-phase $BiFeO_3$, the pellet was quenched after 1 min and washed with 0.1 M HNO_3 solution (see Figure 3.3 (b)).

3.3.3 *In situ* SXRD Reactions

Synchrotron X-ray diffraction (SXRD) data were collected at beamline 11-1D-B at the Advanced Photon Source at Argonne National Laboratory. Data for the reactions were obtained with a gradient furnace, where each horizontal position is calibrated and defined to a temperature.[19] The gradient furnace ensures its temperature gradient through scaling densities of heating elements along a quartz capillary. Samples were packed into 1.1 mm outer diameter, 0.9 mm inner diameter quartz capillaries (Friedrich & Dimmock) in an argon-filled glovebox and carefully flame-sealed under vacuum. Calibration of detector curvature was performed using LaB_6 at all points along the gradient furnace using pyFAI.[34] SXRD data were collected on a PerkinElmer plate detector at 600 mm distance. Using a PID-controlled power source, a horizontal temperature range of 325-750 °C along

the capillary was created. The temperature at a given position (1 mm increments) was calibrated with NaCl and its thermal expansion.[20] Samples were held at temperatures for 40 min twice for 5-8 separate time points. Samples were then cooled at an approximately 5 °C/min rate. *Ex post facto* diffraction data were collected after the heating experiment with a wavelength of 0.2408 Å at ambient temperatures.

3.3.4 Quantitative Analysis of Diffractive Data

Quantitative phase analysis of X-ray diffraction data was performed using the Rietveld method with TOPAS v6 software package. The following assumptions were made for consistent analysis: Atomic displacement parameters were fixed to a value of $B = 1$ Å^2, and peak broadening is primarily modeled via crystal size broadening using a refined Lorentzian function. Data from *ex post facto* SXRD runs are plotted as weight fractions.

3.4 Results and Discussion

Density functional theory guided thermochemistry permits down-selection of precursors for the reaction scheme, AFeO$_2$ + BiOX. A chemical reaction network scheme[16,60] based off of all entries from the Materials Project Database[37] in the A-X-Bi-Fe-O system, where A = Li, Na, K, Rb, Cs, Mg, Ca, Sr, Ba and X = F, Cl, Br, I, permits facile calculation of the reaction energies for reactions producing BiFeO$_3$ and a secondary phase, as found in metathesis style reactions. From these calculations, BiFeO$_3$ is stable only under finite pO$_2$ (specifically pO$_2$ > 70 torr from Grand Potential calculations). The Grand Potential reaction energies for all 8610 reactions are compared with the "chemical potential distance" in Figure 3.1. The chemical potential distance,[16] can be used to select precursors that share a stable boundary on the equilibrium phase diagram; if the distance between two phases is zero, they form a stable 2-phase region in the high-dimensional phase diagram. Examination of the Pareto frontier along the bottom left edge of the histogram highlights several reactions for further experimental investigation. Reactions involving fluoride tend

to have the shortest chemical potential distance. This can reflect the sparse phase space of the database for fluorine ion containing phases, as well as the fewer number of phases of composition intermediate between the $A\text{FeO}_2$ precursor and BiFeO_3. Of the F-based reactions, K has the most negative energy of reaction, while Li and Na have the shortest chemical potential distance but still favorable reaction energetics.

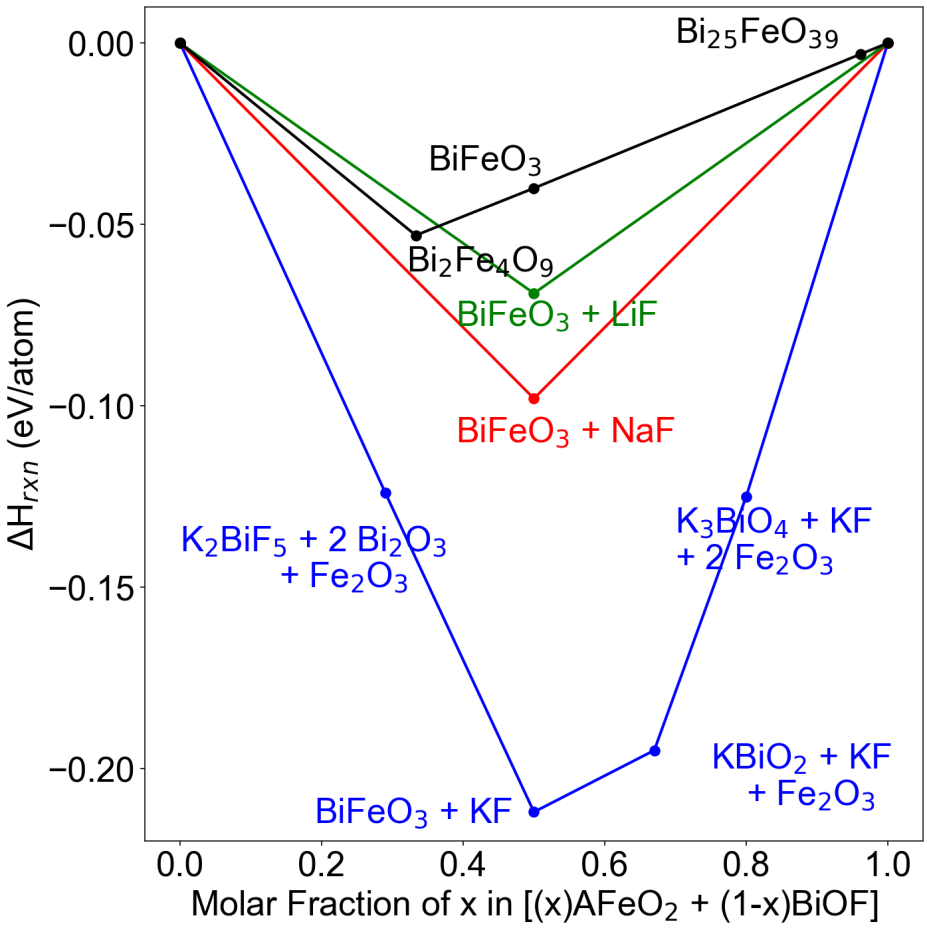

Figure 3.2: Examination of the thermodynamic convex hulls leading to BiFeO_3 formation illustrates that oxide-based reactions have a low thermodynamic competitiveness and (metathesis-based reactions have a significantly higher thermodynamic competitiveness relative to formation of undesired products (e.g., $\text{Bi}_2\text{Fe}_4\text{O}_9$ and $\text{Bi}_{25}\text{FeO}_{39}$). Within the ternary metathesis reactions, $\text{BiOF} + A\text{FeO}_2$, where A = Li, Na, K, K presents the biggest thermodynamic driving force for BiFeO_3 formation,though K-based reactions has potential for reaction intermediates.

Closer examination of the reactions, $A\text{FeO}_2 + \text{BiOF}$ reveals the different predicted thermodynamic outcomes. Shown in Figure 3.2, reaction of $\text{Bi}_2\text{O}_3 + \text{Fe}_2\text{O}_3$ (black line) has a

relatively low driving force, which is particularly non-competitive against the formation of $Bi_2Fe_4O_9$.[51,52] Such geometry of a convex hull has been shown to be useful in predicting ideal precursors for reactions,[58,61] as the lowest energy product on a compositionally-unconstrained convex hull is most likely to form first.[6,62] In stark contrast, expanding the chemical space to include an alkali and fluoride yields $BiFeO_3 + AF$ as the lowest energy product for an composition. From the convex hulls in Figure 3.2, it is apparent that both Li and Na based reactions are predicted to not have any possible alternative reactions, hence they have a low chemical potential distance. In contrast, the reaction $KFeO_2 + BiOF$ has the potential to form other phases (e.g., K_3BiO_4, K_2BiF_5, and $KBiO_2$), yet the overall reaction energy is significantly more negative. In all cases, the hyperdimensional chemistry[44] is predicted to avoid the formation of $Bi_2Fe_4O_9$ and $Bi_{25}FeO_{39}$ that plagues the reaction of $Bi_2O_3 + Fe_2O_3$.

From bulk laboratory-scale reactions $AFeO_2 + BiOX$, we identified that $KFeO_2 + BiOF$ produces $BiFeO_3$, whereas the other reactions yield a mixture of Bi-Fe-O phases. The reaction performs best at 860 °C and with a partial oxygen pressure of $p(O_2) = 70$ Torr, $KFeO_2 + BiOF \longrightarrow BiFeO_3 + KF$, though the KF dissolves during the quenching step (Figure 3.3(a)). From a time series of reactions performed at a furnace set point of 860 °C (see methods and Figure 3.3(c)), we observe that $BiFeO_3$ forms in the shortest time points measured but then starts to decompose in reactions longer than 1.5 min. For the shortest reactions ($t = 0$ min and 0.5 min), the reactants are no longer present; indexing the powder diffraction pattern reveals a mixture of $Bi_{13}O_{20}$, Bi_2O_3, $BiO_{0.55}F_{1.9}$, $Bi_4Fe_5O_{13}F$, $Bi_2FeO_3F_3$, KFe_2F_7, K_3FeF_6, $Bi_{25}FeO_{39}$. Reactions that produce LiF, NaCl, and KBr as byproduct phases also do not yield $BiFeO_3$ as the sole Bi-Fe-O phase (Figure 3.3(b)). In situ diagnostics of the reaction were used to gain further insight to the selectivity of this reaction.

In situ synchrotron powder X-ray diffraction of the reaction $KFeO_2 + BiOF$ illustrates a time-dependent decomposition of $BiFeO_3$ under the reaction conditions. PXRD data shown in Figure 3.4 illustrates that $Bi_{25}FeO_{39}$ already starts to form at the fastest data

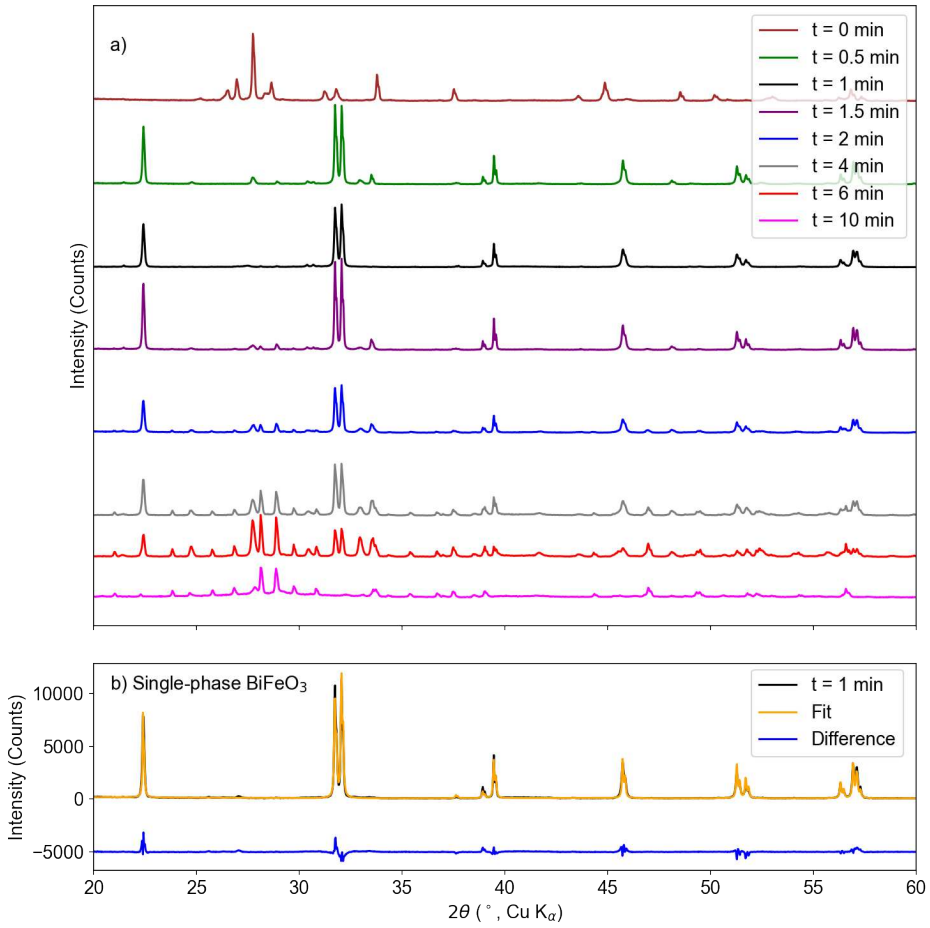

Figure 3.3: (a) Laboratory PXRD data of a series of BiOF + $KFeO_2$ reactions heated for 0 min to 10 min, illustrate that pure $BiFeO_3$ can only be obtained in a narrow time window. Heating beyond that time window promotes the formation of byproducts such as α-Bi_2O_3 and $Bi_2Fe_4O_9$. (b) Single Quenched reaction of BiOF + $KFeO_2$ after 1 min of heating and a 0.1 M HNO_3 wash. The reaction yields single phase $BiFeO_3$ by putting the open pellet directly into a furnace heated to 860 °C with $p(O_2)$ = 70 Torr; upon closing the furnace the T reads 835 °C. The sample remains at temperature for 60±5 s followed by rapid quench of the open ampule directly into water.

set collected upon equilibration of the capillary (heating rate ≈ 50 °C/min). The phase fraction of $Bi_{25}FeO_{39}$ grows in over time at the expense of $BiFeO_3$ (see inset). Together, these data illustrate the importance of both a very rapid heating rate as well as a rapid cooling rate, motivated by the narrow temperature window of stability of $BiFeO_3$.[55]

Quantitative phase analysis of the in situ diffraction data of $KFeO_2$ + BiOF, reveals a trend in decreasing phase fraction of $BiFeO_3$ as a function of time. The rate of this process increases with temperature, as higher temperatures show higher initial weighted scale

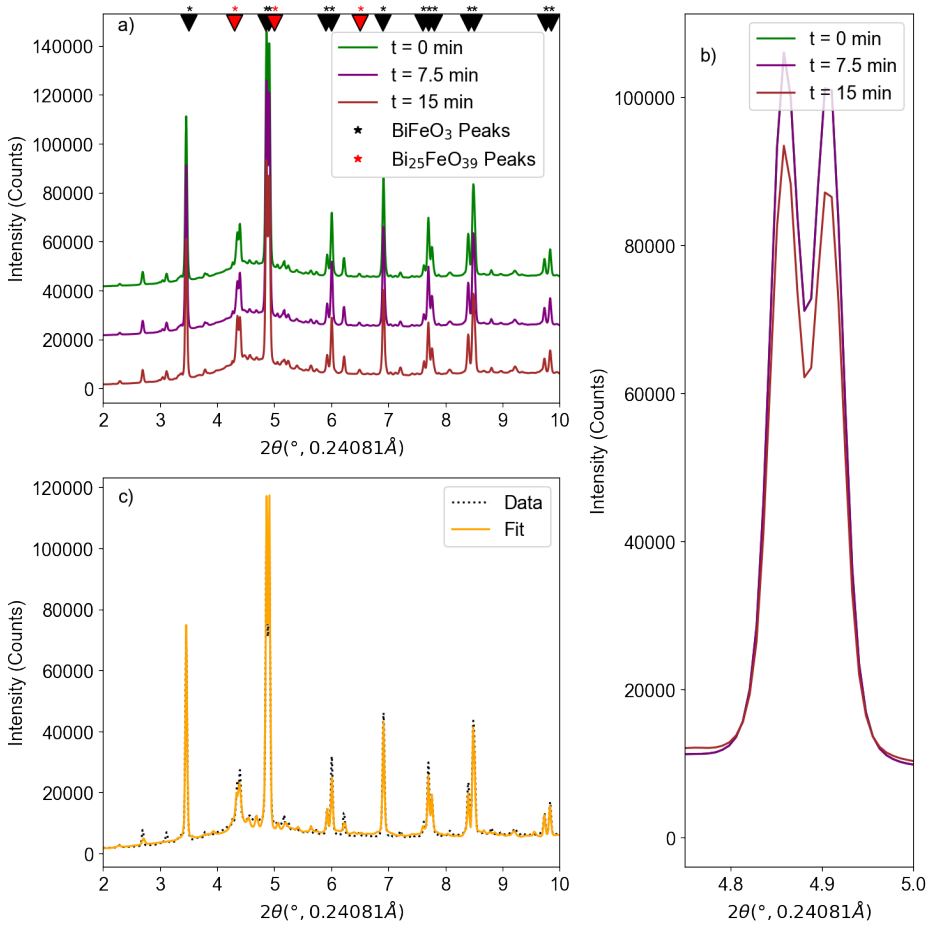

Figure 3.4: a) *In situ* synchrotron PXRD data collected from the reaction BiOF + $KFeO_2$ using a gradient furnace at short time points at 724 °C highlights the rapid formation of $BiFeO_3$ (e.g., it has already formed in the first time point) and its subsequent decomposition into $Bi_{25}FeO_{39}$ (b) Bragg peaks occurring solely from $BiFeO_3$ to illustrate the time-dependent decomposition. PXRD from t = 0 and t = 7.5 min overlap. (c) Rietveld analysis of the products of the reaction BiOF + $KFeO_2$ after 7.5 min.

factors (WSF) compared to lower temperatures; however, the rate of $BiFeO_3$ decomposition is faster at higher temperatures. It is possible that these reactions are too fast to observe the maximum amount of $BiFeO_3$.

In contrast, the reactions $NaFeO_2$ + BiOF and $LiFeO_2$ + BiOF do not form $BiFeO_3$. Both reactions form $Bi_7F_{11}O_5$ and other Fe-deficient phases which changes the global chemical equilibrium towards the formation of $Bi_{25}FeO_{39}$ and $Bi_2Fe_4O_9$ instead of forming $BiFeO_3$ (see Appendix B Figures B.2-B.3).

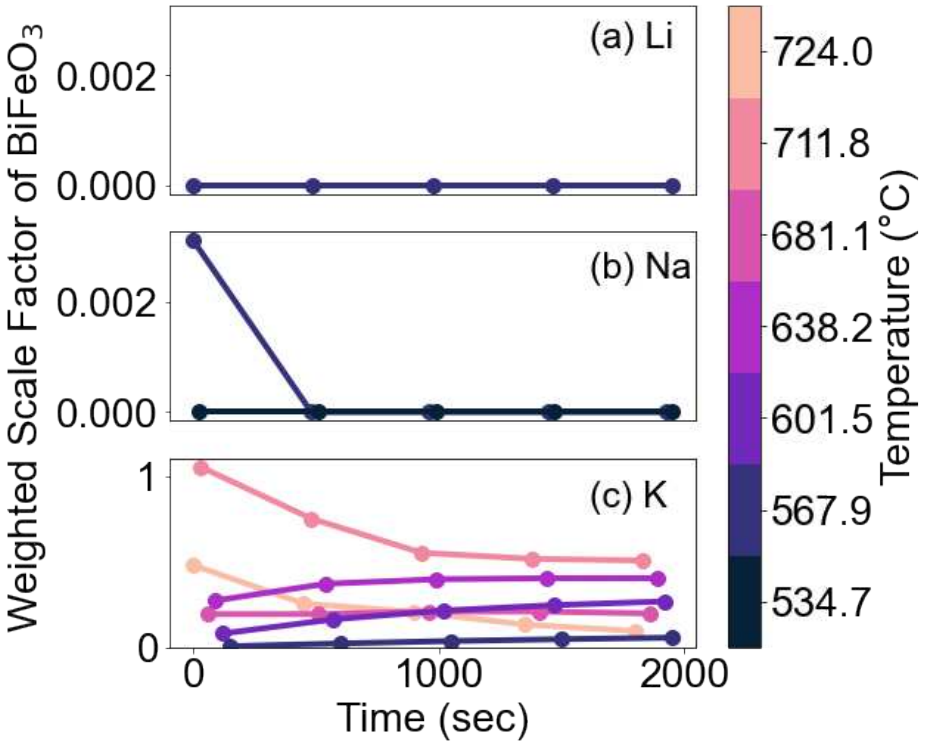

Figure 3.5: Weighted scale factor of $BiFeO_3$ obtained from Rietveld analysis of in situ synchrotron PXRD data. (a) BiOF + $LiFeO_2$ forms no $BiFeO_3$. (b) BiOF + $NaFeO_2$ forms $BiFeO_3$ only at around $T > 567.9$ °C and then decomposes rapidly (< 7.5 min). (c) In the reaction BiOF + $KFeO_2$, initial $BiFeO_3$ formation is relatively slower at lower temperatures and slowly decomposes at the higher temperatures studied. From the reaction temperatures T = 534.7, 567.9, and 601.5 °C, the peaked WSF in time illustrates that formation and decomposition reactions can occur in parallel.

The decomposition of $BiFeO_3$ at longer reaction times can be attributed to the shape of the multi-component phase diagram and its limited region of temperature-dependent thermodynamic stability. Previous work has shown a limited region of thermodynamic stability of $BiFeO_3$ between 767 °C (1040 K) and 852 °C (1125 K). At lower temperatures ($T <$ 767 °C; 1040 K), $BiFeO_3$ decomposes into $Bi_2Fe_4O_9$ and $Bi_{25}FeO_{39}$.[55] At higher temperatures ($T >$ 852 °C; 1125 K), $BiFeO_3$ undergoes a peritectic decomposition reaction.[63] The *in situ* PXRD data shown in Figure 3.4 collected at T = 724 °C supports the high temperature decomposition reaction.

Intentional incorporation of impurity elements in the Bi-Fe-O system have been shown to lead to significant formation of the $Bi_2Fe_4O_9$ and $Bi_{25}FeO_{39}$ phases.[51] This was previously attributed to the lever rule action that exists by pulling the average composition

into a 3-phase field rather than on the precise stoichiometry, $BiFeO_3$. The shape of this 3-phase region is such that the phase fraction of $BiFeO_3$ in equilibrium becomes greatly diminished. The metathesis reactions studied here also have the potential for forming substituted phase (e.g., $Bi_{26}F_2O_{38}$[64] and $Bi_{19}F_3O_{27}$[37]) that could have an comparable effect on the global equilibrium that leads to degradation of the $BiFeO_3$ at long time points. The compositionally-unconstrained convex hull between $AFeO_2$ and BiOF (Fig. 3.2) shows that $BiFeO_3$ has the most favorable reaction energy, suggesting that it should also have the fastest nucleation rate, relative to the formation of other Bi-Fe-O phases.[62,65] However the chemical potential distance informs us that reactions with a short chemical potential distance (e.g., precursors $LiFeO_2$ and $NaFeO_2$, see Figure 3.1) lead to formation of $BiFeO_3$. We suspect that $BiFeO_3$ decomposes before the first time point was collected during *in situ* XRD ($t < 7.5$ min, Figure 3.5). In contrast, reactions with $KFeO_2$ show the formation of myriad different phases at short time points ($t < 0.5$ min, Figure 3.3), reflective of the finite chemical potential distance to $BiFeO_3$ and KF (Figure 3.1(a)). The metathesis reaction with $KFeO_2$ slows down the reaction towards $BiFeO_3$ and slows down the decomposition of $BiFeO_3$ such that the reaction can be practically quenched.

Quantitative analysis reveals that $BiFeO_3$ decomposes into Fe_2O_3, Bi_2O_3, and $Bi_{25}FeO_{39}$ (see Appendix B). Owing to the much higher scattering factor of bismuth compared to iron, the signal of iron oxide is very weak compared to the signals from phases that contain bismuth. This is supported by the observation of Bi_2O_3, and $Bi_{25}FeO_{39}$ as the predominant phases. To maintain stoichiometric amounts, Fe_2O_3 must be present. Levin et al. commented on the possibility of a low scale factor from iron phases owing to the much higher scattering factor of bismuth compared to iron.[66] Upon closer careful investigation of the in situ data, we see an overlap of Fe_2O_3 with the peaks for Bi_2O_3 and the phase with $Bi_{25}FeO_{39}$ with the spacegroup *I23*.

The phase $BiFeO_3$ decomposes into γ-Bi_2O_3 or the isostructural phase $Bi_{25}FeO_{39}$, depending on the reaction temperature. Recent work revisited the synthesis of $BiFeO_3$ using

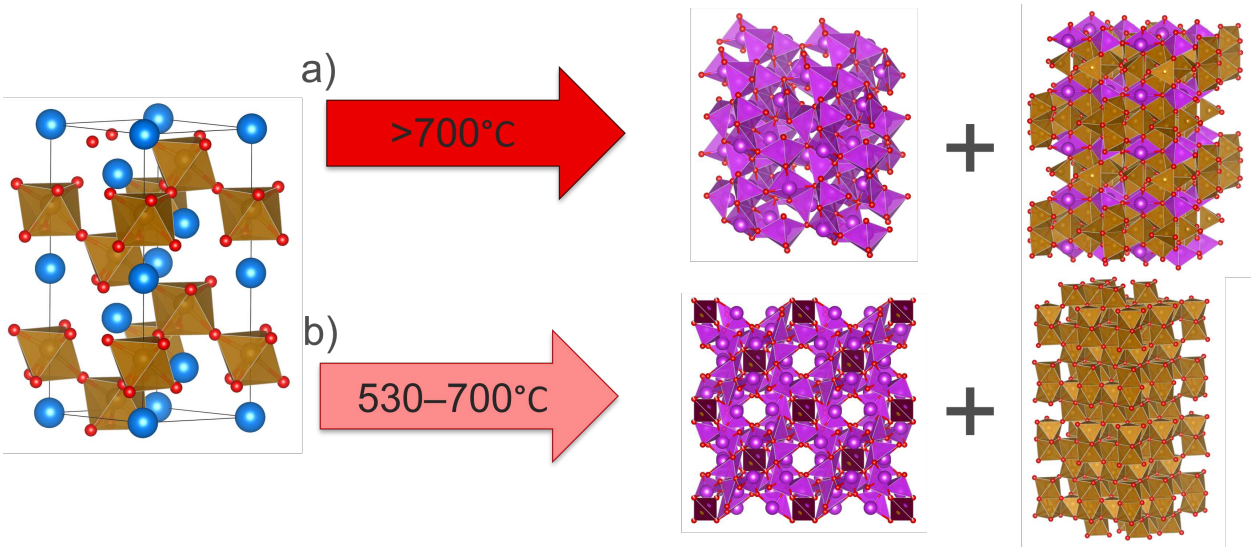

Figure 3.6: Illustrated reaction steps of the decomposition reaction of $BiFeO_3$ at (a) 700 °C and (b) 530-700 °C. At temperatures above 700 °C, The products are γ-Bi_2O_3 and $Bi_2Fe_4O_9$. Between 530-700 °C, $BiFeO_3$ decomposes to $Bi_{25}FeO_{39}$ and Fe_2O_3.

in situ PXRD. Westley, et al. elaborated on the proposition, made by Bernando, et al. that Bi_2O_3 diffuses into Fe_2O_3 to form the ternary phase.[53,67] In the process, undesirable ternaries can form and the chemical gradient causes the reaction to proceed towards a core-shell structure as an intermediate, namely $Bi_{25}FeO_{39}$. $Bi_{25}FeO_{39}$ is a cubic structure (*I23* space group). γ-Bi_2O_3 is structurally analogous to $Bi_{25}FeO_{39}$, but they differ by the occupancy (or vacancy) of iron atoms. Therefore, it is challenging to discern between these two phases. As pointed out by Westley, et al. a comparison of the lattice parameter can suggest one phase over the other, where γ-Bi_2O_3 has a literature value of 10.27 Åand 10.19 Åfor $Bi_{25}FeO_{39}$. From in situ diffraction data, the lattice parameter of the phase with an *I23* spacegroup has been plotted as a function of time at the respective temperatures between 530 - 730 °C (Figure 3.7). The time window corresponds to time points after $BiFeO_3$ starts to decompose. At the highest temperature (above 710 °C), the lattice parameter fluctuates around 10.22 Åsuggesting that the phase is $Bi_{25}FeO_{39}$. Any observed temperature below 710 °C the lattice parameter is above 10.24 Å. The smallest lattice parameter at the highest temperature indicates that the lattice parameter is not a result of thermal expansion but rather comes from compositional differences at the different temperatures. Based on

the temperature-dependent decomposition products, we propose the following possible decomposition reaction steps:

$$4\mathrm{BiFeO_3} \longrightarrow 2\gamma{-}\mathrm{Bi_2O_3} + 2\mathrm{Fe_2O_3} \longrightarrow \mathrm{Bi_2Fe_4O_9} + \mathrm{x}\gamma{-}\mathrm{Bi_2O_3} + 1{-}\mathrm{xBi_2O_3} \tag{3.2}$$

preferred at low temperatures (530 - 730 °C), and,

$$25\mathrm{BiFeO_3} \longrightarrow \mathrm{Bi_{25}FeO_{39}} + 12\mathrm{Fe_2O_3} \tag{3.3}$$

at high temperatures (above 710 °C) The reaction steps are illustrated in Figure 3.6

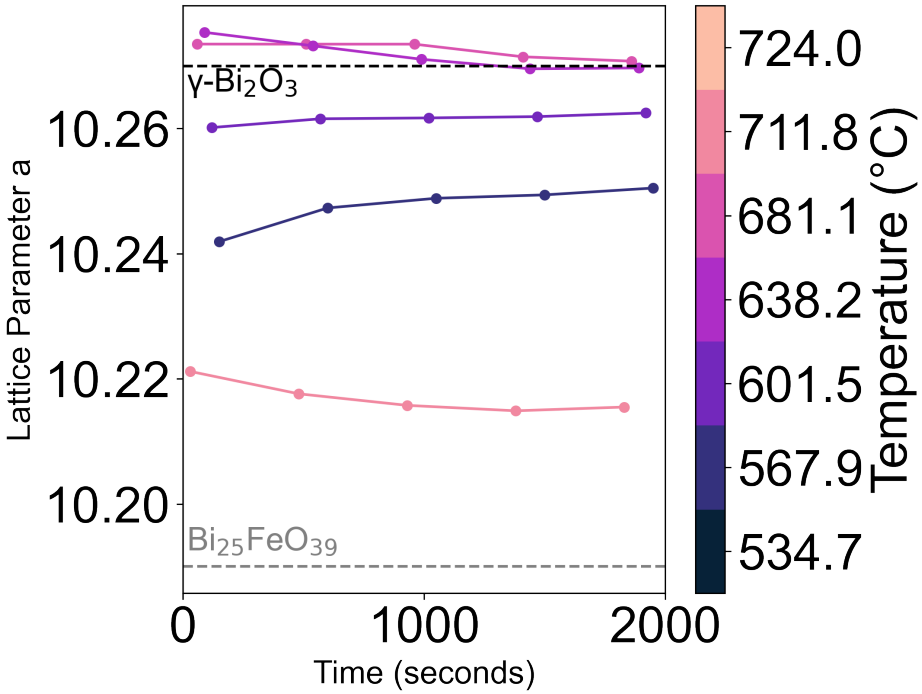

Figure 3.7: Lattice parameter of the phase with the space group *I23* from in situ PXRD at various reaction temperatures as a function of time. The phase is suspected to be between γ-Bi_2O_3 or the distorted isostructural phase $Bi_{25}FeO_{39}$. Consistent, yet different lattice parameters at given temperatures, hint to temperature dependent decomposition products of $BiFeO_3$.

In the search for thermodynamic proxies for reaction kinetics, the synthesis of $BiFeO_3$ reveals a need for counter-intuitive reaction design. Previous work has shown how large

driving forces,[62] low nucleation barriers,[65] and optimally-shaped phase diagrams[58,61] are valuable considerations in reaction design. The metathesis-based approach here highlights how the local rapid equilibration can be detrimental, particularly as heat removal from a system is required. The use of the $KFeO_2$ precursor provides a favorable reaction for producing $BiFeO_3$ relative to other Bi-Fe-O phases, but it does so with a short window of opportunity that allows for the removal thermal energy from the reaction that is needed to prevent $BiFeO_3$ from decomposing due to the 3-phase (or more) region of the multi-component phase diagram.

3.4.1 Conclusions

$BiFeO_3$ is synthesized from the rapid metathesis reaction of $KFeO_2 + BiOF$ in $p(O_2) =$ 70 Torr at ca. 810-830 °C for 1 min followed by a rapid quenching in iced brine. Due to the rapid local equilibration of metathesis reactions, the slightly less selective reaction using $KFeO_2$, relative to $LiFeO_2$ and $NaFeO_2$ as predicted by first-principles based thermochemical analysis, guides the reaction towards $BiFeO_3$ and appears to slows down the decomposition of $BiFeO_3$, as determined from *in situ* synchrotron X-ray diffraction. This enables the reaction to be thermally arrested before decomposition into other Bi-Fe-O phases. We suspect that the multi-dimensional phase diagram offers a thermodynamic local minimum that favors the formation of $BiFeO_3$. While these results highlight the missing knowledge regarding real reaction kinetics in predictive synthesis, they highlight the utility in how thermodynamic proxies for reaction selectivity can capture aspects of reaction design and assist in narrowing down precursor choices

Chapter 4

Kinetic Insights to Solid-state Metathesis Reactions

Overview

This chapter investigates the reaction kinetics of three select metathesis reactions towards $YMnO_3$, specifically, the kinetics on $YOCl + AMnO_2$ and their formation towards $YMnO_3$ were characterized over time. The chapter introduces an overview of kinetic studies in solid-state reactions. By measuring the time dependence of these reactions, we are able to identify three kinetic regimes of reactions: interface limited, diffusionlimited and geometry limiteded regimes. Analysis of the time-dependent power law of the phase fractions allows limiting process based on simple models. The reactions of Mg and Ca are interface limited kinetics, but differ in their reaction rate. The Li metathesis reacts the fastest and is limited by diffusion and eventually by geometric constraints.

4.1 Introduction

Understanding reaction kinetics and how to use kinetics to influence product differentiation is a difficult problem in solid-state chemistry. Here, we make a simplifying assumption that solid-state reactions progress through three different regimes of limiting processes. (Fig. 4.1).[3] The first regime is defined by the limited transport across an interface. At the interface, there is a discontinuity of the chemical potentials (Fig. 4.1(b), left). If there is no discontinuity in chemical potential, reactions are proposed to follow

* Reprinted with permission from G.T. Tran, A. Wustrow, D. O'Nolan, C.H. Liu, M.J. McDermott, B.C. McBride, K.W. Chapman, S.J. L. Billinge, K. A. Persson, G. Ceder, and J.R. Neilson, *Manuscript in preparation*. G.T.T, A.W and J.R.N. conceptualized the project. C.H.L assisted with *in situ* X-ray diffraction experiments. D. O'N. provided essential equipment. A.W., B.C.M., and G.T.T. performed the experiments, and G.T.T wrote the manuscript with guidance of J.R.N.

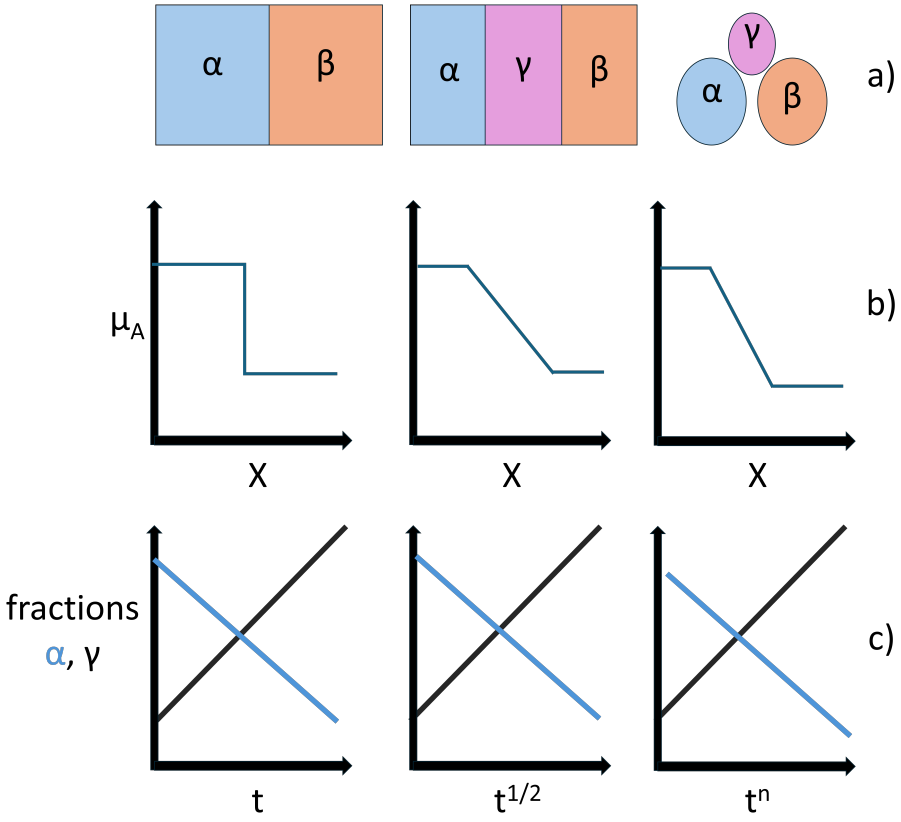

Figure 4.1: a) Model representation of solid-state reaction (a), their chemical potential gradient (b), and the phase fraction as a function of time (c). When the chemical potential gradient between the reactants α and β is discontinuous, the reaction is interface-limited and the consumption of reactants and production of new phases is linear in respect to time (left). When the chemical potential gradient between the reactants α and β is continuous, the reaction is diffusion-limited and the consumption of reactants and production of new phases is linear in respect to $t^{1/2}$ (center).When the chemical potential gradient between the reactants α and β is continuous, but the consumption of reactants and production of new phases is linear as a function of t^n ,where n is non-zero, then the reaction is neither dominated by diffusion of the reaction interface and may be subject to other factors (right).[3]

diffusion limited growth down the chemical potential gradient (Fig. 4.1(b), center). The third regime considered is a geometry limited regime, which may be controlled by particle shape, size, and contact (Fig. 4.1 (b) right).

For example, particle contact can limit reaction kinetics as studied in topotactic ion-exchange reaction of Li for Na in $NaFeO_2$.[68] Each aforementioned kinetic regime is not necessarily inherently slower or faster than the other. The limiting reaction kinetics are

closely tied to the system of interest. Therefore, it is imperative to consider intrinsic and extrinsic properties of the reaction system that can influence the thermodynamics that define the chemical potentials of the system, and means by which the reaction takes place (e.g., the factors that strictly limit kinetics). Therefore, here we primarily consider the relative time dependence for each individual system across a range of temperatures.

In our explanation on the kinetic regime (Figure 4.1), we assumed a simple binary reagent systems that form one product. In most reactions, that is less likely to be the case. Therefore, kinetics studies on more complex, yet useful synthesis techniques, will assist in our pursuit of synthetic control in the solid-state. Solid-state metathesis reactions are useful in that they require milder reaction conditions.[26] Furthermore, they demonstrated product selectivity depending on the thermodynamics of the precursor choices, but without elaboration of reaction kinetics.[15,16] Here, we revisit the reactions of $YOCl + AMnO_2$, where *A* is Li, Mg, and Ca. In this contribution, we investigate the limiting kinetics throughout the reaction for achieving local equilibrium at different temperatures.

4.2 Methods

4.2.1 Precursor Synthesis

Orthorhombic $LiMnO_2$ was synthesized by reacting Li_2CO_3 (Baker, 99.3%) and MnO_2 (Alfa Aesar, 99.9%) with 15 mol% excess Li_2CO_3. The powders were milled using an 8000 M Spex MixerMill within a 30 mL polypropylene bottle placed inside the steel Spex jar. The powders were milled for 90 min with 5 mm spherical yttria-stabilized zirconia milling media in a 2:1 weight ratio of media to sample. The resulting gray powder was pelleted using $\sim$1 short ton of force. The pellets were placed inside beds of sacrificial powder in an alumina boat and heated under flowing argon. The samples were heated at 600 °C for 4 h and 900 °C for 48 h with heating and cooling rates of 10 °C/min.

$CaMn_2O_4$ was synthesized by mixing $CaCO_3$ and MnO_2 in a 1:2 molar ratio and heating to 1300 °C for 2 weeks in air, with regrinding every 4 days. $MgMn_2O_4$ was synthesized

through a sol–gel route, in which $Mg(NO_3)_2$ and $Mn(NO_3)_2 \bullet 6H_2O$ were dissolved in water with a molar excess of citric acid. After stirring for 3 h, the mixture was heated to allow the water to boil off, leaving behind an orange foam. The orange foam was heated to 650 °C and cooled slowly.[69] The slow cooling is performed to prevent site mixing (i.e., site inversion) between Mg and Mn sites in the spinel structure.

4.2.2 Synchrotron X-ray Diffraction

Synchrotron X-ray diffraction (SXRD) data were collected at beamline 28-ID-2 with a wavelength of 0.19319 Å at the National Synchrotron Light Source II at Brookhaven National Laboratory. Data of the reaction progress were obtained with a gradient furnace, where each horizontal position is calibrated and defined to a temperature.[19] The gradient furnace ensures its temperature gradient through scaling densities of heating elements along a quartz capillary (Friedrich & Dimmock). Samples were packed into 1.1 mm outer diameter, 0.9 mm inner diameter quartz capillaries in an argon-filled glovebox. This capillary was then brought out of the glovebox and sealed under vacuum ($\leq$20 mTorr). Calibration of detector curvature was performed using CeO_2 at all points along the gradient furnace using pyFAI.[34] SXRD data were collected on a PerkinElmer plate detector at 1400 mm distance and 1480 mm at two different visits to the light source. Using a PID-controlled power source, a horizontal temperature range of 300-800 °C along the capillary was created. The temperature at a given position was calibrated with NaCl and its thermal expansion.[20] Multiple time points were collected at each temperature point at an interval of 11 min for up to five separate time points. Samples were then cooled at an approximately 5 °C/min rate. Ex situ diffraction data were collected afterwards.

4.2.3 Powder X-ray Diffraction

Quantitative phase analysis of X-ray diffraction data was performed using the Rietveld method with TOPAS v6 software package. The following assumptions were made for consistent analysis: Atomic displacement parameters were fixed to a value of $B = 1$ Å^2,

and peak broadening is primarily modelled via crystal size broadening using a refined Lorentzian function. Data from *ex situ* SXRD runs are plotted as weight fraction.

4.3 Results

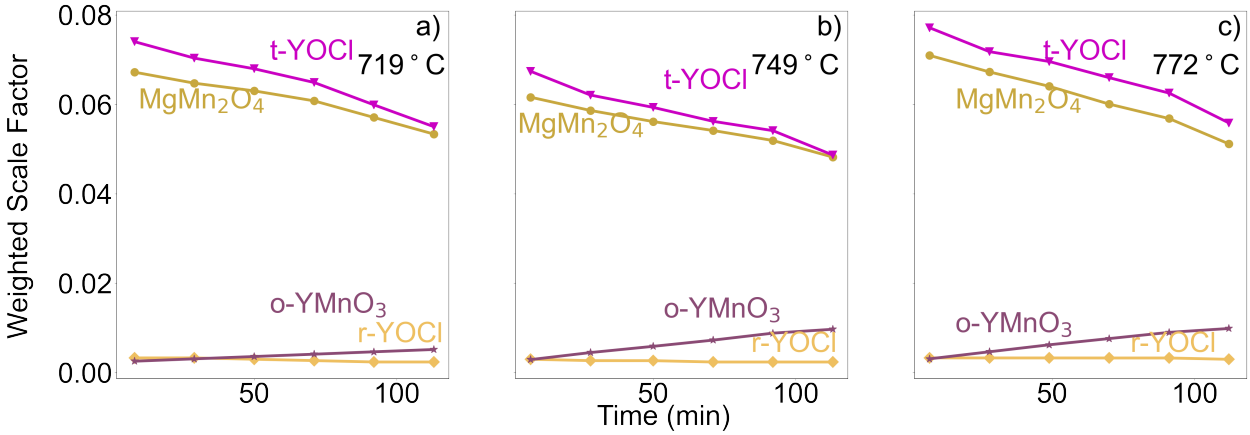

Figure 4.2: Phase distribution from isothermal reactions illustrated by their weighted scale factors at different temperatures (a)719 °C, (b) 749 °C, and (c) 772 °C in a gradient furnace for the reaction of $MgMn_2O_4 + 2\,YOCl$.

The reaction pathway towards $YMnO_3$ varies based on the *A* cation used. The phase evolution suggest that metathesis reactions that proceed through crystalline intermediate phases have faster kinetics. Here we compare the metathesis reactions $A_xMnO_2 + YOCl \longrightarrow A_xCl + YMnO_3$ where A is Li, Ca, or Mg. Using the gradient furnace (see Methods), the time- and temperature-dependent product distributions of the *in situ* reactions were determined using the Rietveld method and plotted in Figures 4.2-4.4. The weighted scale factors were plotted at a fixed reaction temperature as a function of reaction time (2 h total).

Ca and Li metatheses form a crystalline halide salt and the intermediate Y_3O_4Cl while the Mg metathesis forms Mg-substitute $YMnO_3$ directly without intermediates. $MgMn_2O_4$ shows little reactivity with YOCl. The Mg reaction only forms Mg-substituted $YMnO_3$ $T >$ 700 °C.[11,18,70] Under the same reaction conditions, the Ca metathesis forms $YMnO_3$ through

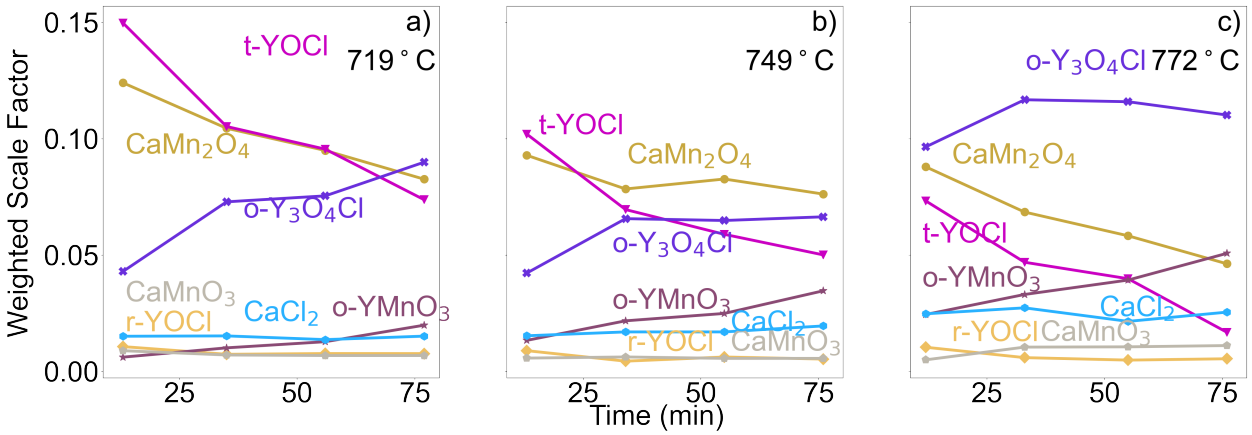

Figure 4.3: Phase distribution from isothermal reactions illustrated by their weighted scale factors at different temperatures (a)719 °C, (b) 749 °C, and (c) 772 °C in a gradient furnace for the reaction of $CaMn_2O_4 + 2\,YOCl$.

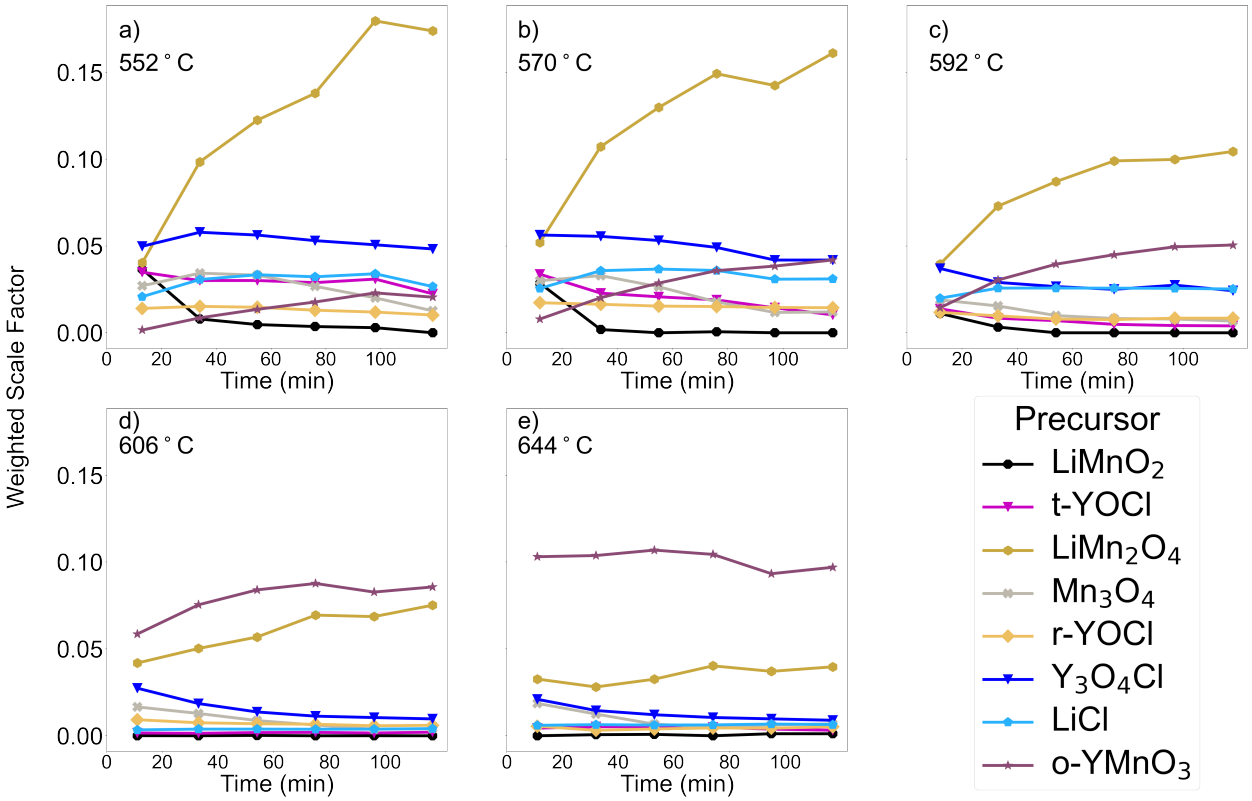

Figure 4.4: Phase distribution from isothermal reactions illustrated by their weighted scale factors at different temperatures for the reaction of $LiMnO_2$+YOCl as weighted scale factor from isothermal reactions at different temperatures ((a) 550 °C, (b) 570 °C, 592 °C, (d) 606 °C, and 650 °C) in a gradient furnace.

through the intermediate structure Y_3O_4Cl and crystalline $CaCl_2$. In contrast to Mg, Ca metathesis proceeds faster under identical conditions. The reaction $LiMnO_2 + YOCl \longrightarrow LiCl + YMnO_3$ proceeds even faster than Ca and at lower temperatures of 550 to 650 °C. $LiMnO_2$ first forms $LiMn_2O_4$ before it reacts with YOCl towards intermediate structure Y_3O_4Cl and crystalline LiCl. However, a direct comparison across different chemistries is challenging due to the influence of particle size distribution and packing densities.[68]

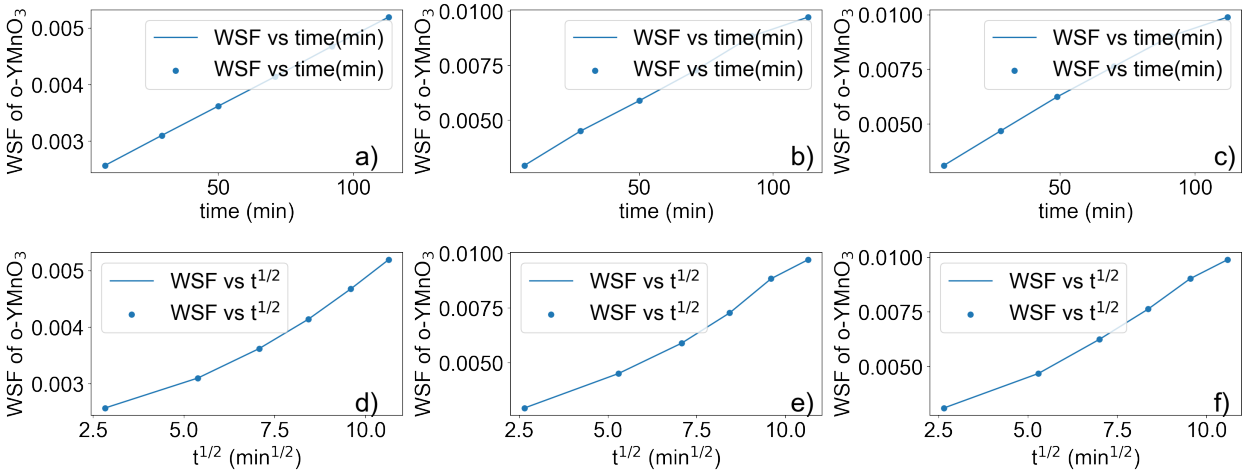

Figure 4.5: Weighted scale factor of $YMnO_3$ vs time and square root of time from isothermal reactions at different temperatures ((a and d)719 °C, (b and e) 749 °C, and (c and f) 772 °C) in a gradient furnace for the reaction of $MgMn_2O_4 + 2\,YOCl$.

Analysis of these *in situ* crystallographic data gives insight into the chemical process limiting the reaction kinetics as a function of time and temperature. As proposed by Schmalzried,[25] a linear increase in product phase fraction with time comes about from interface-controlled processes. In contrast, diffusion-limited phase formation follows a $t^{1/2}$ dependence. In Figures 4.5-4.7 the product phase fraction, inferred from the weighted scale factor from Rietveld analysis, are scaled by both linear-t and $t^{1/2}$ dependencies in order to identify a characteristic response. From the linear time dependence, it we infer that reaction kinetics of Mg and Ca are primarily governed by interfacial processes across

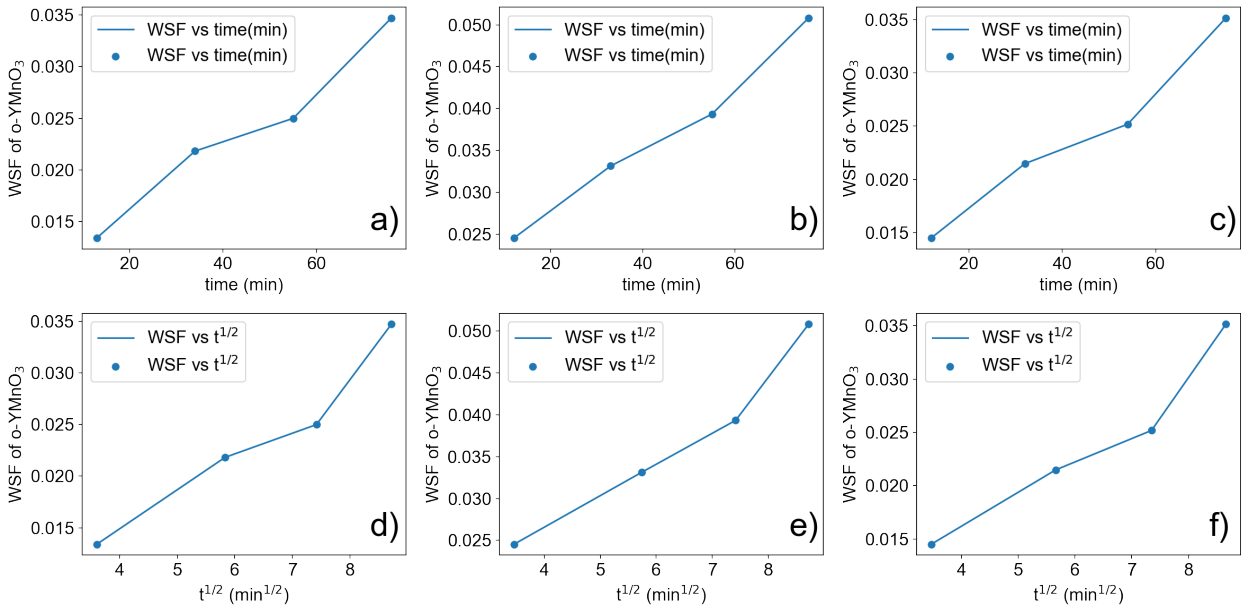

Figure 4.6: Weighted scale factor of $YMnO_3$ vs time and square root of time from isothermal reactions at different temperatures ((a) 719 °C, (b) 749 °C, and (c) 772 °C) in a gradient furnace for the reaction of $CaMn_2O_4 + 2\,YOCl$.

all times and temperatures. Li on the other hand, shows different time dependencies for each reaction temperature.

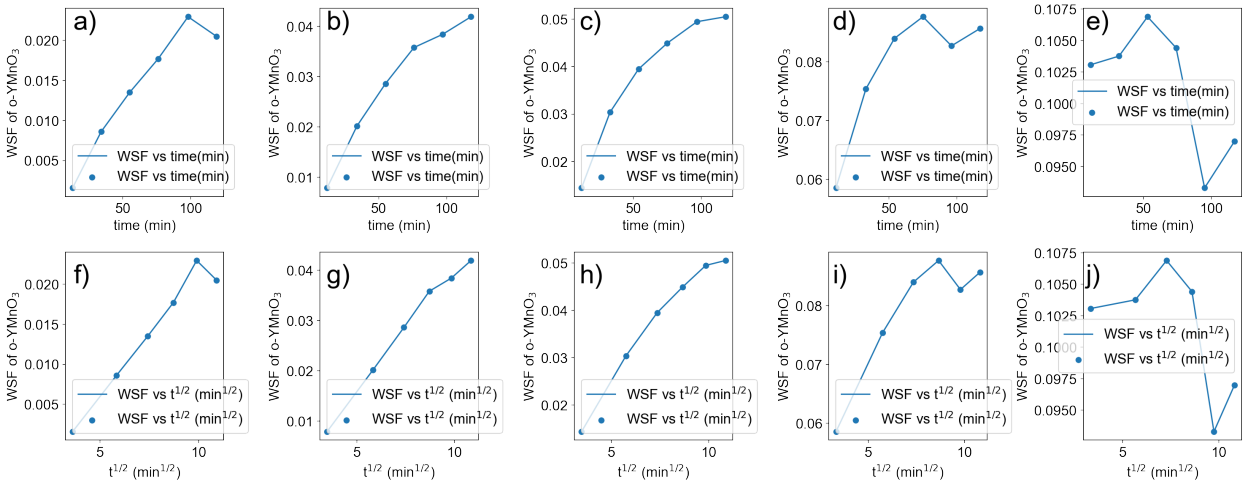

Figure 4.7: Weighted scale factor of $YMnO_3$ vs time and square root of time from isothermal reactions at different temperatures ((a) 552 °C, (b) 570 °C, (c) 592 °C, (d) 606 °C, and (e) 644 °C) in a gradient furnace for the reaction of $LiMnO_2 + YOCl$.

Under the same conditions and on both time scales, Mg and Ca reactions consume their reagents and form their products at a linear rate, but Ca proceeds faster and through the intermediate Y_3O_4Cl. The Li metathesis reaction begins with a linear rate of $YMnO_3$ formation at 552 °C. At 570 °C, the rate of formation shifts away from a linear trend on both time scales. Above 600 °C the Li reaction enters a geometry controlled kinetic regime, or some process distinct from characteristic interface- or diffusion-limited growth. We observe a slower growth in $YMnO_3$. At 644 °C, the weighted scale factor of $YMnO_3$ plateaus and may have found a local chemical equilibrium. The detection of intermediate phases suggests that the reaction kinetics are limited and slowed by a non-ideal particle contact between Y_3O_4Cl and $LiMn_2O_4$.

4.4 Discussion

The kinetics of the metathesis reactions are heavily impacted by the presence of reaction mediating intermediate crystal structures. Here, we observe that if reactions that do not form reaction intermediates, the time dependence is characteristic of a interface-limited process.

From previous studies, we know that reactions of $MgMn_2O_4$ and $CaMn_2O_4$ with YOCl require temperatures in excess of 700–750 °C for substantive reactivity. However, $CaMn_2O_4$ and $LiMnO_2$ can form oxygen defects, and forms Y_3O_4Cl as a oxygen-rich and chlorine deficient phase akin to YOCl, much more easily (at lower temperatures) than $MgMn_2O_4$.[11] This also leaves the intermediate Mn_3O_4, however; we do not observe Mn_3O_4 in the *in situ* scans of the Ca reactions. The reaction between $MgMn_2O_4$ and YOCl to form $YMnO_3$ and $MgCl_2$ has a positive ΔG_{rxn} at the temperatures investigated in this study and therefore should not spontaneously occur.[11] However, those calculations do not consider the thermodynamic favorability of Mg substituting into $YMnO_3$, which is what is experimentally observed through the unit cell of $YMnO_3$ that contracts upon Mg substitution.[18]

In each case, the reaction requires the formation of a defective intermediate (or defective version of precursors/product). Relating this to chemical potential (Fig 4.1), if there is a discontinuity in chemical potential, the reaction can be limited by a process to relieve this discontinuity (e.g. an "interface" process). Here, the formation of defects serve as a means to shift the bounding chemical potentials of the reacting/producing phases as to smooth out discontinuities in chemical potential. In contrast, the Li-based system has a larger number of intermediates available as to decrease large discontinuities in chemical potential; there, transport through these phases is limiting instead.

4.5 Conclusion

The reaction kinetics of the reactions $MgMn_2O_4 + 2\,YOCl$, $CaMn_2O_4 + 2\,YOCl$, and $LiMnO_2 + YOCl$ were studied using isothermal X-ray diffraction. The presence of crystalline intermediate phases determine the rate-limiting mechanism that define the reaction kinetics.

The chemical potential between $MgMn_2O_4$ and YOCl is discontinuous owing to not forming cyrstalline intermediates. Therefore, the reaction is interface limited. $CaMn_2O_4$ and $LiMnO_2$ form defect-rich crystalline intermediates which allow a continuous chemical potential gradient. Both reactions quickly transition from interface to diffusion limited processes. In the case of the Li-based system, the formation of large numbers of different intermediates leads to limiting transport across particles, or geometrically restricted contact.

The kinetic regimes were estimated through simple linear model fits of the isothermal data. Continuous studies on the reaction kinetics, including more extensive modeling and calculations, will offer further insight into reaction mechanisms and another step closer to the selective synthesis paradigm. While this chapter does not encompass all aspects of solid-state kinetics, it hopefully serves the purpose to rather point out the sheer size and complexity of the topic and hopefully encourage future studies on kinetics with respect

to solid-state synthesis, perhaps specifically for metathesis reactions, which could be the topic of at least 1 if not more future Ph.D theses.

Chapter 5

Synthesis of $LiMoO_2$

5.1 Overview

The synthesis of Mo-based inorganic materials is challenging. Mo-oxides prefer an electronic configuration that result in oxidation states of zero or *VI* owing to the preferable electron configuration. Here, we present data of the attempts to synthesize $LiMoO_2$ as a precursor for $RE MoO_3$, where *RE* is a rare earth metal. The synthesis of stoichometric $LiMoO_2$ did not succeed and efforts were discontinued. While Mo-oxides with oxidation states between *III-V* are less likely to selectively form, nitrides might offer a promising phase space to explore valency-specific synthesis.

5.2 Introduction

Materials of the perovskite structure display a wide range of physical properties such as, ionic conductivity for potential battery applications, colossal magnetoresistance for data storage, and superconductivity.[71–73] Figen et al. attempted to synthesize $LaMoO_3$, but synthesized a lanthanum deficient $La_2Mo_3O_{12}$ monoclinic phase which is thermodynamically stable. Synthesis reports of Lanthanum/yttrium-molybdenum-oxides (LnMoO3) perovskites remain rare and often show that a derivative structure was formed with off-stoichiometry instead of the stoichiometric desired phase.[74] On one hand, one must provide sufficient temperatures to overcome the high diffusion barrier, but on the other hand, high reaction temperatures lose control over selectivity and form the systems that are thermodynamically most stable such as binary metal oxides rather than the desired functional material. Metathesis reactions are useful by lowering the reaction temperature with maximum thermodynamic driving forces by providing a thermodynamically stable side product,

for example a lithium halide salt. Here, we propose a metathesis reaction towards $LaMoO_3$,

$$\mathrm{LiMoO_2} + \mathrm{LaO}X \longrightarrow \mathrm{Li}X + \mathrm{LaMoO_3} \tag{5.1}$$

where $X =$ Cl ,Br. However, the synthesis of stoichiometric $LiMoO_2$ is nontrivial. $LiMoO_2$ is a layered structure with edge-sharing MoO_6 octahedra that form the MoO_2 layers that are separated by the lithium ions sitting between each layer.[75,76] This enables the material to be used in Li-ion batteries as cathode materials as it allows lithium to move in and out of the layer. Unfortunately, Mo does not prefer to retains a valence state of +3. Molybdenum oxides tend to have oxidation states of zero or *VI* owing to the preferable electron configuration of either [Kr]$5s^1 4d^5$ or [Kr], respectively. While many molybdenum oxides with a valence of +3 have been made, selective synthesis towards certain oxidation states remains challenging. We attempted to synthesize stoichiometric $LiMoO_2$. Efforts either resulted in the synthesis of Li-deficient phases or synthesizes phases that contain Mo^{6+}. We also contrast the capabilities of oxygen and nitrogen compounds to mend the valence state of molybdenum.

5.2.1 Methods

$LiMoO_2$ synthesis was attempted through conventional solid-state synthesis by mixing stoichiometric amounts of Li_2MoO_4 (Alfa Aesar, 99.95%) and Mo.[76] Inside an Ar glovebox, the reagent powders were ground and mixed, pelleted, and placed in an alumina crucible. The sample was sealed in an evacuated ($\leq$20 mTorr) silica tube and heated at 500 °C for 24 h, then ramped up to 900 °C for another 48 h. This yielded $Li_{1-x}MoO_2$.

$LiMoO_2$ was previously synthesized through Birch reductions.[77] Lithium deficient $Li_{1-x}MoO_2$ and 5 times molar excess solid lithium metal (0.0258 g) were mixed with 0.8106 g benzophenone (Alfa Aesar, 99%) in Tetrahydrofurane (Sigma-Aldrich, 99%). This forms a dark blue solution that is pyrophoric. Thus, the reaction was kept on the schlenk line under flowing N_2 and stirred for 1 d. The solid and the liquids were separated via can-

nula transfering the liquids into a separate flask under N_2. The solution is quenched with ethanol and the remaining powder was dried under N_2 before it was recovered.

Phases were identified with laboratory powder X-ray diffraction (PXRD) data collected on a Bruker D8 Discover diffractometer using Cu Kα radiation and a Lynx Eye XE-T position sensitive detector (Figure 5.1.

5.2.2 Results and Discussion

Solid-state syntheses towards $LiMoO_2$ was unsuccessful and resulted in Li-deficient phases (Figure 5.1). Quantitative phase analysis of X-ray diffraction data was performed using the Rietveld method with TOPAS v6 software package. Initial attempts to synthesized $LiMoO_2$ showed unreacted precursor remains of Mo as well as Li_2MoO_4 (Fig. 5.1(b)). We hypothesize that lithium volatilizes at high temperatures and therefore, does not remain in the van der Waals gaps of the $LiMoO_2$. The Li-deficient sample of $LiMoO_2$ was combined with 5 molar excess Li metal to participate in a Birch reduction. All Li_2MoO_4 reacted with the lithium ion to form more Li-deficient $LiMoO_2$ (Fig. 5.1(a)).

Molybdenum oxides are known to remain in oxidation states of zero and *VI* owing to the preferable electron configuration of either $[Kr]5s^14d^5$ or [Kr], respectively. The high stability of these configuration probes Mo-based systems to adapt to these valencies over others. While other valence states of Mo are known and reported, they are less common.[78] We attempted to circumvent these challenges by using a Birch reduction and use the lithium ions to intercalate into the lithium deficient phase, made from high temperature solid-state reactions.[77] Although, some fully lithiated $LiMoO_2$ formed, a significant amount remained lithium deficient. Owing to the difficulties of synthesizing stoichiometric $LiMoO_2$ as precursor for the metathesis reaction $LiMoO_2 + YOCl$, this project is discontinued. While the goal of synthesizing a new Mo-based perovskite with a rare oxidation state of *III* is exciting and would likely lead to interesting property measurements, the synthesis proved to be too ambitious.

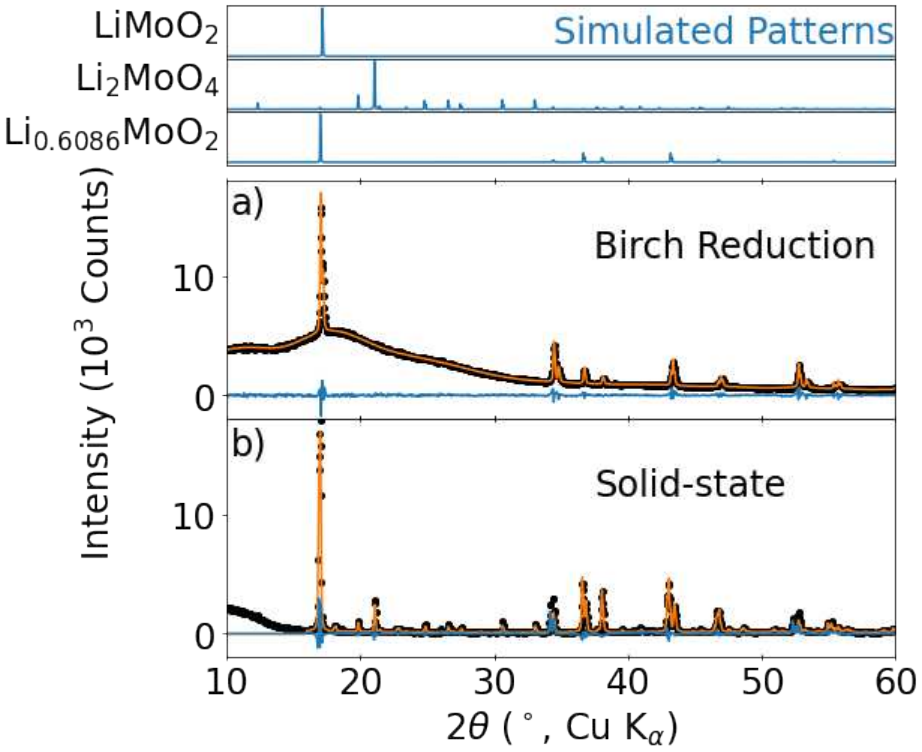

Figure 5.1: PXRD of $LiMoO_2$ via Birch reduction (a) and solid-state synthesis (b), respectively. Both synthesis routes yield lithium deficient phases while the solid-state method also had unreacted Li_2MoO_4.

Molybdenum phases with oxidation states between *III-V* are more common in nitrides. Ternary transition metal nitrides (TTMN) are an emerging class of materials with a variety of functional properties, including photoelectrochemical characteristics. Nitride materials are severely under-explored in contrast to oxygen. Bonding in ternary nitrides can range from ionic to covalent types. This is thanks to the moderate electronegativity of nitrogen ($\chi = 3.0$). It is more ionic than other pnictides that have been used in solar applications and yet more covalent than most oxides. The moderate electronegativity allows nitrides to be more defect tolerant for p-type doping and gain better charge-transport properties owing to the smaller band gaps as opposed to p orbitals of oxygen.[79–81] Owing to the moderate electronegativity, TTMNs, particularly with stoichiometric base composition A-B-N_2, can take advantage of the inductive effect and reductive effects to form stable phases.[82,83] In molecular chemistry, the inductive effect is commonly referred to a shift in the electron

density within a molecule. An electron donating group or atom shifts its electrons onto to a functional group or element that is more electronegative relative to the donating species which in turn redistributes to accommodate the additional electrons.[84] The donation onto a neighboring nitrogen leads to nitrogen reduction and oxidation of the bound B-site metal which implores the system to adapt to a structure with more nitrogen to accommodate the electron density and neutralize the oxidized and positively charged metal. The reductive effect refers to the rare phenomenon where the nitrogen atom acts as an electron donor for its neighboring metal to reduce the metal and becomes nitrogen poor to accommodate the less positive metal.[82,83,85,86] The inductive effect has been used to selectively tune stoichiometries in thin films, but no bulk synthesis has been reported to take advantage of it. Arca et al. published on the redox-mediated stabilization of crystal structures in the Zn-Mo-N phase space. Stoichiometries of $ZnMoN_2$ to Zn_3MoN_4 have been synthesized and tuned thanks to the inductive effect and molybdenum's ability to accommodate a wide range of oxidation states.[86] This project originally aimed to synthesize predicted novel Y-Mo-O perovskite materials with unusual oxidation states. Perhaps nitrides are more susceptible to a metathesis approach by taking advantage of the inductive/reductive effect from nitrogen.

5.2.3 Conclusion

Molybdenum oxides are known to remain in oxidation states of zero and *VI* owing to the preferable electron configuration. Synthesis attempts failed to synthesize stoichiometric $LiMoO_2$ and thus no successful synthesis towards $YMoO_3$ were conducted via metathesis. However, published research efforts for thin-film nitrides show promise in utilizing the wide range of the molybdenum valence states.

Chapter 6

Synthesis of Transition Metal Oxynitrides via Salt Flux Reactions

6.1 Overview

This Chapter summarizes the attempted syntheses towards Li-Mn-O-N and Li-Fe-O-N phases. The synthesis of oxynitrides is dependent on retaining the reactivity of nitrogen during the reaction at high temperatures and preventing the formation of N_2. The operating hypothesis assumes that alkali halide salt mixtures solubilize nitrogen and pins nitrogen's chemical potential to prevent N_2 formation and allow sufficient chemical potentials towards selective targets.

6.2 Introduction

Heteroanionic materials are defined as compounds with multiple or mixed anions in a single phase. They offer a wide variety of chemical compositions (oxynitrides, oxyhalides, oxysulfides) to choose from.[87] Our focus remains on the synthesis of oxynitrides. Oxynitride materials have been relatively unexplored (over 50000 oxide entries, and below 1000 oxynitride entries),[87] but they offer opportunities for fundamental studies on their structure-property relationship and potential advancements in energy transportation and storage.[88] Existing heteroanionic materials hold physical properties that are superior to compositions that employ only one type of anion.[88] The enhanced physical properties stem from the bonding interactions of multiple different anions bound to the cation. The differences in anionic characteristics give rise to unique electronic and atomic structures which are inaccessible to oxides and nitrides. Nitrides and oxynitrides are challenging to synthesize owing to the high thermodynamic stability of N_2 that is often more favorable

over the formation of other nitrides, especially at higher temperatures. One external factor to promote the reactivity of nitrogen with other elements and to synthesize heteroanionic compounds is a controlled atmosphere such as high-pressure nitrogen. Alternatively, thin-film syntheses of nitrides used atomic sputtering in excited-state nitrogen plasma. Ammonolysis uses ammonia to create a nitrogen-rich environment to synthesize oxynitrides from oxide powders. This method is generally reducting owing to the presence of H_2 gas during the decomposition of NH_3. Thus, most oxynitrides produced from ammonolysis contain electronpositive metals with a d^0 electron configuration.[89,90] This chapter's contribution conducted experiments based on the hypothesis that alkali halide salt mixtures solubilize nitrogen and pin nitrogen's chemical potential to prevent N_2 formation and allow sufficient chemical potentials towards selective targets. This chapter presents the attempted synthesis of Li_2MnON, and Li_2FeON.

6.3 Methods

A LiCl-KCl eutectic flux mixture was prepared by mixing 0.59 mol of LiCl (Sigma-Aldrich, 99.9%) with 0.41 mol of KCl (Sigma-Aldrich, 99.9%) into a homogeneous mixture with a total mass of roughly 3 g with a mortar and pestle inside an argon filled glovebox.

We attempted to synthesize "Li_2MnON" and "Li_2FeON" via LiCl−KCl flux reactions between Li_3N and Mn_2O_3, or Fe_2O_3 respectively. In each case, 0.0697 g of Li_3N was mixed inside an Ar filled glovebox with 0.1579 g of Fe_2O_3 (0.001 mol) and 0.1597 g of Mn_2O_3. About 0.5 g of the salt flux was added and mixed with the reactants. The mixture was pelleted and sealed in steel tubes by arc welding, which in turn were sealed inside a quartz tube to prevent rusting of the steel tubing ($\leq$20 mTorr). The reaction was heated at 800 °C for 12 h, then furnace cooled to room temperature. The resulting powder pellet was washed with methanol to separate the salt flux from the product. After the wash and solid extraction, a permanent magnet was held over the sample to see if the synthesis resulted in a permanent magnet(e.g., iron).

Phases were identified with laboratory powder X-ray diffraction (PXRD) data collected on a Bruker D8 Discover diffractometer using Cu Kα radiation and a Lynx Eye XE-T position sensitive detector.

6.4 Results and Discussion

Phase fractions of crystalline phases from synthesis attempts were collected on a Bruker D8 Discover diffractometer. The reactions did not yield phase pure products.

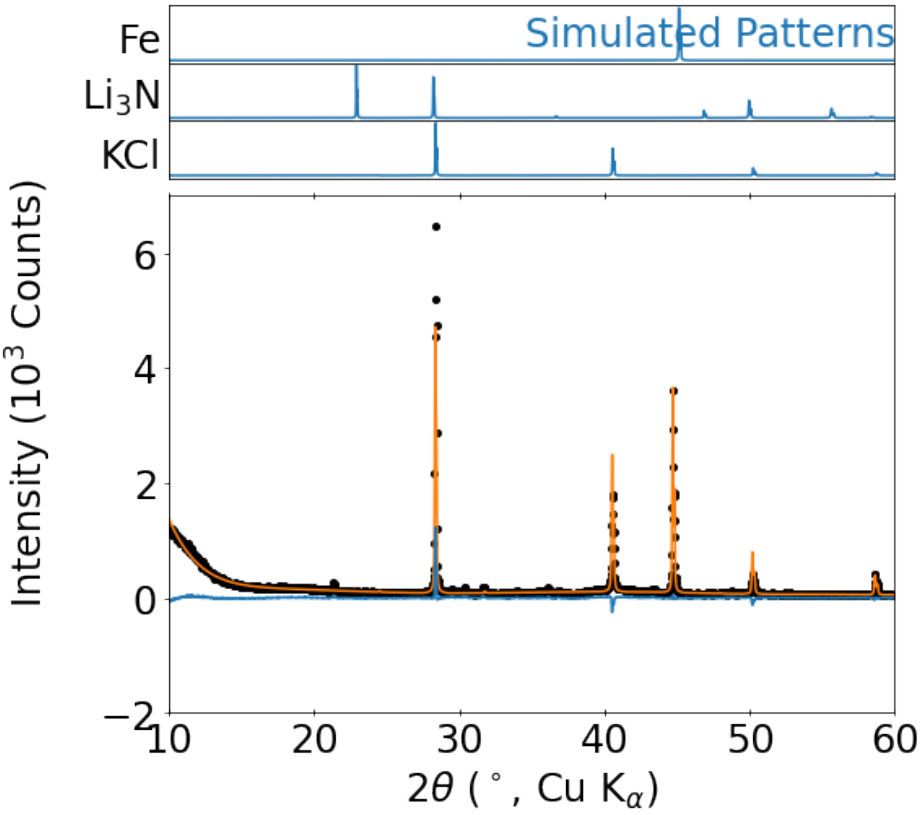

Figure 6.1: PXRD of synthesis attempts towards Li_2FeON.

The synthesis of Li_2FeON resulted in the formation of elemental iron (28.7%), some Li_3N (13.1%) and remaining KCl (58.2%) after several washes (Figure 6.1). The PXRD displays a few unidentified peaks that remain inconclusive, although Fe_2O_3 and Fe_4N did not fit the data through the Rietveld method. Prior to PXRD analysis, a permanent magnet

was held over the sample to quickly test for permanent magnetic properties. Unfortunately, PXRD revealed that the present iron powder is the permanent magnet rather than a novel oxynitride material. We hypothesize that Fe_2O_3 must have formed oxygen gas as well as nitrogen gas form Li_3N. No PXRD was taken of the interior wall of the steel tube to test for any reaction with the steel tubing. Furthermore, the presence of Li_3N suggest that Fe_2O_3 and Li_3N did not react with one another. Given the results of the refinements, the reaction is likely $Li_3N + Fe_2O_3 \longrightarrow 2\,Fe + 1.5Li_2O + N_2 + 0.25O_2$. No Li_2O can be detected in the PXRD owing to several washings of the sample prior to PXRD.

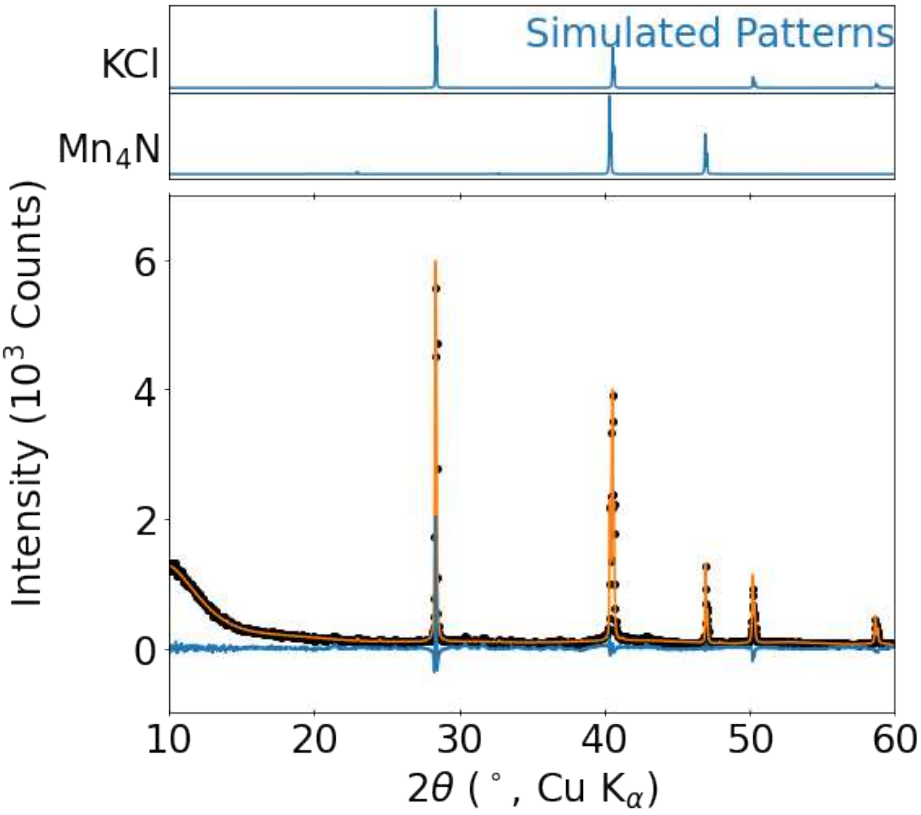

Figure 6.2: PXRD of synthesis attempts towards Li_2MnON.

The synthesis of Li_2MnON resulted in the formation of Mn_4N (19.9%) along with undissolved KCl (80.1%) (Figure 6.2). Given the results of the refinements, the reaction is likely $Li_3N + Mn_2O_3 \longrightarrow 0.5Mn_4N + 1.5Li_2O + 0.25N_2 + 0.75O_2$. No Li_2O can be detected in the

PXRD owing to several washings of the sample prior to PXRD. When a permanent magnet was held over the sample, the Mn_4N, ferrimagnet, was attracted by the magnet.[91]

6.5 Conclusion

The synthesis of novel oxynitrides is a challenging endeavor. No novel materials were synthesized in this contribution. However, it is important to note that these exploratory reactions highlighted the importance of experimental details. Alternative reaction vessels may be advantageous and prevent reactions between the container and the reactants. Furthermore, it is important and always necessary to design chemical processes with a balanced chemical equation.

Chapter 7

Hydrothermal Synthesis of Cs_2SbCl_6

Overview

Mixed valence perovskite materials bring opportunities to probe questions on the electronic structures in relation to the structural composition. Herein, we report the single crystal synthesis of Cs_2SbCl_6 via hydrothermal synthesis. We report different combination of reaction conditions to grow large single crystals for property measurements. Crystalline phases were identified through PXRD. We determined the band gap of Cs_2SbCl_6 via UV-visible diffuse reflectance spectroscopy along with the electronic conductivity through time-resolved microwave conductivity.

7.1 Introduction

Halide perovskite semiconductors are candidates for commercial photovoltaic devices. While promising perovskites already exists (such as $CH_3NH_3PbI_3$), alternative materials could improve the selection and reduce the necessity to rely on toxic elements such as lead.[92] Vacancy-ordered double perovskites (VODP) are a derivative of the perovskite structure. The structure is derived by doubling the perovskite unit cell from ABX_3, taking away every other B-site cation which results in A_2BX_6 with isolated octahedra and vacancies between the octahedra.

Many revolutionary photovoltaic materials display ns^2 electron configurations. This opens up questions about the fundamental mechanics behind the properties of VODPs. At the forefront of materials that ignited interest is Cs_2SnI_6. Depending on the synthesis and

---

* G.T.Tran and J.R.Neilson conceptualized the project. Large single crystals of Cs_2SbCl_6 were provided by P. Bhatt and R.G. Palgrave. D.C. Asabiah and O.G.Reid conducted photoconductance measurements. G.T.T. performed hydrothermal syntheses of Cs_2SbCl_6 crystals.

measurement methods Cs_2SnI_6 is reported to have a black coloring with an optical band gap ranging from 1.25 to 1.62 eV. Physical property measurements point out that Cs_2SnI_6 is typically a n-type semiconductor, but it can exhibit p-type conductivity under the right doping conditions.[93,94]

Cs_2SbX_6 are VODPs that have mixed valency for antimony. The isolated octahedra with mixed valency allows for studies that probe the impact of each Sb valency on the electronic structure and their properties including the optical gaps and charge transport behavior. The nominally average valence state "+4" disproportionate into +3 and +5. Thus, we can write a structural formula as $Cs_4Sb'\ Sb''X_{12}$, where Sb′ and Sb″ are +3 and +5, respectively. While this contribution is motivated to attain a deeper understanding of the structure-property relationship within $Cs_4Sb'Sb''X_{12}$ VODPs, we report herein the hydrothermal crystal growth of Cs_2SbCl_6 that yields single crystals suitable for electronic studies. We determined the band gap of Cs_2SbCl_6 via UV-vis diffuse reflectance spectroscopy along with the electronic photoconductivity through time-resolved microwave conductivity.

7.2 Methods

7.2.1 Preparation of Cs_2SbCl_6 powder

Sb_2O_4 powder was synthesized via solid-state synthesis. 2 g of Sb_2O_3 (Alfa Aesar, 99%) was placed in a boat crucible and heated up in air to 500 °C within 3 h. The reaction was held at 500 °C for 15 h and cooled down to room temperature within 2 h. Polycrystalline powders of Cs_2SbCl_6 were synthesized via solution precipitation following previous publication on Cs_2SbBr_6.[92,95] 0.872 g of Sb_2O_4 were dissolved in approximately 10 mL of HCl (Sigma-Aldrich, 37 %) inside a round bottom flask at 110 °C for about one week. 2 g of Cs_2CO_3 (Sigma-Aldrich, 37 %) were dissolved in approximately 5 mL of HCl and added to the dissolved Sb_2O_4. Upon mixing, the solution changes color to a deep black-purple. The

solution was stirred for at least 30 min. The precipitate Cs_2SbCl_6 was then filtered from the solution as a purple powder.

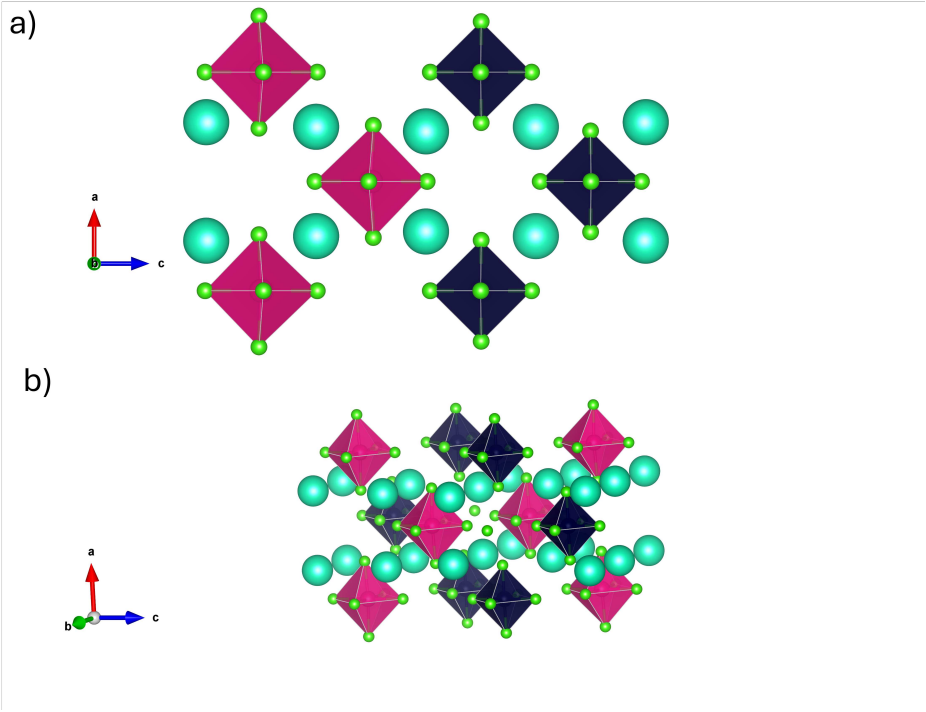

Figure 7.1: Crystal structure of Cs_2SbCl_6 showing one slice of disconnected octahedra (a) and showing highlighting the disconnect between the octahedra (b). Cs is cyan, Sb^{III} is magenta, Sb^{V} is dark blue, and Cl is neon green.

7.2.2 Hydrothermal Crystal growth

Hydrothermal crystallization was carried out following instructions from previous publications.[95] The crystals were grown in Parr Instrument Company model 4749 and 4745 acid digestion vessels (23 and 45 mL capacity respectively) in a Binder APT.line FP convection oven. To ensure the vessels were free of contamination prior to crystallization experiments, the autoclaves were treated with ~8 mL of HNO_3 and heated at 150 °C for 24 h. The vessels were subsequently charged with ~8 mL of unpurified H_2O and heated at 150 °C for 24 h to rinse. This rinse was repeated until contents of the vessel were pH neu-

tral. Each autoclave was charged with previously prepared Cs_2SbCl_6 powder, 5 mL of HCl, and 0.04 grams of excess Cs ions in the form of Cs_2CO_3. The excess Cs ions were added to shift the chemical equilibrium towards Cs_2SbCl_6 rather than $CsSbCl_6$. The reactions were heated to 150 °C over 1 h and then dwelled at the temperature for 24 h to a week before being either slowly cooled over 7 days or quenched in air (see Table 7.1).

7.2.3 Crystallographic Characterization

Sample product identification was verified with laboratory powder X-ray diffraction (PXRD) data collected on a Bruker D8 Discover diffractometer using Cu Kα radiation and a Lynxeye XE-T position sensitive detector. All samples were ground in an agate mortar and pestle before being affixed to a "Zero Diffraction" silicon wafer with a small amount of petroleum jelly. Quantitative phase analysis of X-ray diffraction data was performed using the Rietveld method with TOPAS v6 software package.

7.2.4 UV-Vis diffuse reflectance spectra

UV-vis diffuse reflectance spectra were recorded on a Ocean OpticsFlame 500 spectrometer within range 350 - 1200 nm using the $BaSO_4$ as a standard. Using integrating sphere, The diffuse reflectance data were collected and analyzed to generate the tauc plot in Figure 7.3.

7.2.5 Time-resolved Microwave Conductivity

Time-resolved microwave conductivity (TRMC) measurements were adjusted from procedures described in literature.[96,97] Powder samples were packed into 3 mm EPR tubes. The photoconductivity of the tubes themselves was determined and substracted from the actual samples. TRMC transients were gathered for each sample with varying laser pulse intensities. For all experiments a Nd: YAG laser system equipped with a 355 nm pumped optical parametric oscillator (OPO) was employed for sample excitation (Spectra-Physics PremiScan ULD/500 OPO, pumped by a Spectra-Physics Quanta-Ray, or Continuum Pan-

ther OPO pumped by a Continuum Powerlite). TRMC transients with fits for all samples are depicted in Figure 7.4.

7.3 Results and Discussion

Table 7.1: List of chemical concentrations of Cs_2SbCl_6 and Cs_2CO_3, volume of HCl, dwell duration at 150 °C, and the crystal growth observations.

Cs_2SbCl_6 (mol/mL)	Excess Cs (mol)	HCl (mL)	Temperature Profile	Observation
6.75e-8	5.19e-5	3	17 h dwell, quench	black/white crystals
6.75e-8	5.49e-5	3	17 h dwell, quench	black/white crystals
6.69e-8	5.86e-5	3	1 h dwell, 24 h cool	no crystallization
6.88e-8	5.52e-5	3	1 h dwell, 24 h cool	no crystallization
2.24e-8	5.83e-5	9	24 h dwell, quench	black/white crystals
2.72e-8	4.42e-5	5	24 h dwell, quench	small black crystals
2.67e-8	3.81e-5	5	24 h dwell, quench	1mm black crystals
2.81e-8	1.13e-4	5	7 d dwell, quench	1mm black crystals
2.69e-8	4.94e-5	5	7 d dwell, quench	small black crystals
3.28e-8	1.08e-4	5	7 d dwell, quench	black/white crystals
2.77e-8	7.39e-5	5	7 d dwell, quench	black/white crystals

Phase pure polycrystalline synthesis of Cs_2SbCl_6 was confirmed via PXRD (Figure 7.2). Cs_2SbCl_6 is isostructural to Cs_2SbBr_6. In the structure Cs_2SbBr_6, the charge disproportionation distorts the octahedra forms in the $I4_1/amd$ space group as previously reported by authors.[95,98] Akin to Cs_2SbBr_6, Cs_2SbCl_6 is vacancy ordered that features two different B-site octahedra $[SbCl_6]^{3-}$ and $[SbCl_6]^{-}$ (Figure 7.1). Literature reports have elaborated on the crystal structure through neutron and X-ray diffraction techniques, but conductivity measurements were very low which made it inconclusive on whether the carriers are ionic or electronic.[99,100] Therefore, electronic property measurements from single crystal will benefit our fundamental understanding of VODP such as Cs_2SbCl_6.

We conducted a sequence of hydrothermal syntheses to form single crystals of Cs_2SbCl_6 at the same temperature of 150 °C. We identified the black crystals as Cs_2SbCl_6 via powder X-ray diffraction by grinding up a single crystal. Table 7.1 shows the parameters that led to around 1 mm diameter single crystals. The temperature was set to a constant 150 °C while

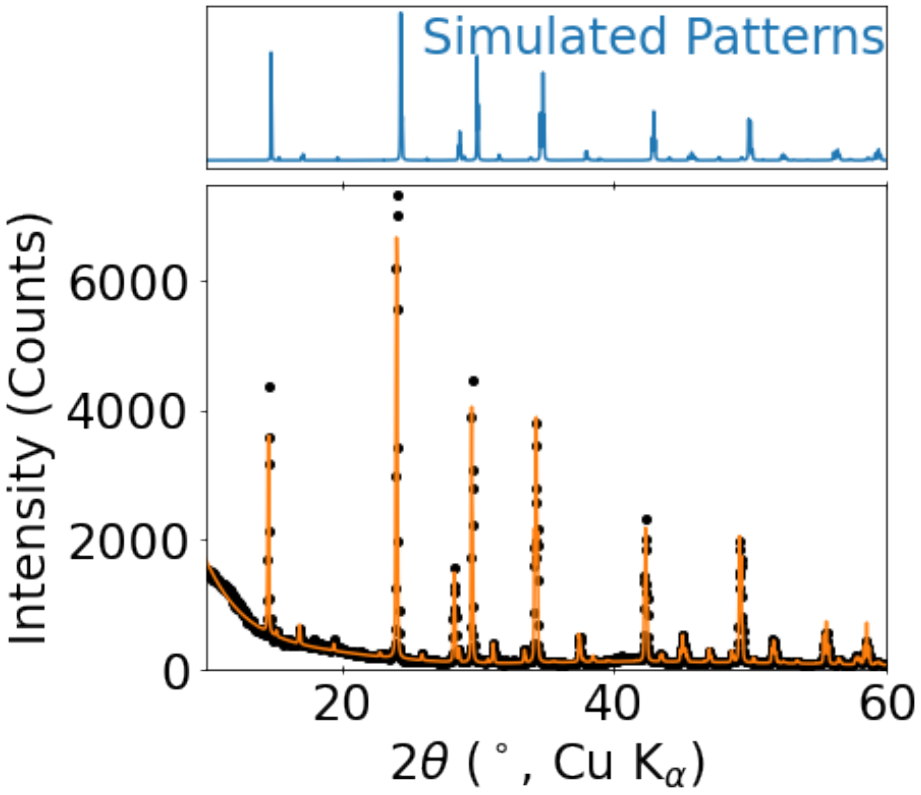

Figure 7.2: PXRD of polycrystalline CS_2SbCl_6 via solution precipitation.

the solute mass and solvent volume was adjusted. To increase the chances to successfully grow single crystal of Cs_2SbCl_6 over competing phases such as $CsSbCl_6$ and $Cs_3Sb_2Cl_9$, excess Cs ions were added in the form of Cs_2CO_3 to the autoclaves.

As seen in Table 7.1, large amounts of excess cesium ions coincides with larger Cs_2SbCl_6 crystals and no $CsSbCl_6$ formation (white crystals). We hypothesize that the excess concentration of Cs shifts the equilibrium towards more Cs_2SbCl_6 and no $CsSbCl_6$. Sb in $CsSbCl_6$ has a valence state of +5, however, upon Cs incorporation and partial reduction, some Sb^{5+} ions reduce to Sb^{3+}) for a mixed valency equal to Sb^{4+} when it forms Cs_2SbCl_6. However, the crystal growth over several days sometimes yielded smaller crystals along with white needle-shaped crystals ($CsSbCl_6$).

We collected UV-vis diffuse reflectance spectra to measure the band gap of the Cs_2SbCl_6. The band gap was extrapolated from the tangent line in Figure 7.3. The band gap is measured to be 0.93(6) eV, which is in agreement to its black coloring.

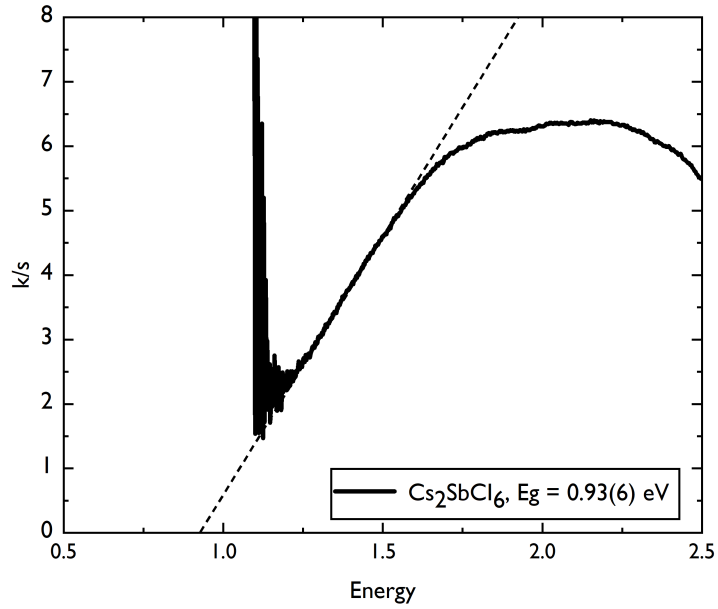

Figure 7.3: UV-vis spectrum of Cs_2SbCl_6. The band gap was extrapolated and determined as 0.93(6) eV.

Time-resolved microwave conductivity (TRMC) was employed to test its conductivity. This technique measures the transient change in microwave reflectivity that carriers generated by a visible laser pulse induce in a sample. The reflectivity of the microwave from the sample is dependent on a material's ability to electrically conduct via free carriers.[101] The free carriers are generated through a pulse laser. The data is shown in Figure 7.4 At all laser pulse frequencies, the data does not measure any microwave conductivity (signal fluctuates around 0 siemens). This suggest that there are no photo-induced charge carriers in Cs_2SbCl_6.

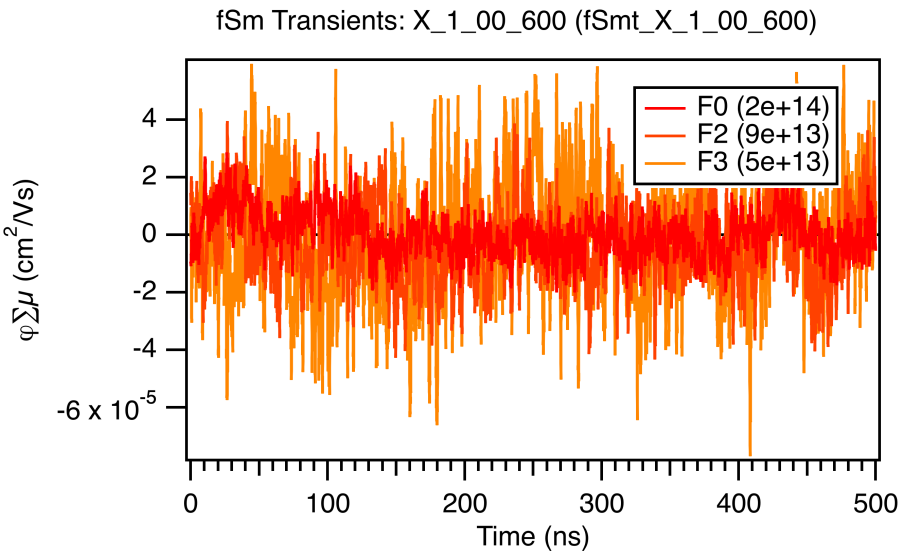

Figure 7.4: TRMC of Cs_2SbCl_6. The sample does not display free carriers and is electronically unconductive despite the small band gap.

Since Cs_2SbCl_6 does not appear to have measurable photoconductivity, further investigations were put on hold. Adjustments to the chemical formula and thus the electronic structure allow for fundamental investigations of VODPs. We learned from previous studies on Cs_2SnX_6 that the optical band gap is dependent on the B-site and X-site ions.[92,102]

As the size of halogens decrease, the band gap widens owing to the non-bonding p states of the halogens that contribute to the highest occupied states in the valence band. The band gap is also based on the interactions between B-site and X-site ions. The conduction band minimum is derived from hybridized states of the B-site cation's 5s and the halogen's p states.[103] On the condition that this behavior holds true in Sb-based VODPs, this offers opportunities to compare and contrast the optical properties of Cs_2SbCl_6 with isostructural counterparts with different halogens and a plethora of solid solutions that feature B-site substitutions, X-site substitutions, a combination of those or vacancies of them to tune the optical properties.

7.3.1 Conclusion

This chapter reports the synthesis of polycrystalline powder and the single crystal growth of Cs_2SbCl_6. We determine that the presence of excess Cs shifts the equilibrium towards Cs_2SbCl_6 over $CsSbCl_6$. More experiments are needed to probe the solubility of Cs_2SbCl_6. Furthermore, the electronic structure remains undetermined by experimental measurements, thus we remain reliant on carefully conducted DFT calculations. However, the outlined synthesis should provide means to easily synthesize single crystals with sufficient size to conduct the necessary measurements. Lastly, Cs_2SbCl_6 does not seem to have useful electronic conductivity despite a relatively small band gap. It would be interesting to compare the system to solid solutions and other isostructural systems.

Chapter 8

Outlook and Future Directions

8.1 Extending *In situ* PXRD Studies of Metathesis Reactions

The bulk of this dissertation revolved around metathesis reaction with the reaction equation template,

$$AMO_2 + LnOX \longrightarrow \mathrm{Li}X + \mathrm{LaMO_3} \tag{8.1}$$

where A=Li, Na, K, M= Mn, Fe, Ln= La, Y and X= Cl ,Br, F. Across multiple chemical phase spaces, the products and key intermediates were identified and modifications to the formula proved useful for product selectivity and further improvements towards milder reaction conditions. For the synthesis of $LaMnO_3$, the cometathesis using multiple spectator anions lowered the reaction temperature conditions below the solidus line of the corresponding halide salts. Considering cation cometathesis reported by Wustrow et al. together with anion cometathesis , the modifications to the metathesis reaction may offer access to many more metastable and functional materials through lowering the reaction onset temperature significantly and offer selectivity as well.[11]

8.2 Extended *In situ* characterization of Metathesis Reaction Kinetics via PXRD and Beyond

X-ray diffraction techniques are the cornerstone of every crystalline materials characterization (at least in this dissertation). Specifically, SXRD was fundamental to the investigations of the metathesis reactions and their kinetics. However, PXRD is agnostic to

noncrystalline phases, and microscopy could compliment the existing studies. *In situ* tomography experiments allows to observe and measure the time scale of the nucleation process in metathesis reactions. Additionally, we would be able to observe the particle growth and consider the effect of the particle geometry on the reaction kinetics. Electron microscopy requires custom parts to visualize hydroscopic materials without damaging the microscope (nor contained within a protective ampule). In addition, in situ conditions can be quite chemically harsh because of halide salts, so experiments where a disposable capillary can be used as a sample holder are ideal, in contrast to specialized heater for TEM studies.

8.3 Extended Kinetic Studies of solid-state Metathesis Reaction

In the chapter on the reaction kinetics of the reactions $MgMn_2O_4 + 2\,YOCl$, $CaMn_2O_4 + 2\,YOCl$, and $LiMnO_2 + YOCl$ were studied using isothermal X-ray diffraction. The kinetic regimes were estimated based on the assumptions outlined by Schmalzried.[3]However, these models may be oversimplified. To evaluate and accurately characterize the kinetics of metathesis reactions more rigorous models are imperative. Furthermore, it would be exciting to investigate the kinetics of metatheses that target non-oxides, in particular nitrides and oxynitrides as their exploration is much harder. In my opinion, kinetics studies in the solid-state are challenging but would pioneer a deeper understanding of solid-state reaction mechanism. As stated in the conclusion of the 'Kinetics chapter', I believe that future studies on kinetics with respect to solid-state synthesis, perhaps specifically for metathesis reactions, would fill an entire dissertation by itself.

Bibliography

[1] Bale, C. W.; Chartrand, P.; Degterov, S.; Eriksson, G.; Hack, K.; Mahfoud, R. B.; Melançon, J.; Pelton, A.; Petersen, S. *calphad* **2002**, *26*, 189–228.

[2] Töpfer, J.; Goodenough, J. *Chemistry of materials* **1997**, *9*, 1467–1474.

[3] Schmalzried, H. **1981**,

[4] Gopalakrishnan, J. *Chemistry of Materials* **1995**, *7*, 1265–1275.

[5] Martinolich, A. J.; Kurzman, J. A.; Neilson, J. R. *Journal of the American Chemical Society* **2016**, *138*, 11031–11037.

[6] Bianchini, M.; Wang, J.; Clément, R. J.; Ouyang, B.; Xiao, P.; Kitchaev, D.; Shi, T.; Zhang, Y.; Wang, Y.; Kim, H.; others *Nature materials* **2020**, *19*, 1088–1095.

[7] Lavina, B.; Downs, R. T.; Sinogeikin, S. *Crystals* **2018**, *8*, 289.

[8] Ranade, M.; Navrotsky, A.; Zhang, H.; Banfield, J.; Elder, S.; Zaban, A.; Borse, P.; Kulkarni, S.; Doran, G.; Whitfield, H. *Proceedings of the National Academy of Sciences* **2002**, *99*, 6476–6481.

[9] Martinolich, A. J.; Neilson, J. R. *Chemistry of Materials* **2017**, *29*, 479–489.

[10] Yang, G.; Park, S.-J. *Materials* **2019**, *12*, 1177.

[11] Wustrow, A.; Huang, G.; McDermott, M. J.; O'Nolan, D.; Liu, C.-H.; Tran, G. T.; McBride, B. C.; Dwaraknath, S. S.; Chapman, K. W.; Billinge, S. J.; others *Chemistry of Materials* **2021**, *33*, 3692–3701.

[12] Meyer, H.-J. *Dalton Transactions* **2010**, *39*, 5973–5982.

[13] Wiley, J. B.; Kaner, R. B. *Science* **1992**, *255*, 1093–1097.

[14] Martinolich, A. J.; Kurzman, J. A.; Neilson, J. R. *Journal of the American Chemical Society* **2015**, *137*, 3827–3833.

[15] Todd, P. K.; Neilson, J. R. *Journal of the American Chemical Society* **2019**, *141*, 1191–1195.

[16] Todd, P. K.; McDermott, M. J.; Rom, C. L.; Corrao, A. A.; Denney, J. J.; Dwaraknath, S. S.; Khalifah, P. G.; Persson, K. A.; Neilson, J. R. *Journal of the American Chemical Society* **2021**, *143*, 15185–15194.

[17] Todd, P. K.; Wustrow, A.; McAuliffe, R. D.; McDermott, M. J.; Tran, G. T.; McBride, B. C.; Boeding, E. D.; O'Nolan, D.; Liu, C.-H.; Dwaraknath, S. S.; others *Inorganic chemistry* **2020**, *59*, 13639–13650.

[18] Wustrow, A.; McDermott, M. J.; O'Nolan, D.; Liu, C.-H.; Tran, G. T.; McBride, B. C.; Vornholt, S. M.; Feng, C.; Dwaraknath, S. S.; Chapman, K. W.; others *Chemistry of Materials* **2022**, *34*, 4694–4702.

[19] O'Nolan, D.; Huang, G.; Kamm, G. E.; Grenier, A.; Liu, C.-H.; Todd, P. K.; Wustrow, A.; Thinh Tran, G.; Montiel, D.; Neilson, J. R.; others *Journal of applied crystallography* **2020**, *53*, 662–670.

[20] Pathak, P.; Vasavada, N. *Acta Crystallographica Section A: Crystal Physics, Diffraction, Theoretical and General Crystallography* **1970**, *26*, 655–658.

[21] England, W.; Goodenough, J.; Wiseman, P. *Journal of Solid State Chemistry* **1983**, *49*, 289–299.

[22] Hayward, M.; Green, M.; Rosseinsky, M.; Sloan, J. *Journal of the American Chemical Society* **1999**, *121*, 8843–8854.

[23] Tsujimoto, Y.; Tassel, C.; Hayashi, N.; Watanabe, T.; Kageyama, H.; Yoshimura, K.; Takano, M.; Ceretti, M.; Ritter, C.; Paulus, W. *Nature* **2007**, *450*, 1062–1065.

[24] Hayward, M. *Semiconductor Science and Technology* **2014**, *29*, 064010.

[25] Schmalzried, H. *Chemical kinetics of solids*; John Wiley & Sons, 2008.

[26] Wustrow, A.; Neilson, J. R. In *Comprehensive Inorganic Chemistry III (Third Edition)*, third edition ed.; Reedijk, J., Poeppelmeier, K. R., Eds.; Elsevier: Oxford, 2023; pp 24–39.

[27] Ramirez, A. *Journal of Physics: Condensed Matter* **1997**, *9*, 8171.

[28] Töpfer, J.; Goodenough, J. *Journal of Solid State Chemistry* **1997**, *130*, 117–128.

[29] Tofield, B.; Scott, W. *Journal of Solid State Chemistry* **1974**, *10*, 183–194.

[30] Mandal, T. K.; Gopalakrishnan, J. *Journal of Materials Chemistry* **2004**, *14*, 1273–1280.

[31] Toberer, E. S.; Weaver, J. C.; Ramesha, K.; Seshadri, R. *Chemistry of materials* **2004**, *16*, 2194–2200.

[32] Tarascon, J.; Guyomard, D. *Journal of The Electrochemical Society* **1991**, *138*, 2864.

[33] Wang, M.; Navrotsky, A. *Journal of Solid State Chemistry* **2005**, *178*, 1230–1240.

[34] Ashiotis, G.; Deschildre, A.; Nawaz, Z.; Wright, J. P.; Karkoulis, D.; Picca, F. E.; Kieffer, J. *Journal of applied crystallography* **2015**, *48*, 510–519.

[35] Kothakonda, M.; Kaplan, A. D.; Isaacs, E. B.; Bartel, C. J.; Furness, J. W.; Ning, J.; Wolverton, C.; Perdew, J. P.; Sun, J. *ACS Materials Au* **2022**,

[36] Furness, J. W.; Kaplan, A. D.; Ning, J.; Perdew, J. P.; Sun, J. *The journal of physical chemistry letters* **2020**, *11*, 8208–8215.

[37] Jain, A.; Ong, S. P.; Hautier, G.; Chen, W.; Richards, W. D.; Dacek, S.; Cholia, S.; Gunter, D.; Skinner, D.; Ceder, G.; others *APL materials* **2013**, *1*, 011002.

[38] Kresse, G.; Hafner, J. *Physical review B* **1993**, *47*, 558.

[39] Bartel, C. J.; Millican, S. L.; Deml, A. M.; Rumptz, J. R.; Tumas, W.; Weimer, A. W.; Lany, S.; Stevanović, V.; Musgrave, C. B.; Holder, A. M. *Nature communications* **2018**, *9*, 1–10.

[40] Yokokawa, H. *Journal of phase equilibria* **1999**, *20*, 258.

[41] Gönen, Z. S.; Gopalakrishnan, J.; Sirchio, S. A.; Eichhorn, B.; Smolyaninova, V.; Greene, R. L. *Journal of Solid State Chemistry* **2001**, *159*, 68–71.

[42] Prado, F.; Sánchez, R.; Caneiro, A.; Causa, M.; Tovar, M. *Journal of Solid State Chemistry* **1999**, *146*, 418–427.

[43] Miyoshi, S.; Kaimai, A.; Matsumoto, H.; Yashiro, K.; Nigara, Y.; Kawada, T.; Mizusaki, J. *Solid State Ionics* **2004**, *175*, 383–386.

[44] Neilson, J. R.; McDermott, M. J.; Persson, K. A. *arXiv preprint arXiv:2303.11915* **2023**,

[45] Islam, M.; Cherry, M.; Catlow, C. *Journal of Solid State Chemistry* **1996**, *124*, 230–237.

[46] David, W.; Thackeray, M.; De Picciotto, L.; Goodenough, J. *Journal of Solid State Chemistry* **1987**, *67*, 316–323.

[47] Armstrong, A. R.; Bruce, P. G. *Nature* **1996**, *381*, 499–500.

[48] Song, K.; Kauzlarich, S. M. *Chemistry of materials* **1994**, *6*, 386–394.

[49] Odink, D. A.; Kauzlarich, S. M. *Molecular Crystals and Liquid Crystals* **1990**, *181*, 325–332.

[50] Spaldin, N. A.; Ramesh, R. *Nature materials* **2019**, *18*, 203–212.

[51] Valant, M.; Axelsson, A.-K.; Alford, N. *Chemistry of Materials* **2007**, *19*, 5431–5436.

[52] Morozov, M.; Lomanova, N.; Gusarov, V. *Russian journal of general chemistry* **2003**, *73*, 1676–1680.

[53] Bernardo, M.; Jardiel, T.; Peiteado, M.; Mompean, F.; Garcia-Hernandez, M.; Garcia, M.; Villegas, M.; Caballero, A. *Chemistry of Materials* **2013**, *25*, 1533–1541.

[54] Wang, Y.; Zhou, L.; Zhang, M.; Chen, X.; Liu, J.-M.; Liu, Z. *Applied Physics Letters* **2004**, *84*, 1731–1733.

[55] Selbach, S. M.; Einarsrud, M.-A.; Grande, T. *Chemistry of Materials* **2009**, *21*, 169–173.

[56] Gillan, E. G.; Kaner, R. B. *Chemistry of materials* **1996**, *8*, 333–343.

[57] Tran, G. T.; Wustrow, A.; O'Nolan, D.; Tao, S.; Bartel, C. J.; He, T.; McDermott, M. J.; McBride, B. C.; Chapman, K. W.; Billinge, S. J.; others *Inorganic chemistry* **2023**,

[58] McDermott, M. J.; McBride, B. C.; Regier, C. E.; Tran, G. T.; Chen, Y.; Corrao, A. A.; Gallant, M. C.; Kamm, G. E.; Bartel, C. J.; Chapman, K. W.; others *ACS Central Science* **2023**, *9*, 1957–1975.

[59] McAuliffe, R. D.; Kamm, G. E.; McDermott, M. J.; Hermann, R. P.; Vasquez-Garcia, N.; Sacci, R. L.; Persson, K. A.; Chapman, K. W.; Veith, G. M. *Inorganic Chemistry* **2023**, *62*, 3358–3367.

[60] McDermott, M. J.; Dwaraknath, S. S.; Persson, K. A. *Nature communications* **2021**, *12*, 3097.

[61] Miura, A.; Ito, H.; Bartel, C. J.; Sun, W.; Rosero-Navarro, N. C.; Tadanaga, K.; Nakata, H.; Maeda, K.; Ceder, G. *Materials horizons* **2020**, *7*, 1310–1316.

[62] Richards, W. D.; Miara, L. J.; Wang, Y.; Kim, J. C.; Ceder, G. *Chemistry of Materials* **2016**, *28*, 266–273.

[63] Lu, J.; Qiao, L.; Fu, P.; Wu, Y. *Journal of crystal growth* **2011**, *318*, 936–941.

[64] Meera, A.; Ganesan, R.; Gnanasekaran, T. *Journal of Alloys and Compounds* **2017**, *692*, 841–847.

[65] Aykol, M.; Montoya, J. H.; Hummelshøj, J. *Journal of the American Chemical Society* **2021**, *143*, 9244–9259.

[66] Levin, E. M.; Roth, R. S. *Journal of research of the National Bureau of Standards. Section A, Physics and chemistry* **1964**, *68*, 197.

[67] Wesley, C.; Bellcase, L.; Forrester, J. S.; Dickey, E. C.; Reaney, I. M.; Jones, J. L. *Journal of the American Ceramic Society* **2024**,

[68] Kamm, G. E.; Huang, G.; Vornholt, S. M.; McAuliffe, R. D.; Veith, G. M.; Thornton, K. S.; Chapman, K. W. *Journal of the American Chemical Society* **2022**, *144*, 11975–11979.

[69] Truong, Q. D.; Kobayashi, H.; Nayuki, K.; Sasaki, Y.; Honma, I. *Solid State Ionics* **2020**, *344*, 115136.

[70] Todd, P. K.; Smith, A. M.; Neilson, J. R. *Inorganic Chemistry* **2019**, *58*, 15166–15174.

[71] Lai, K. T.; Antonyshyn, I.; Prots, Y.; Valldor, M. *Journal of the American Chemical Society* **2017**, *139*, 9645–9649.

[72] Bhat, M. A.; Zargar, R. A.; Modi, A.; Arora, M.; Gaur, N. *Progress in Natural Science: Materials International* **2016**, *26*, 579–583.

[73] Wu, M.-K.; Ashburn, J. R.; Torng, C.; Hor, P.-H.; Meng, R. L.; Gao, L.; Huang, Z. J.; Wang, Y.; Chu, a. *Physical review letters* **1987**, *58*, 908.

[74] Figen, H.; Guldal, N.; Baykara, S. *Acta Physica Polonica A* **2014**, *125*, 278–280.

[75] Aleandri, L.; McCarley, R. *Inorg. Chem.;(United States)* **1988**, *27*.

[76] Mikhailova, D.; Bramnik, N.; Bramnik, K.; Reichel, P.; Oswald, S.; Senyshyn, A.; Trots, D.; Ehrenberg, H. *Chemistry of Materials* **2011**, *23*, 3429–3441.

[77] Zimmerman, H. E. *Accounts of chemical research* **2012**, *45*, 164–170.

[78] De Castro, I. A.; Datta, R. S.; Ou, J. Z.; Castellanos-Gomez, A.; Sriram, S.; Daeneke, T.; Kalantar-zadeh, K. *Advanced Materials* **2017**, *29*, 1701619.

[79] Zakutayev, A. *Journal of Materials Chemistry A* **2016**, *4*, 6742–6754.

[80] Hultman, L. *Vacuum* **2000**, *57*, 1–30.

[81] Guo, Y.; Li, H.; Clark, S.; Robertson, J. *The Journal of Physical Chemistry C* **2019**, *123*, 5562–5570.

[82] DiSalvo, F. J.; Clarke, S. J. *Current Opinion in Solid State and Materials Science* **1996**, *1*, 241–249.

[83] Etourneau, J.; Portier, J.; Ménil, F. *Journal of alloys and compounds* **1992**, *188*, 1–7.

[84] Lewis, G. N. *Valence and the Structure of Atoms and Molecules*; Chemical Catalog Company, Incorporated, 1923.

[85] Sun, W.; Bartel, C. J.; Arca, E.; Bauers, S. R.; Matthews, B.; Orvañanos, B.; Chen, B.-R.; Toney, M. F.; Schelhas, L. T.; Tumas, W.; others *Nature materials* **2019**, *18*, 732–739.

[86] Arca, E.; Lany, S.; Perkins, J. D.; Bartel, C.; Mangum, J.; Sun, W.; Holder, A.; Ceder, G.; Gorman, B.; Teeter, G.; others *Journal of the American Chemical Society* **2018**, *140*, 4293–4301.

[87] Kageyama, H.; Hayashi, K.; Maeda, K.; Attfield, J. P.; Hiroi, Z.; Rondinelli, J. M.; Poeppelmeier, K. R. *Nature communications* **2018**, *9*, 772.

[88] Lopez-Aranguren, P.; Reynaud, M.; Głuchowski, P.; Bustinza, A.; Galceran, M.; Lopez del Amo, J. M.; Armand, M.; Casas-Cabanas, M. *ACS Energy Letters* **2021**, *6*, 445–450.

[89] Fuertes, A. *Progress in Solid State Chemistry* **2018**, *51*, 63–70.

[90] Otsuka, Y.; Pithan, C.; Dornseiffer, J.; Takada, T.; Konoike, T.; Waser, R. *Journal of the European Ceramic Society* **2016**, *36*, 2719–2725.

[91] Li, C.; Yang, Y.; Lv, L.; Huang, H.; Wang, Z.; Yang, S. *Journal of alloys and compounds* **2008**, *457*, 57–60.

[92] Maughan, A. E.; Ganose, A. M.; Scanlon, D. O.; Neilson, J. R. *Chemistry of Materials* **2019**, *31*, 1184–1195.

[93] Lee, B.; Stoumpos, C. C.; Zhou, N.; Hao, F.; Malliakas, C.; Yeh, C.-Y.; Marks, T. J.; Kanatzidis, M. G.; Chang, R. P. *Journal of the American Chemical Society* **2014**, *136*, 15379–15385.

[94] Qiu, X.; Cao, B.; Yuan, S.; Chen, X.; Qiu, Z.; Jiang, Y.; Ye, Q.; Wang, H.; Zeng, H.; Liu, J.; others *Solar Energy Materials and Solar Cells* **2017**, *159*, 227–234.

[95] Combs, V. E.; Oswald, I. W.; Neilson, J. R. *Crystal Growth & Design* **2019**, *19*, 4090–4094.

[96] Reid, O. G.; Moore, D. T.; Li, Z.; Zhao, D.; Yan, Y.; Zhu, K.; Rumbles, G. *Journal of Physics D: Applied Physics* **2017**, *50*, 493002.

[97] Savenije, T. J.; Ferguson, A. J.; Kopidakis, N.; Rumbles, G. *The Journal of Physical Chemistry C* **2013**, *117*, 24085–24103.

[98] Prassides, K.; Day, P.; Cheetham, A. K. *Inorganic chemistry* **1985**, *24*, 545–552.

[99] Clark, H.; Swanson, B. I. *Journal of the American Chemical Society* **1981**, *103*, 2928–2933.

[100] Ionov, S.; Ionova, G.; Makarov, E.; Yu. Aleksandrov, A. *physica status solidi (b)* **1974**, *64*, 79–85.

[101] Brenot, R.; Vanderhaghen, R.; Drevillon, B.; French, I.; i Cabarrocas, P. R. *Thin Solid Films* **1997**, *296*, 94–97.

[102] Cai, Y.; Xie, W.; Ding, H.; Chen, Y.; Thirumal, K.; Wong, L. H.; Mathews, N.; Mhaisalkar, S. G.; Sherburne, M.; Asta, M. *Chemistry of Materials* **2017**, *29*, 7740–7749.

[103] Pradhan, A.; Jena, M. K.; Samal, S. L. *ACS Applied Energy Materials* **2022**, *5*, 6952–6961.

Appendix A

Supplemental Information: Selective Synthesis of Defect-Rich $LaMnO_3$ by Low Temperature Anion Cometathesis

A.1 Reported $LaMnO_3$ Syntheses

Table A.1: List of DOIs with reported $LaMnO_3$ syntheses with extracted reaction temperature. The synthesis temperature were reported in Figure 2.1

DOI	Temperature Temperature (°C)
10.1039/c3ta00982c	1599.85 °C
10.1021/jp408585z	1000 °C
10.1111/j.1744-7402.2006.02065.x	1200 °C
10.1007/s10854-017-7276-9	1350 °C
10.1007/s10853-015-9109-7	1199.85 °C
10.1039/b914975a	1400 °C
10.1016/j.ssi.2004.08.008	1399.85 °C
10.1016/s0167-2738(01)00737-8	1100 °C
10.1016/j.ssi.2004.07.024	1400 °C
10.1039/c5fd00187k	700 °C
10.1039/c5cp00842e	1350 °C
10.1016/j.elspec.2012.06.017	1019.85 °C
10.1016/j.ssi.2010.02.024	1500 °C
10.1016/j.ssi.2011.02.007	1400 °C
10.1016/j.apsusc.2014.03.134	1099.85 °C

10.1016/j.apcata.2004.12.009	699.85 °C
10.1016/j.apcata.2006.03.019	600 °C
10.1016/j.ssc.2004.12.010	1000 °C
10.1016/j.jpowsour.2013.11.093	1300 °C
10.1016/s0304-8853(00)01404-9	1400 °C
10.1016/j.jmmm.2007.03.171	999.85 °C
10.1016/j.surfcoat.2005.08.131	1000 °C
10.1016/j.physc.2004.11.020	900 °C
10.1016/j.physc.2005.10.013	900 °C
10.1016/j.physc.2010.02.002	1300 °C
10.1016/s0167-577x(01)00565-1	1200 °C
10.1016/j.matlet.2009.08.032	1500 °C
10.1016/j.ceramint.2015.02.001	1350 °C
10.1103/physrevb.92.125118	1400 °C
10.1103/physrevb.70.094403	1350 °C
10.1103/physrevb.80.045123	1250 °C
10.1103/physrevb.82.235102	1400 °C
10.1103/physrevb.72.064425	1400 °C
10.1103/physrevb.71.134402	1250 °C
10.1016/s0022-3697(03)00266-x	1370 °C
10.1016/s0022-4596(02)00028-2	1100 °C
10.1016/s0022-4596(03)00050-1	1300 °C
10.1016/j.elspec.2004.02.093	1350 °C
10.1016/s0021-9517(03)00265-3	999.85 °C
10.1016/j.mseb.2004.02.009	800 °C
10.1016/s0167-2738(99)00276-3	999.85 °C
10.1016/s0167-2738(99)00324-0	1099.85 °C

10.1016/j.ssc.2003.08.004	1400 °C
10.1016/j.jmmm.2003.12.751	1500 °C
10.1016/s0304-8853(02)01343-4	1200 °C
10.1016/s0304-8853(03)00040-4	1400 °C
10.1016/s0921-5107(00)00438-4	999.85 °C
10.1016/s0304-8853(99)00620-4	1450 °C
10.1016/s0304-8853(00)00429-7	1100 °C
10.1016/j.jeurceramsoc.2012.10.023	1500 °C
10.1016/s0167-2738(98)00045-9	1000 °C
10.1063/1.3242008	1450 °C
10.1063/1.3671070	1099.85 °C
10.1063/1.4966610	1100 °C
10.1063/1.4811372	1600 °C
10.1063/1.4789315	1600 °C
10.1063/1.5053705	1100 °C
10.1016/j.jmmm.2018.07.047	1200 °C
10.1016/j.molcata.2006.05.008	600 °C
10.1016/j.jeurceramsoc.2019.03.003	1000 °C
10.1063/1.4872216	1350 °C

A.2 Laboratory X-ray Diffraction Data

Bulk reactions were prepared by mixing stoichiometric amounts of $LiMnO_2$ and lanthanum oxyhalides. Reactions were heated at 10 °C/min to the dwell temperature (600 °C) to ensure product formation within four hours (see methods section for further details). Bulk reactions reach oxidized $LaMnO_{3+x}$ as the equilibrium product, as indicated

by the small unit cell volume (60.812(1) Å^3/fu) relative to the stoichiometric unit cell reported in the literature.

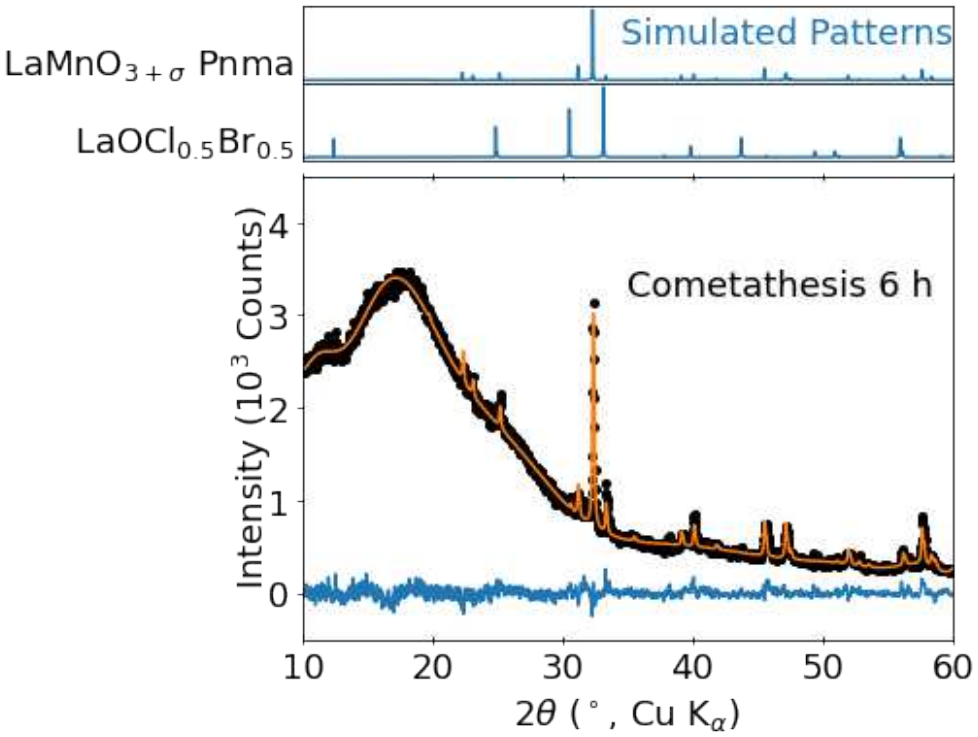

Figure A.1: Laboratory X-ray diffraction data of the product from quenched ex situ, bulk reactions of anion cometathesis 0.5 LaOCl + 0.5 LaOBr + $LiMnO_2$ after 4 h at 650 °C. Anion cometathesis forms orthorhombic defect rich $LaMnO_3$ in the *Pnma* spacegroup. After dwelling at the reaction temperature for 4 h, there is residual LaOX yet no more $LiMnO_2$ is visible by diffraction.

A.3 Thermodynamics

Subtle differences of entropy contributions to the reaction thermodynamics manifest in the reaction temperature and reactivity for the formation of $LaMnO_3$. Reaction energies, ΔG_{rxn}, were calculated with the meta-GGA density functional theory, r2SCAN (Fig. A.2). The model incorporates reaction enthalpy and entropy of the reaction. The entropy of reaction is summed up as the entropy of vibration and the entropy of mixing (Fig. A.3). Single anion metathesis with chlorine is calculated to have a stronger driving force while a

metathesis with bromine should have the lowest driving force relative to the driving force from the chlorine and the mixed anion systems. However, the model calculates that a metathesis with both anions will have similar driving forces as $LaOCl + LiMnO_2$ at elevated temperatures. Yet, the observed reaction onset temperatures suggest that the differences in entropy have a non-negligible impact on the reaction.

Thermodynamic calculations were performed to evaluate and compare the reaction energetics of each system. The Gibbs energies were compiled from FactSage.[39] Enthalpies were calculated with meta generalized gradient approximation (r2scan meta-GGA) density functional theory, which were strongly constrained and appropriately normed. To calculate the temperature-dependent energies, the entropic contributions from vibrational entropy of the lattice and the configurational entropy of solid solutions were included (when formed). The model assumes each phase to be solid in all reactions. Thus, the mean absolute error is $\approx$ 50 meV·atoms^{-1} (Figure A.2 and A.3).

A.4 Crystallographic Analysis of Mn_3O_4

Crystallographic examination of the evolution of intermediates that appear in the reaction mixture provides corroborating evidence of the progression from a local to bulk equilibrium at higher reaction temperatures. The ex post facto analysis reveal that tetragonal $LiMnO_2$ undergoes a phase transformation into the more thermodynamically stable orthorhombic $LiMnO_2$ polymorph $Pmnm$, as well as the formation of a phase that is best indexed as tetragonal spinel consistent with the model Mn_3O_4 ($I4_1/amd$). The presence of the orthorhombic phase and the tetragonal spinel is similar to the disproportionation described by our previous work.[17] There, the presence of both in the intermediates suggested a charge disproportionation of manganese ions, with the defected cubic spinel $LiMn_2O_4$ accumulating formally oxidized $Mn^{3+\delta}$ cations and the defected tetragonal spinel Mn_3O_4 accumulating formally reduced $Mn^{3-\delta}$ cations. However, this study finds only a defect-rich spinel and an over-oxidized $LaMnO_{3+x}$.

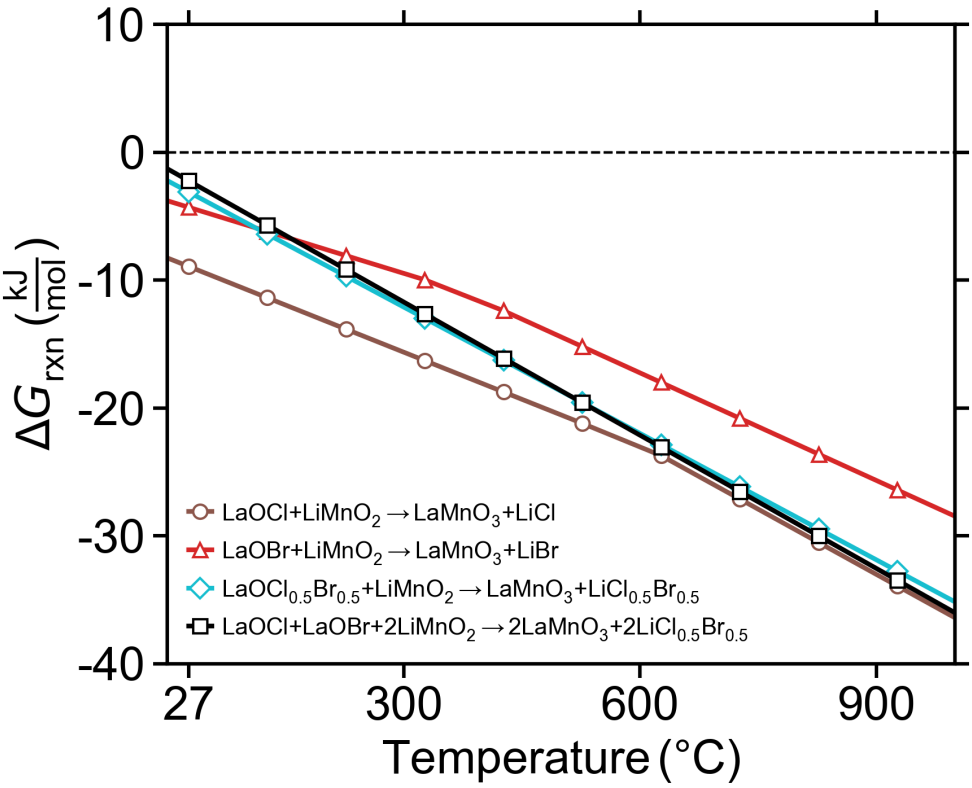

Figure A.2: ΔG_{rxn} calculation from meta-GGA density functional, r2SCAN of $LaOCl + LiMnO_2$ (brown circles), $LaOBr + LiMnO_2$ (red triangles), 0.5$LaOCl$ $^{+}0.5$ $LaOBr + LiMnO_2$ (black squares), and $LaOCl_{0.5}Br_{0.5} + LiMnO_2$ (cyan diamonds). ΔG_{rxn} calculations suggest lowest reaction temperature for the formation of $LaMnO_3$ occurs with $LaOCl + LiMnO_2$, and highest reaction temperature for $LaOBr + LiMnO_2$

The observation of stoichiometric Mn_3O_4 would suggest that there is a net reduction of Mn during the reaction, or it may serve as a source of excess oxygen during the formation of $LaMnO_{3+x}$. From the Rietveld analysis of the Mn_3O_4 phase, the peak intensities are inconsistent with a stoichiometric model. One such way to interpret the diffraction data are by a reduced Mn site occupancy in the octahedral site, as the fit of the model to the data improves as illustrated in Figure 2.6. The octahedral site (with a site multiplicity of 8) results with a reduced occupancy ($g(\mathrm{Mn_{oct}}) = 0.671(1)$), consistent with either vacancies or Li substitution, Yet, the tetrahedral site (site multiplicity of 4) occupancy remains relatively unchanged($g(\mathrm{Mn_{tetra}}) = 0.0.958(1)$). Assuming that a vacancy replaces the Mn, the average Mn valence of the $Mn_{3-x}O_4$ phase is 3.03(1); if one assumes Li_{Mn} substitution,

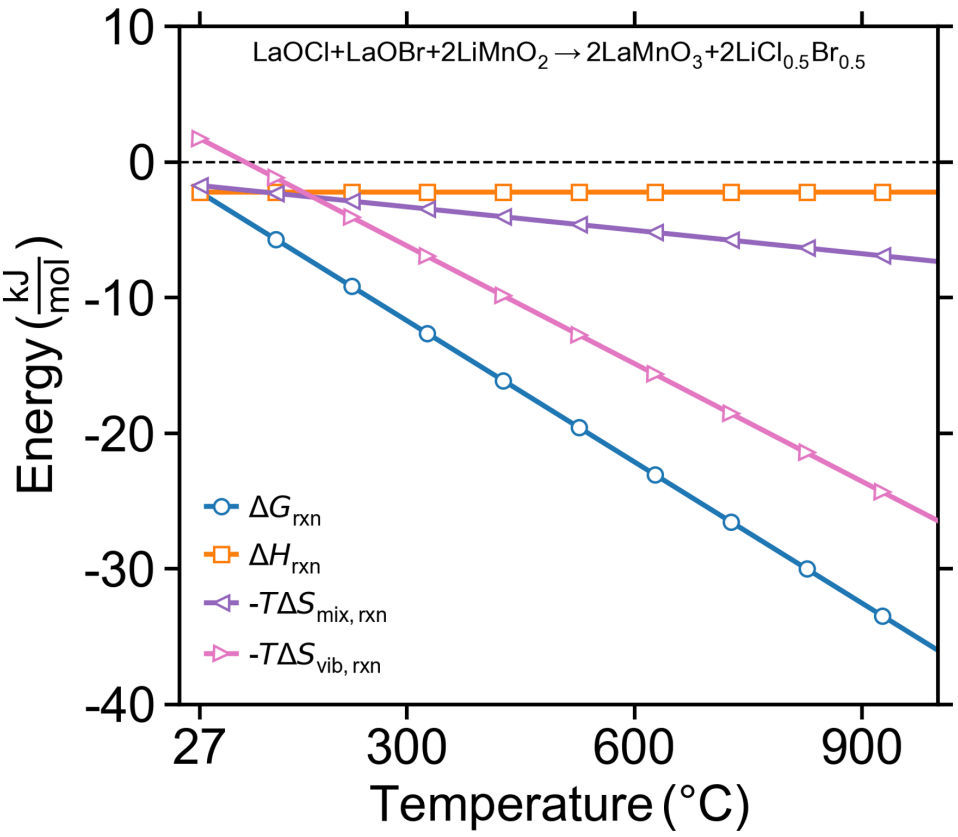

Figure A.3: Energy calculation from meta-GGA density functional, r2SCAN of 0.5 LaOCl + 0.5 LaOBr + $LiMnO_2$ with ΔG_{rxn} in blue circles, ΔH_{rxn} in orange squares, entropy of mixing -$T\Delta S_{mix}$ in purple triangles, and entropy of vibration -$T\Delta S_{vib}$ in pink triangles. $LaOCl_{0.5}Br_{0.5}$ + $LiMnO_2$ has a positive and linearly growing -$T\Delta S_{mix}$ term. 0.5 LaOCl + 0.5 LaOBr + $LiMnO_2$ -$T\Delta S_{mix}$ energetically contributes to spontaneous reaction. The differences in structural strains and imperfections possibly lead to different reaction temperatures.

the valence is 3.08(1). Therefore, the change in the manganese valence averaged over all Mn compounds during the reaction is small or slightly oxidized. This observation is consistent with previous studies of the metathesis reactions $LiMnO_2$ + YOCl, during which $LiMnO_2$ reacted towards two lithium manganese oxide spinel intermediates.[17,46] There, the presence of both in the intermediates suggested a charge disproportionation of manganese ions, with the defected cubic spinel $LiMn_2O_4$ accumulating a $Mn^{3+\delta}$ valence and the tetragonal spinel accumulating a $Mn^{3-\delta}$ Mn valence.[17,47] However, this analysis is not robust, as the resulting bond distances from free refinement of the atomic coordinates yields

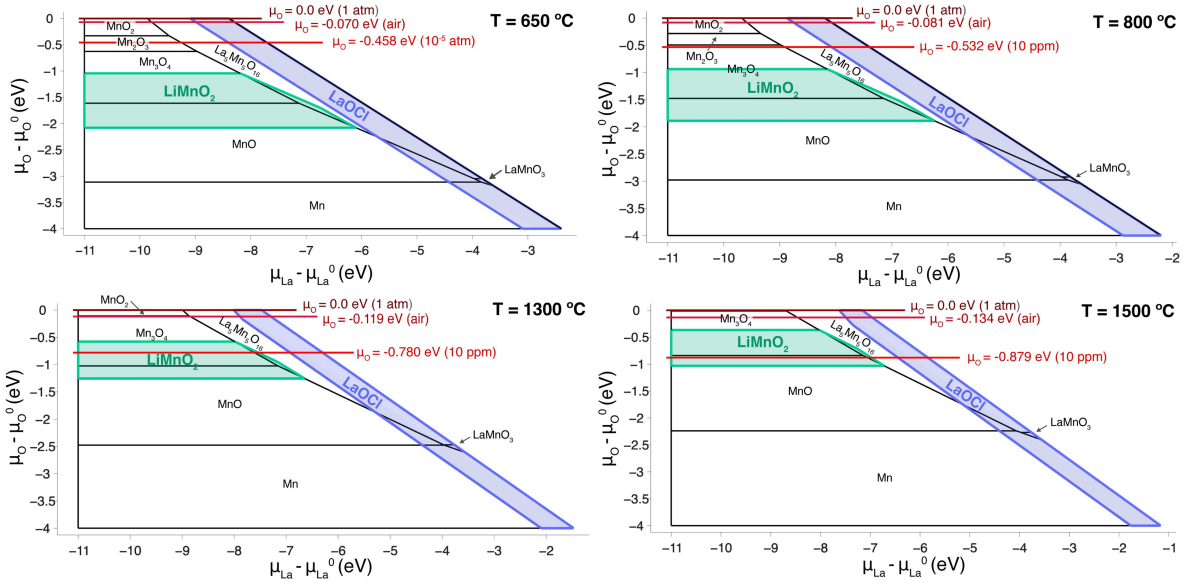

Figure A.4: Predominance diagram of lanthanum and oxygen chemical potential referenced to their standard elemental state shown at 650 °C (upper left), 800 °C (upper right), 1300 °C (lower left),and 1500 °C (lower right). Pressures of oxygen gas (lines in red) highlight the chemical potential that is expected at 1 atm, partial oxygen pressure in air, and partial pressure that is expected in an argon atmosphere (10 ppm). $LiMnO_2$ (green), LaOCl (blue), were plotted as a plane across the chemical potential space. The metathesis byproduct LiX has been omitted for visual clarity as it is always stable. All projected phases overlap with the 'overoxidized' phase $La_5Mn_5O_{16}$ and share a stable interface with the oxidized phase. Only LaOCl overlaps with $LaMnO_3$.

yield unphysical bond valence sums. This is related to the high correlation of multiple refinement parameters due to the strong overlap of multiple reflections in the diffraction pattern. As such, Mn_3O_4, could be present solely to offset the presence of the over-oxidized $LaMnO_{3+x}$, or it is itself defective with only Mn^{3+} present in the mixture.

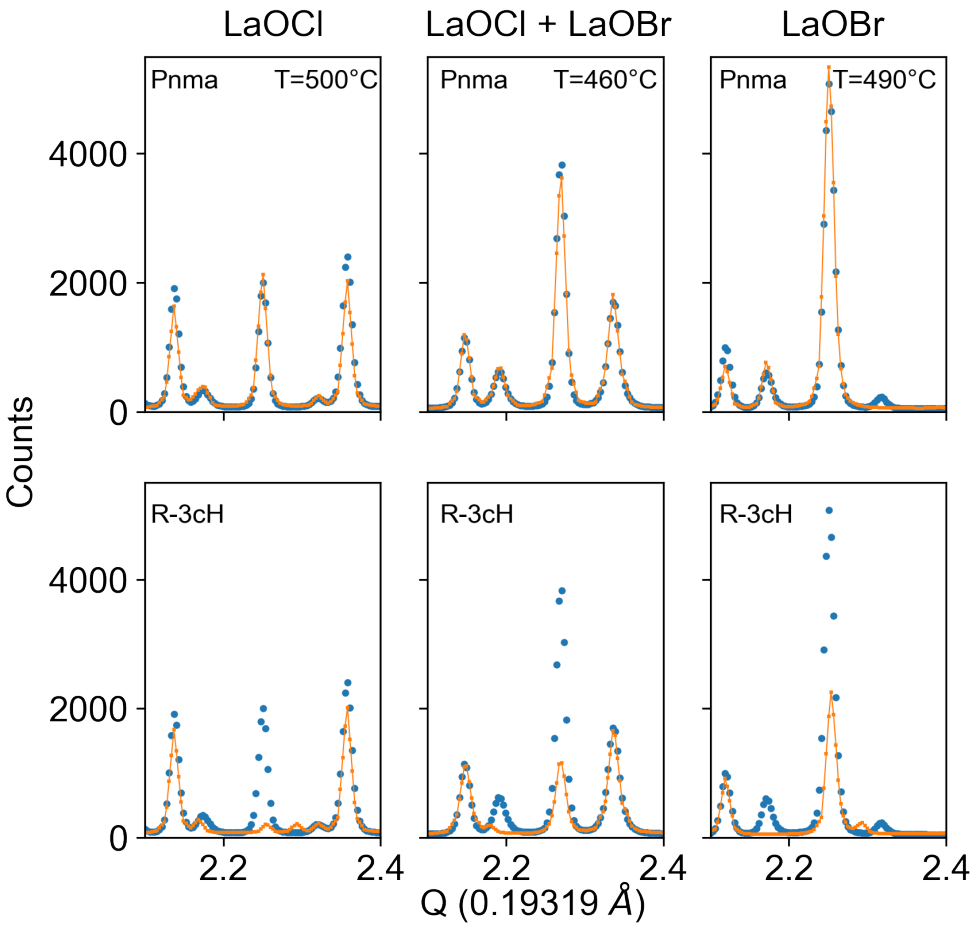

Figure A.5: Comparisons of Rietveld refinements using $LaMnO_3$ with space group *Pnma* vs. *R-3cH*. All models fit (orange triangle) the data (blue dots) better when using space group *Pnma* over *R-3cH*.

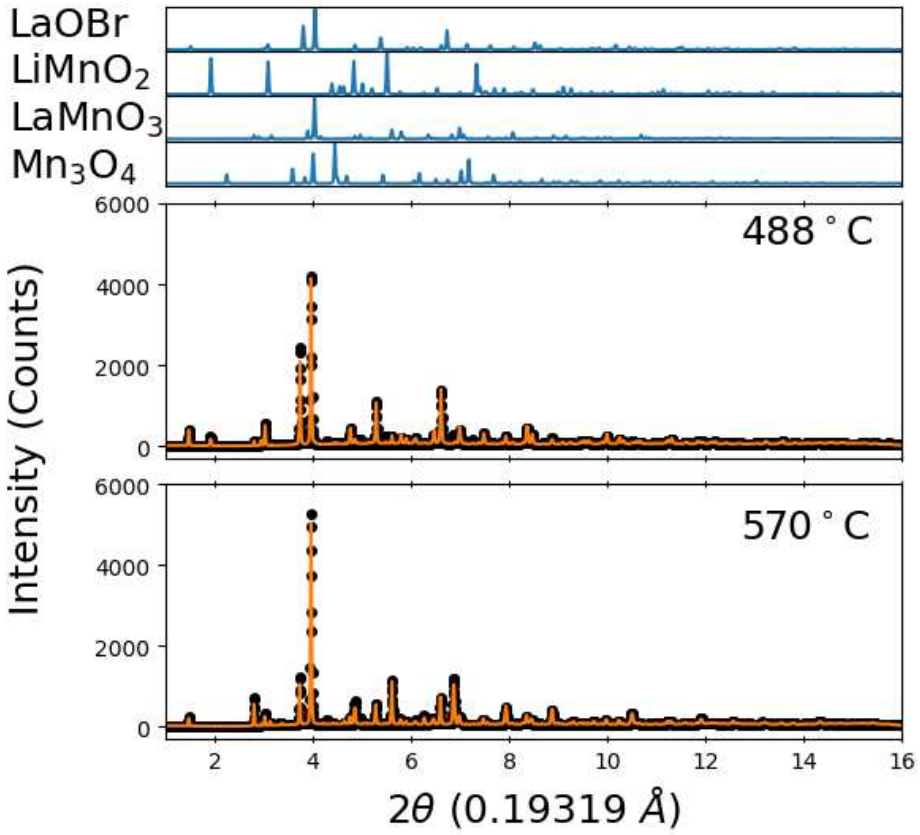

Figure A.6: X-ray diffraction data from *in situ* synchrotron NSLS II of bulk reaction LaOBr+$LiMnO_2$ at 488 °C and 570 °C.

Appendix B

Supplemental Information: Synthesis of $BiFeO_3$ Using Metathesis Reactions

B.1 X-ray Diffraction Data

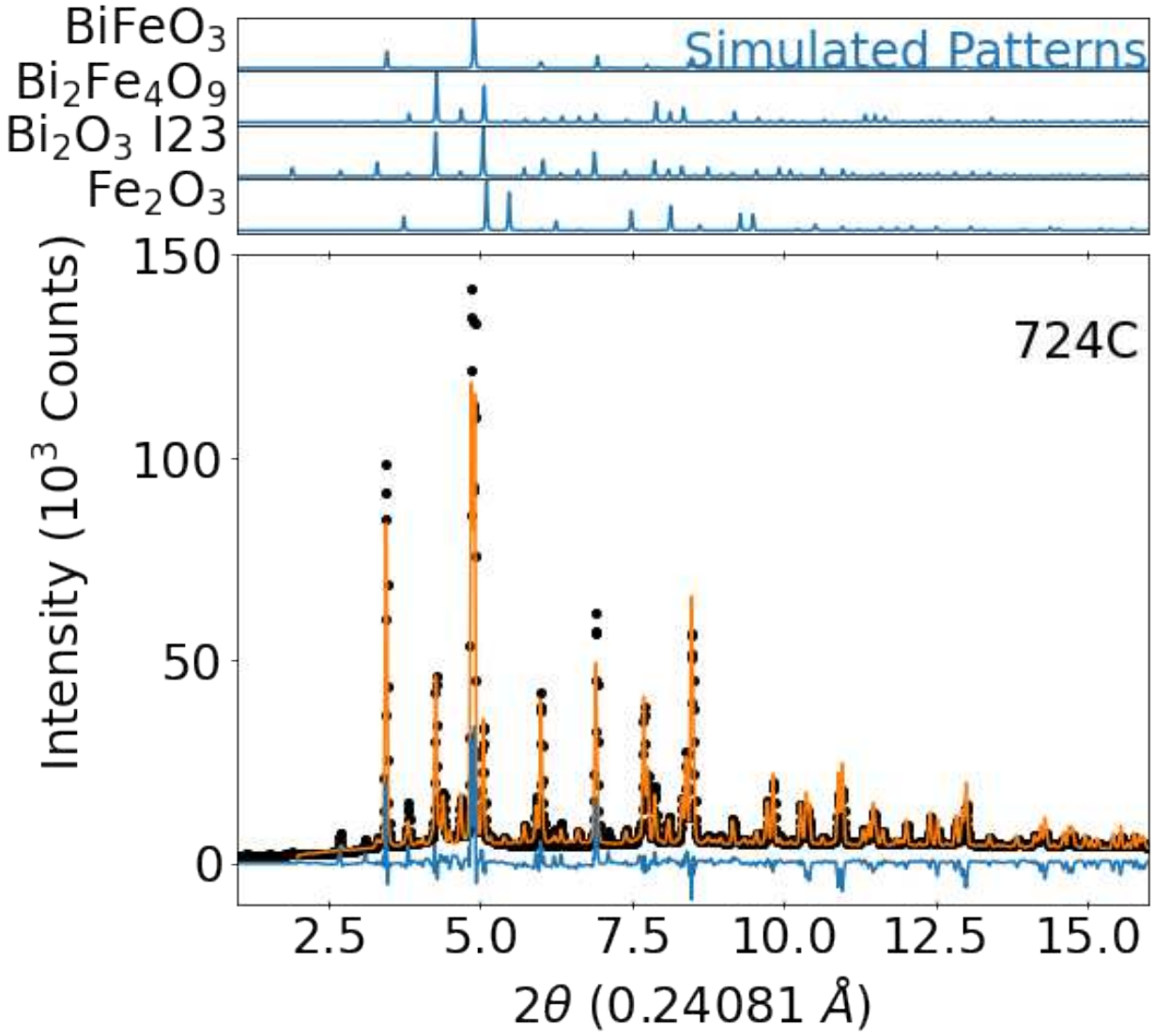

Figure B.1: In situ synchrotron PXRD data collected from the reaction BiOF + $KFeO_2$ using a gradient furnace at short time points at 724 °C. The PXRD captures the crystalline phases $BiFeO_3$, $Bi_{25}FeO_{39}$, Bi_2O_3, Fe_2O_3.

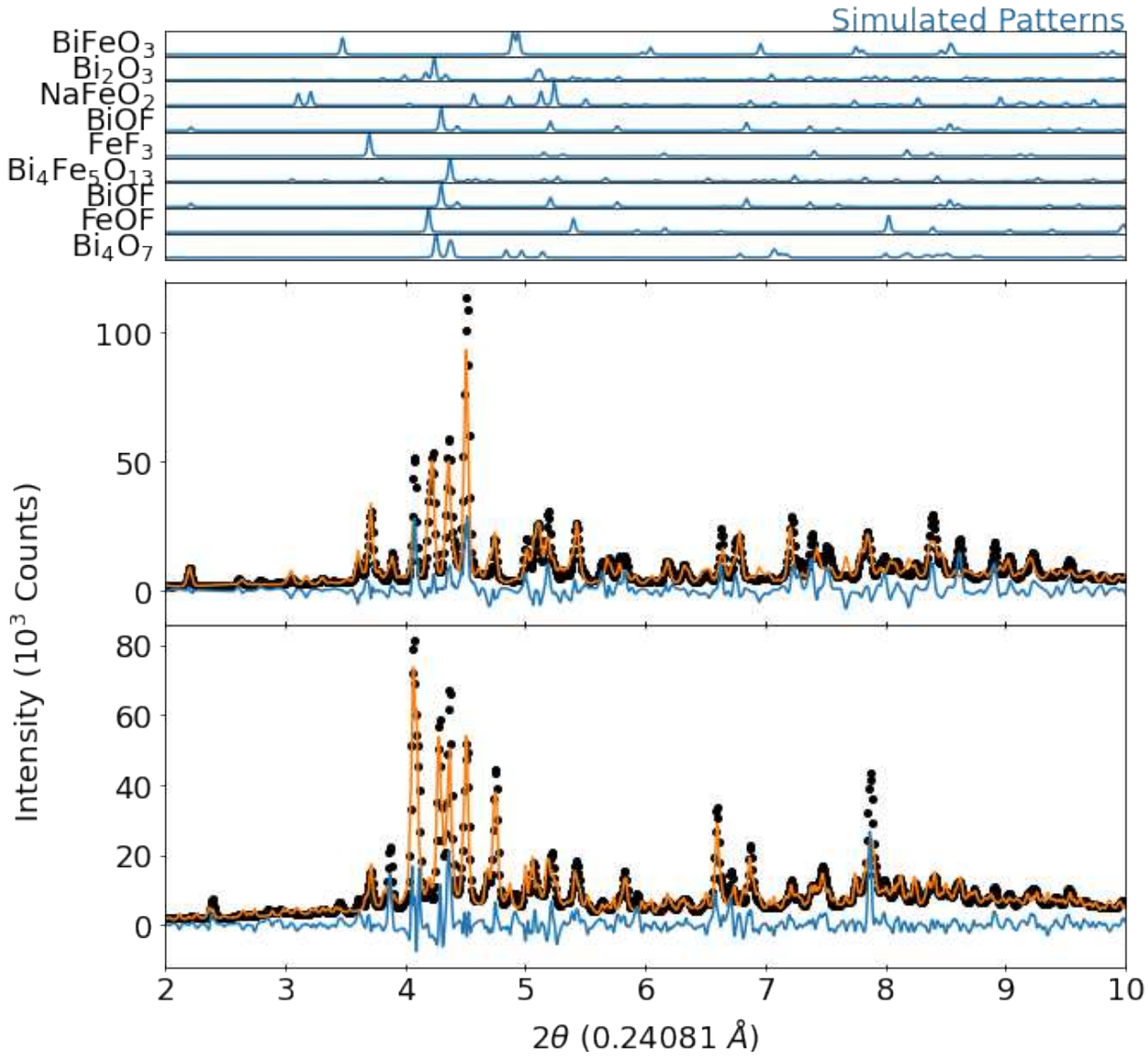

Figure B.2: In situ synchrotron PXRD data collected from the reaction BiOF + $NaFeO_2$ using a gradient furnace at short time points at 724 °C.

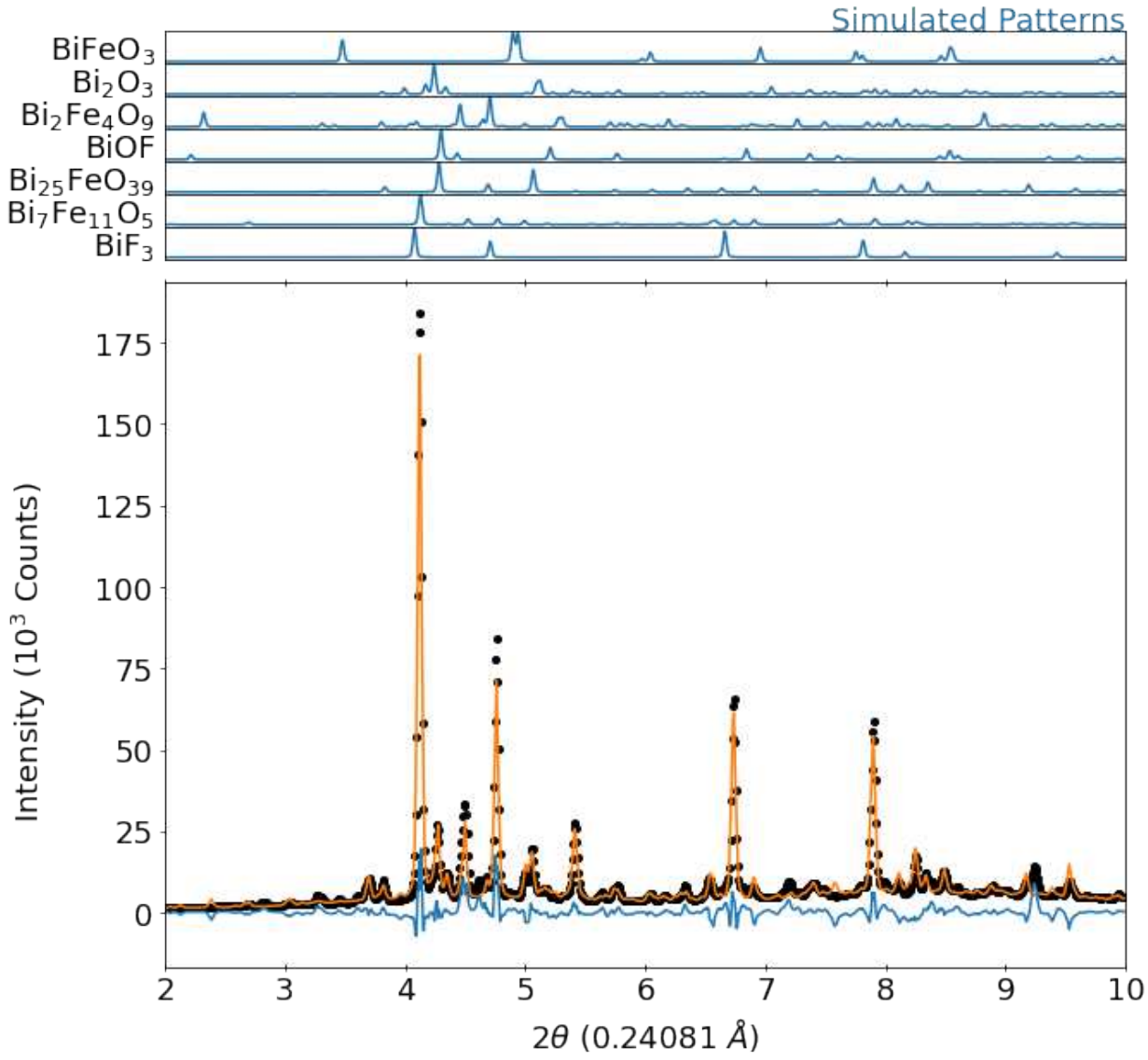

Figure B.3: In situ synchrotron PXRD data collected from the reaction BiOF + $LiFeO_2$ using a gradient furnace at short time points at 724 °C.